universität wien

MASTERARBEIT | MASTER'S THESIS

Titel | Title

Rotational cooling of non-spherical particles

verfasst von | submitted by

Florian Johannes Friedrich Fechtel B.Sc.

angestrebter akademischer Grad | in partial fulfilment of the requirements for the degree of

Master of Science (MSc)

Wien | Vienna, 2024

Studienkennzahl lt. Studienblatt | Degree programme code as it appears on the student record sheet:	UA 066 876
Studienrichtung lt. Studienblatt | Degree programme as it appears on the student record sheet:	Masterstudium Physics
Betreut von | Supervisor:	Univ.-Prof. Dr. Markus Arndt

Acknowledgements

First and foremost, I thank Prof. Markus Arndt for enabling my master's thesis in this state-of-the-art-experiment. I am especially grateful for the opportunity to contribute as an intern before starting with my project. Furthermore, I appreciate your eagerness to advance the experiment and your commitment to collaborate with other researchers, exchanging valuable ideas.

Additionally, I thank my lab partners, Stephan Troyer and Lorenz Hummer, for welcoming me into the cavity group and for introducing me into the experiment. I appreciate that you are always available, and open to discussing and explaining the relevant physics. I would also like to thank Stefan Schrems for changing ideas during lunch.

I thank Dr. Uroš Delić for the fruitful discussions and helpful tips on experimental problems, and of course for his support with my PhD application.

Finally, I thank Prof. Philip Walther for his prompt willingness to co-supervise my defense.

Abstract

Exploring the classical to quantum transition at ever-increasing mass scales is the key goal in modern physics. With precise control over the translational and rotational degrees of levitated nanoparticles in ultra-high vacuum, these particles are promising candidates for probing quantum mechanical behavior. We aim to operate interference experiments with masses around 10^7 amu, which would increase the current mass limit by three orders of magnitude and the macroscopicity by more than five orders. In current state-of-the-art experiments, the maximal achieved delocalization of the particles on the order of 100 pm exceeding the zero-point motion. For coherence length over the particle extent, rotational interference schemes like rotational revivals or tennis racket flips have been proposed. They require both translational and rotational quantum control beyond the particle, ensuring a defined position and orientation. This is achieved by cooling the motion in its quantum regime. While translational ground state cooling has already been performed in one and two dimensions, the ground state in the system's librational modes remains outstanding. However, this is not crucial for performing rotational interference.

In our experiment, we explicitly investigate the rotational optomechanics in a high-finesse cavity with coherent scattering cooling. Therefore, we launch non-spherical silica nanoparticles using laser-induced acoustic desorption and trap them in an optical tweezer and along the standing wave of the cavity.
We characterize the particle asymmetry by evaluating its translational damping and determine its shape. Based on the analysis, we trap nano-dumbbells consisting of two anisotropic spheres stuck together. Determined by the shape, the particle orients inside the elliptical polarized trap, leading to librational motion. We detect two librational modes directly, and we can modulate their frequencies by the tweezer ellipticity. At pressures below 1 mbar, the librational modes couple through the third diffusive rotation, forming two hybrid modes. From the resulting frequency separation, we obtain the rotation frequency, characterizing the undetected mode. We observe this free evolution destabilizing the x- and y-motion, rendering the transfer to high-vacuum challenging. To address this, we optically drive rotation around the tweezer axis to stabilize the particle's orientation.
Scattered light from the particle populates the initially empty cavity. Depending on the degrees of freedom, the particle motion couples to one of the two orthogonally polarized cavity modes. By blue-detuning the cavity modes with respect to the optical tweezer, Anti-Stokes scattering is enhanced, and carries away motional energy. We observe the coupling of five degrees of freedom to their respective mode and demonstrate three-dimensional translational cooling. At a pressure of 10^{-4} mbar, we achieve final temperatures of 36 mK, 129 mK and 105 mK for the z-, x-, y-motion respectively, corresponding to an occupation number in each mode of $\sim 20 \times 10^3$. The final temperature is primarily limited due to laser phase noise. We overcome this limit by phase noise reduction around the relevant particle frequencies using an unbalanced Mach-Zehnder interferometer. According to our simulation, this will enable ground state cooling along the two observed librational degrees of freedom, in the near future.

Zusammenfassung

Einer der Hauptforschungsschwerpunkte in moderner Physik liegt darin, den Übergang zwischen klassischer Physik und der Quantenmechanik zu beschreiben. Nanoteilchen, die mit hoher Präzision in ihrer Translations- und Rotationsbewegung gesteuert werden können, haben sich als vielversprechend erwiesen, quantenmechanischem Verhalten an schweren Objekten mit ungefähr 10^7 amu zu beobachten. Interferenz-Experimente mit diesen Teilchen würden den aktuellen Massenrekord um drei und die Makroskopizität um mehr als fünf Größenordnungen erhöhen. In aktuellen Experimenten mit modernstem Stand der Technik hat man es geschafft, diese Teilchen über 100 pm zu delokalisieren, was ihre Nullpunktsschwingung übertrifft. Um die Teilchen über ihre gesamte Ausdehnung zu delokalisieren wurden Rotations-Interfenz-Experimente vorgeschlagen, die die Quantelung des Drehimpulses ausnutzen, und die daraus resultierende periodische Wiederholung der Orientierung. Die Realisierung der Experimente erfordert die quantenmechanische Kontrolle über sowohl die Translationen als auch die Rotationen des Teilchens, so dass Position und Orientierung definiert werden können. Bisher ist es gelungen, die Translationen in einer und zwei Dimensionen in ihren jeweiligen Grundzustand zu kühlen. Der Grundzustand in allen sechs Dimensionen konnte bisher noch nicht nachgewiesen werden, ist aber auch für die Interferenz-Experimente nicht notwendig.
In unserem Experiment widmen wir uns der Rotationsmechanik im Feld der Optomechanik und verwenden einen optischen Resonator für Kühlversuche mit kohärent gestreutem Licht. Dazu laden wir Siliziumdioxid Teilchen in eine optische Pinzette, indem wir sie durch einen Laserpuls von einer Probe lösen. Danach werden sie innerhalb der stehenden Welle des optischen Resonators positioniert.
Über die Dämpungsverhältnisse der Teilchenbewegung schließen wir auf dessen Asymmetrie. Unsere Analyse hat ergeben, dass wir hantelförmige Teilchen, die aus zwei sphärischen anisotropen Teilchen bestehen, fangen. Abhängig von ihrer Form orientieren sich die Teilchen innerhalb der elliptisch polarisierten Falle und beginnen um ihre Ausrichtung zu librieren. Wir beobachten zwei der drei Librationen direkt und können ihre Frequenz über die Elliptizität modulieren. Bei Drücken unterhalb von 1 mbar beobachten wir, dass die beiden Librationen über die dritte diffusive Rotation koppeln und daher hybride Moden entstehen. Aus der resultierenden Frequenzaufspaltung bestimmen wir die Rotationsfrequenz der nicht sichtbaren dritten Rotationsmode. Außerdem stellen wir fest, dass die freie Rotation die x- und y-Bewegung des Teilchens destabilisiert, sodass der Übergang in Hoch-Vakuum schwierig ist. Um dies zu verhindern und die Teilchen Orientierung zu stabilisieren, lassen wir es zusätzlich um die z-Achse rotieren.
Vom Teilchen gestreutes Licht besetzt den zunächst leeren Resonator. Abhängig vom Freiheitsgrad koppelt die Teilchenbewegung an eine der zwei orthogonalen Polarisationsmoden des Resonators. Wird dieser zusätzlich in Bezug zur optischen Falle blau-verstimmt, verstärkt er Anti-Stokes-Streuung. Dies führt dazu, dass die Bewegungsenergie des Teilchens reduziert wird. Damit haben wir es geschafft, alle drei Translationsfreiheitsgrade gleichzeitig zu kühlen. Bei einem Druck von 10^{-4} mbar haben wir eine finale Temperatur der z-, x- und y-Bewegung von 36 mK, 129 mK und 105 mK erreicht, was einer

Besetzungsszahl von ungefähr $20 \cdot 10^3$ entspricht. Diese ist hauptsächlich durch Phasenrauschen des Lasers limitiert. Wir haben es geschafft, diesen mithilfe eines nicht ausgeglichenen Mach-Zehnder Interferometer lokal um die Teilchen Frequenzen um 20 dB zu senken. In Simulationen haben wir gezeigt, dass es dadurch schon bald möglich ist, die beiden beobachteten Librationen in ihren jeweiligen Grundzustand zu kühlen.

Contents

CHAPTER 1

Introduction

In modern physics, a primary research focus lies in exploring the transition from classical to quantum mechanical behavior. Probing quantum mechanical dynamics at ever-increasing mass scales becomes one of the key targets in current state-of-the-art experiments. Recently, nanoparticles have emerged as promising candidates. These particles can be trapped in a tightly focused optical beam, known as an optical tweezer, a technique pioneered by Arthur Ashkin in 1986 [1, 2]. Optical levitation revolutionized the studies of light-matter interaction, allows the particle to levitate from its surrounding environment without being clamped to a physical system. Thus, enhancing the isolation by operating in low pressure regimes, it leads in combination with a high trapping frequency to high quality oscillators [3].

Optically trapped particles offer an ideal platform for investigating quantum mechanical behavior, and hold promise for high sensitive measurements like acceleration sensing [4–6], or quantum gravitational effects [7–9]. Their versatility in size and shape renders them especially suitable for rotational experiments. Initial studies gain control over the rotational motion by manipulating the polarization and adjusting the trapped rotor dimensions [10]. This sparks greater interests in rotating particles for applications such as torque sensing [11–15] and micro-gyroscopes [16].
Experiments have demonstrated that nano-dumbbells and even single particles can rotate at GHz frequencies in high vacuum [17, 18]. Thus, their torque sensitivity is high enough to measure effects like the Casimir torque near a birefringent crystal [19] and vacuum frictional torques [20]. However, these experiments require a tight alignment of the particle orientation, and thus motional cooling is essential. Non-spherical particles possess three translational, describing the center of mass (CoM) motion, and three rotational degrees of freedom. Inside an optical tweezer, the rotational motions can be trapped, leading to small oscillations around the equilibrium angles, which are called librations. In contrast to the CoM motion, the librational motion couples to the tweezer polarization. Thus, allowing to manipulate and even cool them independently [21]. While cooling, the motional temperature decreases and finally converges to zero. When the motional occupation is below unity, the system mode is in its ground state. Unlike atom cooling, where internal structures are accessible, nanoparticle cooling requires adapted techniques. Cooling schemes are generally categorized as either active or passive. Active cooling includes adapting the trapping potential according to the current particle position. For example, parametric feedback cooling modifies the trapping power of the tweezer and has cooled the translational [22–24] as well as the librational [25] motion to millikelvins. In the case, the trapped particles carry net charges, electric feedback cooling can be applied [26–28]. In combination with a quantum limited measurement and a real time state estimation, one dimensional ground state cooling has been realized [29–31]. Passive cooling schemes like coherent scattering cooling have the ability to cool the motion even without monitoring the particle position in real time [32]. Their key element is an optical cavity with a narrow

linewidth. It is detuned that the cavity response function enhances Anti-Stokes scattering, and thereby reduces the motional energy. Originally, coherent scattering was developed for atom cooling [33, 34] and then extended to levitated nanoparticles [35]. With this technique, ground state cooling in one [36] and even two dimensions [37, 38] has been achieved. Although the theoretical works have proven that the coupling induced by the cavity is strong enough to simultaneously cool all degrees of freedom, the six dimensional ground state is still outstanding [21, 39]. Currently, the translational motion is limited to hundreds of microkelvins and the librational modes to tenth of millikelvins [40]. Ultimately, these experiments pave the way towards complete quantum control over the trapped nanoparticle.
Explicitly revealing the quantum nature of these nanoparticles ($10^7 - 10^{10}$amu) in interference experiments, delocalizing it over the object extent, has not been realized. The heaviest observed objects in matter-wave interference are molecules with masses beyond 25 kDa, consisting of up to 2 000 atoms [41]. The state-of-the-art for nanoparticles is a coherence length on the order of 100 pm exceeding the zero-point motion [42]. However, there are different proposals suggesting spatial interference experiments [43] and rotational interference [44–46]. For rotational interference, schemes like rotational revivals [45] and quantum tennis racket flips [46] could witness quantum mechanical behavior using a single nanoparticle, rendering it especially suitable for levitated optomechanics. In order to conduct these experiments, it is crucial to investigate their librational behavior and cool it into the quantum regime, while not necessitating the quantum ground state.
The scope of this thesis is to present fundamental work investigating the librations and rotations of trapped silica particles and implement coherent scattering cooling for translational and librational cooling. In Chapter 2 we review the mathematical framework of the interaction between the optical tweezer and the trapped nanoparticle. Thereby, we focus on non-spherical shaped particles and their ability to librate within the tweezer potential. As the motion is highly dependent on the particle shape, we reconstruct it based on the measured data (see Chapter 3). Further, we investigate the motion with different detection techniques. In the second part of this thesis in Chapter 4, we provide a detailed description of coherent scattering cooling and experimentally demonstrate the CoM cooling. We studied the coupling between particle and cavity and particularly focus on the cooling limits. Further, we present a way to reduce phase noise heating locally and based on this simulate the cooling with experimentally feasible parameters.

CHAPTER 2

Theory of rotational optomechanics

The expression 'optomechanics' denotes the interconnection between the classical optical field and the mechanical motion. We study the field by investigating the light coupling to a nanoscale object. In particular, we focus on rational motion, which is inherent with the particle shape. The scope of this chapter is to present an overview of the fundamental concepts that underpin light-mater interactions at the nanoscale. A key element is a tightly focused light beam, known as an optical tweezer, which is capable to trap nanoparticles. We provide a general description of the motion for a trapped particle concerning all six degrees of freedom that a rigid body can have.

2.1 Optical tweezer

A nanoscale object, which consists of many atoms or molecules, can be treated macroscopically. Thus, the object is assigned with a charge density ρ and a current density $\mathbf{j}$, which in turn provide a polarizability and a magnetization. Given that the particle size is small compared to the wavelength of an external optical field, the dipolar approximation is applicable [47]. Over the extent of the particle, the optical field is assumed to be homogenous. In its presence, the electric and magnetic fields induce a dipole moment $\mathbf{p}$ through the polarizability α, which gives rise to the Lorentz force [48]

$$\mathbf{F} = (\mathbf{p}\nabla)\mathbf{E} + \mathbf{p} \times (\nabla \times \mathbf{E}) + \frac{\mathrm{d}}{\mathrm{d}t}(\mathbf{p} \times \mathbf{B}) \tag{2.1}$$

$$= \sum_q p_q \nabla E_q + \frac{\mathrm{d}}{\mathrm{d}t}(\mathbf{p} \times \mathbf{B}). \tag{2.2}$$

For the sake of simplicity, we switch to the index notation where $q \in \{x, y, z\}$ holds. Based on this fundamental relation between nanoscale matter and an external light field, we derive a time averaged force such that the last term drops. The cyclic average ensures the force

$$\langle \mathbf{F} \rangle = \sum_q \langle p_q^* \nabla E_i \rangle = \frac{1}{2} \sum_q \Re\{p_q^* \nabla E_q\} \tag{2.3}$$

to be real. For the dipole moment $\mathbf{p}$ we insert the relation

$$\mathbf{p} = \varepsilon_0 V \chi \mathbf{E} = \alpha \mathbf{E} \tag{2.4}$$

where χ represents the electrical susceptibility and V describes the particle volume, multiplied with the vacuum permittivity ε_0 this ultimately results in the polarizability α. It should be noted that the susceptibility is in general a tensor of rank two, describing the particle response to the external electric field depend on the particle axis. For isotropic particles like spherical ones without impurities, the susceptibility is in all spatial directions identical, thereby becoming a scalar. In general, the polarizability can be expressed as a sum of two terms [49]

$$\alpha = \alpha' + \mathrm{i}\alpha'', \tag{2.5}$$

where the real part describes the dispersive contribution and the imaginary part accounts for the dissipative component. In this context, the polarizability is consistent with the Clausius-Mossotti relation for a particle in vacuum

$$\alpha' = 3\varepsilon_0 V \frac{n^2 - 1}{n^2 + 2}, \tag{2.6}$$

where n is the refractive index of the particle. We insert the polarizability relation back in Equation 2.3 and separate the Force accordingly

$$\langle \mathbf{F}_{\mathrm{grad}} \rangle = \frac{1}{2} \sum_q \Re\{E_q^* \alpha' \nabla E_q\} = \frac{1}{4} \nabla (\mathbf{E}^* \alpha' \mathbf{E}) \tag{2.7}$$

$$\langle \mathbf{F}_{\mathrm{scat}} \rangle = \frac{1}{2} \sum_q \Im\{E_q^* \alpha'' \nabla E_q\}, \tag{2.8}$$

where we introduce the gradient force as the real and the scattering force as the imaginary part. The imaginary part of α is not consequently zero if the particle is lossless.

In an optical field, the gradient force points toward the region of maximal intensity. This allows for the utilization of a highly focused laser beam as an optical trap, called an optical tweezer [1]. While the radiation pressure pushes the particle along the **k**-vector, the trapping position is displaced from the intensity maximum. In order to achieve stable trapping, it is necessary to compensate for the scattering force. This can be achieved either by the gradient force itself or by setting up a double-sided tweezer, whereby the focused light is back-reflected, leading to a standing wave. As an alternative approach, the scattering force can be reduced in an upside down system, where the gravity counteracts the scattering force [18].
Since the gradient force is conservative, we can define a potential

$$U(\mathbf{r}) = -\frac{1}{4} \mathbf{E}_t^*(\mathbf{r}) \alpha' \mathbf{E}_t(\mathbf{r}), \tag{2.9}$$

at the position **r**. To determine the potential shape at the particle location, we suppose the optical field propagating along the z-direction with a transversal Gaussian profile

$$\mathbf{E}_t(\mathbf{r}) = E_0 f_t(\mathbf{r}) \mathrm{e}^{\mathrm{i}\omega t} \mathbf{e}_t, \tag{2.10}$$

wherein the spatial dependency is stored in the mode function $f_t(\mathbf{r})$ and the prefactors summarized in E_0. The electric field oscillates with frequency ω and is polarized along $\mathbf{e}_t$. The mode function encompasses

the Gaussian shape

$$f_c(\mathbf{r}) = \frac{1}{1 + z^2/z_R^2} \exp\left\{\frac{-x^2}{w_x(z)^2} + \frac{-y^2}{w_y(z)}\right\} \exp\left\{\mathrm{i}\left(kz - \phi(\mathbf{r})\right)\right\} \tag{2.11}$$

with $\phi(\mathbf{r})$ being the Gouy phase describing the phase shift at the particle position. The waists of the Gaussian beam scale depend on the position along the propagation direction

$$w_{x,y}(z) = w_{x,y}\sqrt{1 + \frac{z^2}{z_R^2}} \tag{2.12}$$

with their minimal waists at $z = 0$. As we distinguish between the waists corresponding to the x- and y-direction and allow them to differ we approximate the Rayleigh length as $z_R \approx w_x w_y \pi/\lambda$ [21]. The remaining prefactor E_0 sums up all constant terms

$$E_0 = \sqrt{\frac{4P}{c\varepsilon_0 \pi w_x w_y}} \tag{2.13}$$

and is related to the optical power P.
We insert the expression for the electric field in Equation 2.9. As long as we consider a scalar polarizability, we do not need to specify the tweezer polarization further. Hence, we end up with the expression for the potential as

$$U(\mathbf{r}) = -\frac{\alpha'}{4} E_0^2 \exp\left\{\frac{-2x^2}{w_x(z)^2} + \frac{-2y^2}{w_y(z)^2}\right\}. \tag{2.14}$$

Given our interest in how the potential affects the particle motion, we expand the potential around its initial position. Since the particle is trapped in the focus, its location is $\mathbf{r} = (0, 0, 0)$ when the scattering force contribution is ignored. For small displacements of the particle along the spatial directions, we expand the potential in a Taylor series

$$U(\mathbf{r}) = -\frac{1}{2} \times \frac{2\alpha' P}{c\varepsilon_0 \pi w_x w_y}\left(1 - \frac{2x^2}{w_x^2} - \frac{2y^2}{w_y^2} - \frac{z^2}{z_R^2} + O(\mathbf{r}^4)\right). \tag{2.15}$$

In first approximation, the tweezer potential is of the form $U(\mathbf{r}) = k\mathbf{r}^2/2$. Hence, we can treat the particle motion inside the trap as a harmonic oscillator with the frequencies $\Omega_{z,x,y} = \sqrt{k_{z,x,y}/m}$, where m is the nanoparticle mass. Consequently, the particle translational frequencies

$$\Omega_z = \frac{\lambda}{\pi(w_x w_y)}\sqrt{\frac{2\alpha' P}{mc\varepsilon_0 \pi w_x w_y}}, \tag{2.16}$$

$$\Omega_x = \frac{1}{w_x}\sqrt{\frac{4\alpha' P}{mc\varepsilon_0 \pi w_x w_y}}, \tag{2.17}$$

$$\Omega_y = \frac{1}{w_y}\sqrt{\frac{4\alpha' P}{mc\varepsilon_0 \pi w_x w_y}} \tag{2.18}$$

are dependent upon the potential stiffness, which can be manipulated by the optical parameters, including the waists, wavelength, and optical power. We conclude the particle motion along the translational directions to be three independent harmonic oscillations around the equilibrium position $\mathbf{r} = (0, 0, 0)$.

2.1.1 Equations of motion

We proceed to examine the dynamics of the CoM motion. It is therefore necessary to consider the particle in the context of its surrounding environment. In the addition to the coupling to the optical potential, the particle also interacts with the surrounding gas, thereby perturbing the oscillation. We state the tweezer and particle to be in vacuum around intermediate pressure (millibar), where the optical forces dominate the Stoke drag forces [50]. The environment treated as a thermal gas thermalizes the particle motion at the bath temperature $T = 300\,\mathrm{K}$. The interaction results from collisions between the particle and the gas molecules, exerting a friction γ and a thermal force F_{th}. Hence, the differential equation of motion for the direction of motion $q \in \{x, y, z\}$ is

$$\ddot{q}(t) + \Gamma_m \dot{q}(t) + \Omega_q^2 q(t) = \frac{F_{\mathrm{th}}(t)}{m_q}, \tag{2.19}$$

where we use the abbreviation $\Gamma_m = \Gamma/m$. In the event that the interaction with the thermal bath is assumed to be Gaussian and Markovian limited, meaning that it introduces a white noise the thermal force arises from the fluctuation-dissipation theorem [51, 52]

$$F_{\mathrm{th}} = \sqrt{2mk_BT\Gamma_m}\xi(t) \tag{2.20}$$

with $\xi(t)$ fulfilling the relation

$$\langle \xi(t_1)\xi(t_2)\rangle = \delta(t_1 - t_2). \tag{2.21}$$

In order to solve the equation of motion 2.19, it is necessary to Fourier transform the problem $\mathcal{F}[q(t)] = \tilde{q}(\omega)$

$$\tilde{q}(\omega) = \frac{1}{\Omega_q^2 - \omega^2 - \mathrm{i}\Gamma_m\omega} \times \frac{\tilde{F}_{\mathrm{th}}}{m_q} = \chi_m(\omega)\frac{F_{\mathrm{th}}}{m_q}, \tag{2.22}$$

where χ_m denotes the mechanical susceptibility. We calculate the power spectral density (PSD) of the position coordinate q

$$S_{qq}(\omega) = \int \langle \tilde{q}(\omega)\tilde{q}(\omega')\rangle \mathrm{d}\omega. \tag{2.23}$$

Accordingly, the PSD of Equation 2.22

$$S_{qq}(\omega) = \frac{2k_BT\Gamma_m/m}{\left(\Omega_q^2 - \omega^2\right)^2 + \Gamma^2\omega^2} = \frac{k_BT}{m\Omega_q^2} \times 2|\chi_m|^2\Gamma_m\Omega_q^2 \tag{2.24}$$

describes a Lorentzian shaped function, which is peaked at Ω_q for satisfying $\Omega_q \gg \Gamma_m$. Furthermore, the PSD is proportional to the temperature and thus the ratio of thermal and mechanical energy $k_BT/\hbar\Omega_q^2$.

2.2 Rotations and librations

We extend the discussion about the motion of a nanoparticle in the optical potential to anisotropic particles, meaning their susceptibility is spatial dependent. The anisotropy is not caused by impurities inside the particle but by a non-spherical shape. Thus, the susceptibility becomes a tensor of rank two, and in the particle frame it is diagonal

$$\chi_{\text{particle}} = \begin{pmatrix} \chi_a & 0 & 0 \\ 0 & \chi_b & 0 \\ 0 & 0 & \chi_c \end{pmatrix}, \tag{2.25}$$

where without loss of generality $\chi_a < \chi_b < \chi_c$ holds. While the tweezer and the optical potential is given in the laboratory frame, we transform the susceptibility by using an Euler transformation in the z-y'-z'' convention. The transformation is shown in Figure 2.1, where the laboratory frame (red) converts to the particle frame (black). First, it is rotated around the z-axis by the angle α. This changes the orientation of the x and y coordinates but leaves z unaffected. The second rotation, rotates the frame around the new y' axis, followed by a final rotation around the new z'' axis. Mathematically, the

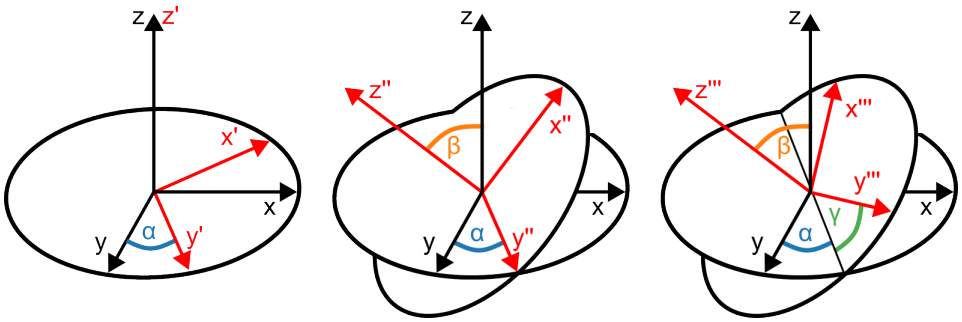

Figure 2.1: Transformation of the tweezer frame (red) to the particle fixed frame (black). The rotations are described by the Euler angles α, β, γ in the z-y'-z'' convention.

transformation is expressed multiplying the three rotation matrices which results in

$$R_{zy'z''} = \begin{pmatrix} \cos(\alpha)\cos(\beta) - \sin(\alpha)\sin(\gamma) & -\cos(\alpha)\cos(\beta)\sin(\gamma) - \sin(\alpha)\cos(\gamma) & \cos(\alpha)\sin(\beta) \\ \sin(\alpha)\cos(\beta)\cos(\gamma) + \cos(\alpha)\sin(\gamma) & -\sin(\alpha)\cos(\beta)\sin(\gamma) + \cos(\alpha)\cos(\gamma) & \sin(\alpha)\sin(\beta) \\ -\cos(\gamma)\sin(\beta) & \sin(\gamma)\sin(\beta) & \cos(\beta) \end{pmatrix} \tag{2.26}$$

with the angles α, β and γ, also known as the Euler angles. With this transformation we convert the susceptibility tensor from the particle in the laboratory frame

$$\chi = R_{zy'z''}\chi_{\text{particle}}R^{\top}_{zy'z''}, \tag{2.27}$$

in fact it is more convenient to describe the orientation of the particle inside the trap and not vice versa. The resulting components depending on the Euler angles $\Omega = (\alpha, \beta, \gamma)$ are calculated in the Appendix A. Beside the different susceptibilities, the particle features also three distinct moments of inertia $I_{\text{particle}} = \text{diag}(I_a, I_b, I_c)$. Its tensor is transformed accordingly.

As the particle is asymmetric, its rotations become relevant. Therefore, we find a Lagrangian representing the free rotation and subsequently derive the Hamiltonian of the system. In absence of a

potential the Lagrangian of motion is given by the rotational energy

$$\mathcal{L}_{\text{rot}} = \frac{1}{2}(\omega^{\top} I \omega), \tag{2.28}$$

where the frequency ω depends on the Euler angles following this relation:

$$\begin{pmatrix} \omega_a \\ \omega_b \\ \omega_c \end{pmatrix} = \begin{pmatrix} 0 & -\sin(\alpha) & \cos(\alpha)\sin(\beta) \\ 0 & \cos(\alpha) & \sin(\alpha)\sin(\beta) \\ 1 & 0 & \cos(\beta) \end{pmatrix} = \begin{pmatrix} \dot{\alpha} \\ \dot{\beta} \\ \dot{\gamma} \end{pmatrix}. \tag{2.29}$$

In order to derive the Hamiltonian we determine the canonical momenta using the relation

$$p_q = \frac{\partial \mathcal{L}}{\partial \dot{q}}, \tag{2.30}$$

which then yields

$$\begin{aligned} p_\alpha = {} & \dot{\alpha}\sin(\beta)^2\left(I_a\cos(\gamma)^2 + I_b\sin(\gamma)^2 + I_c\cot(\beta)^2\right) + \dot{\beta}(I_b - I_a)\sin(\beta)\sin(\gamma)\cos(\gamma) \\ & + \dot{\gamma} I_c \cos(\beta), \end{aligned} \tag{2.31}$$

$$p_\beta = \dot{\alpha}(I_b - I_a)\sin(\beta)\sin(\gamma)\cos(\gamma) + \dot{\beta}\left(I_a\sin(\gamma)^2 + I_b\cos(\gamma)^2\right), \tag{2.32}$$

$$p_\gamma = I_c\left(\dot{\alpha}\cos(\beta) + \dot{\gamma}\right) \tag{2.33}$$

a set of coupled differential equations. Although the rotational modes in the laboratory frame are highly coupled at the angle $\Omega = (0, \pi/2, 0)$ the angular momenta decouple, which results in

$$p_\alpha = \dot{\alpha} I_a, \qquad p_\beta = \dot{\beta} I_b, \qquad p_\gamma = \dot{\gamma} I_c. \tag{2.34}$$

For the following discussion the orientation $\Omega = (0, \pi/2, 0)$ and the position $\mathbf{r} = (0, 0, 0)$ are referred to be the steady-state solution. When inserting the orientation in Figure 2.1, the particle z-axis overlaps with the tweezer x-axis.
The Hamiltonian of the free evolution conducting the translational motion and the rotational reduces to

$$H_N = \sum_q \frac{p_q^2}{2m_q} \tag{2.35}$$

with $q \in \{x, y, z, \alpha, \beta, \gamma\}$. For clarity, the correspondences $m_{x,y,z} = m$ and $m_{\alpha,\beta,\gamma} = I_{a,b,c}$ hold.

2.2.1 Optical torques

Inside the optical tweezer, the free rotation is perturbed by interaction with the optical potential, creating an optical torque. This torque tends to align the dipole in the electric field. The mathematical expression is derived similarly to Equation 2.1. By integrating Maxwell's stress tensor over the surface of the sphere and time averaging the solution, the angular momentum of the field is removed [21, 48]. The calculated

optical torque results in [53],

$$\tau_{\text{opt}} = \frac{1}{2}\Re\{\mathbf{p} \times \mathbf{E}^*_{\text{tot}}\}, \tag{2.36}$$

whereby the total electric field describes both the incoming tweezer field and subsequently the scattered field of the particle. Thus, we decompose the torque in two parts

$$\tau_{\text{opt}} = \tau_d + \tau_{\text{self}}, \tag{2.37}$$

with τ_d stemming from the tweezer field. This torque overcomes the self-induced torque, that arises from the back-action of the scatter field. It can be seen that τ_{self} will become relevant if τ_d vanishes, which is the case when the dipole axis aligns with the tweezer polarization ($\mathbf{p} \parallel \mathbf{E}_t$). Consequently, we define the tweezer polarization as

$$\mathbf{e}_t = \begin{pmatrix} \cos(\psi) \\ \mathrm{i}\sin(\psi) \\ 0 \end{pmatrix} \tag{2.38}$$

where the angle ψ describes the tweezer ellipticity in the range $\psi \in [0, \pi/4]$. For $\psi = 0$ the tweezer is linearly, and for $\psi = \pi/4$ circularly polarized. Taking the electric field of the tweezer as defined in Equation 2.10 into account, we calculate the resulting torque

$$\tau_d = \frac{1}{2}\left|E_0 f_t(\mathbf{r})\right|^2 \Re\left\{\varepsilon_0 V \chi \mathbf{E}_t \times \mathbf{E}_t^*\right\}. \tag{2.39}$$

After transforming in the laboratory frame the torque is given by

$$\tau_d = \frac{1}{2}\varepsilon_0 V |E_0|^2 \Re\left\{\begin{pmatrix} -\mathrm{i}\chi_{31}\sin(\psi)\cos(\psi) - \chi_{32}\sin(\psi)^2 \\ \chi_{31}\cos(\psi)^2 - \mathrm{i}\chi_{32}\sin(\psi)\cos(\psi) \\ \mathrm{i}(\chi_{11} - \chi_{22})\cos(\psi)\sin(\psi) - \chi_{12}\cos(2\psi) \end{pmatrix}\right\}, \tag{2.40}$$

where the susceptibility tensor is assumed to be symmetric $\chi = \chi^\top$. Since the entries of the susceptibility tensor are dependent on the Euler angles, the torque is related to the particle orientation. We evaluate the torque in linear order around the steady-state orientation by Taylor expanding the susceptibility components (cf. Appendix A), e.g.

$$\begin{aligned} \chi_{12} &\approx \chi_a(\alpha(-\beta) + \gamma)(-\beta - \alpha\gamma) + \chi_b(-\alpha + 1)(\beta\gamma - \alpha) + \chi_c\alpha && (2.41) \\ &= (\chi_c - \chi_b)\alpha + O(qq'). && (2.42) \end{aligned}$$

Thus, we come up with a linearized optical torque

$$\tau_d = -\frac{1}{2}\varepsilon_0 V |E_0|^2 \begin{pmatrix} \sin(\psi)^2\left(\chi_b - \chi_a\right)\gamma \\ \cos(\psi)^2\left(\chi_c - \chi_a\right)\beta \\ \cos(2\psi)\left(\chi_c - \chi_b\right)\alpha \end{pmatrix} \tag{2.43}$$

describing a restoring torque along all spatial directions. In analogy to the translational, the restoring torque results in a harmonic motion around the equilibrium orientation $\boldsymbol{\Omega}$.

2.2.2 Libration

The harmonic oscillation around a steady-state angle is called a libration, and can be treated in a manner analogous to the translational description. According to Hook's law, the torque τ_d is determined by the stiffness k_q for each degree of freedom

$$\tau_{\mathrm{d}} = -\begin{pmatrix} k_\gamma \gamma \\ k_\beta \beta \\ k_\alpha \alpha \end{pmatrix}, \tag{2.44}$$

which consequently leads to the frequencies $\Omega_q = \sqrt{k_q/m_q}$ with $q \in \{\alpha, \beta, \gamma\}$. The calculated librational frequencies are

$$\Omega_\alpha = \sqrt{\frac{2P}{c\varepsilon_0 \pi w_x w_y} \varepsilon_0 V \frac{(\chi_c - \chi_b)}{I_a} \cos(2\psi)} \tag{2.45}$$

$$\Omega_\beta = \sqrt{\frac{2P}{c\varepsilon_0 \pi w_x w_y} \varepsilon_0 V \frac{(\chi_c - \chi_a)}{I_b} \cos(\psi)^2} \tag{2.46}$$

$$\Omega_\gamma = \sqrt{\frac{2P}{c\varepsilon_0 \pi w_x w_y} \varepsilon_0 V \frac{(\chi_b - \chi_a)}{I_c} \sin(\psi)^2}. \tag{2.47}$$

In perspective of the laboratory frame, the torque along the z-axis enables the particle to oscillate in the x-y plane. This corresponds to a libration around the steady-state orientation of the Euler angle α. For simplicity this motion is called α-libration with its corresponding frequency Ω_α. Accordingly, we define the remaining two oscillations as β- and γ-libration.
Further, we can predict the particle aligning inside the tweezer. Therefore, we suppose a linear polarized ($\psi = 0$) beam, the torque along the polarization direction (x-axis) disappears, which causes an undefined orientation in the orthogonal z-y plane. As a result, the γ-oscillation evolves freely thus, the particle axis with the smallest susceptibility χ_c is not confined with the optical trap. Instead, the particle z-axis with the strongest susceptibility aligns with the tweezer polarization axis that we conclude the particle axis with the highest polarizability aligns with the strongest polarization axis.
As previously discussed in the context of the translations, the particles do not couple solely to the light field. They also interact with their environment by collisions, which give rise to a stochastic thermal-torque τ_{th}. The white noise torque is Gaussian distributed in magnitude and in middle zero that the relation [11, 12, 18]

$$\langle \tau_{\mathrm{th}}(t_1) \tau_{\mathrm{th}}(t_2) \rangle = 2 m_q \Gamma_q k_{\mathrm{B}} T \delta(t_1 - t_2) \tag{2.48}$$

holds. The equation of librational motion yields

$$\ddot{q} + \Gamma_q \dot{q} + \Omega_q^2 q = \frac{\tau_{\mathrm{th}}}{m_q}. \tag{2.49}$$

Now, we need to treat the damping carefully, and generalize $\Gamma_q = \Gamma/m_q$ as the moment of inertia differ for each degree of freedom. Since the description is similar to the translational Equation 2.19, we

determine the PSD for the librational motion

$$S_{qq}(\omega) = \frac{2k_B T\Gamma_q/m_q}{\left(\Omega_q^2 - \omega^2\right)^2 + \Gamma_q^2\omega^2} \tag{2.50}$$

to be a Lorentzian function as well.
Additionally, as we determined the translational frequencies in Equation 2.16 we supposed a spherical shape, we can now generalize them by replacing the polarizability with

$$\alpha' = \varepsilon_0 V(\chi_c \cos(\psi)^2 + \chi_b \sin(\psi)^2). \tag{2.51}$$

Overall, the CoM motion as well as the librations for an aspherical particle are described by six independent harmonic oscillators in an elliptical tweezer potential. As a remark, we consider only lossless particles exhibiting an anisotropy regarding the polarization to experience an optical torque. Particles that feature impurities or are capable to absorb a photon, undergo torques as well. When every motion is confined as a harmonic oscillation we call the particle deeply trapped with the steady-state position $\mathbf{r} = (0, 0, 0)$ and orientation $\Omega = (0, \pi/2, 0)$.

2.2.3 Rotation

In the case, where the tweezer is circularly polarized ($\psi = \pi/4$) the restoring torque along the z-axis drops (Equation 2.43). Therefore, the α-libration is not defined, which allows for a free evolving rotation. Despite the tweezer induced torque cancels, the self-induced torque does not necessarily disappear, too. In this case, we need to consider the back-action of the scattered light and therefore calculate the scattered field, which we express in terms of the dyadic Green's function [54]

$$\mathbf{E}_{\text{scat}} = \frac{\omega^2}{\varepsilon_0 c^2}\mathbf{G}\mathbf{p}. \tag{2.52}$$

In the near field approximation the dyadic Green's function is [48]

$$\mathbf{G} = -\frac{\exp\{\mathrm{i}kR\}}{4\pi R}\frac{1}{k^2R^2}\left(\mathbf{I} + \frac{3\mathbf{R}\mathbf{R}}{R^2}\right) \approx \frac{\mathrm{i}k}{6\pi}\mathbf{I}, \tag{2.53}$$

where $\mathbf{R}$ stands for the position we want to evaluate the field. As we approximate it around, the steady-state position $\mathbf{R}$ is expanded around $\mathbf{r} = (0, 0, 0)$ that the scattered field close to the particle location becomes

$$\mathbf{E}_{\text{scat}} = \frac{k^2}{\varepsilon_0}\mathbf{G}\mathbf{p} \approx \frac{\mathrm{i}k^3 V}{6\pi}\chi\mathbf{E}_t. \tag{2.54}$$

Inserting the scattered field in Equation 2.37 we obtain the self-induced torque. In the case of interest where the tweezer is circularly polarized, the particle experiences

$$\tau_{\text{self}}^z \approx \frac{1}{4}|E_0|^2\frac{\varepsilon_0 V^2 k^3}{6\pi}\chi_b\chi_c \tag{2.55}$$

a constant torque. This results in a driven rotation around the tweezer axis. Combining the optical torques along the x- and y-direction the total optical torque for circularly polarized light reads

$$\tau_{\text{opt}} = \tau_{\text{d}} + \tau_{\text{self}} = -\frac{1}{4}\varepsilon_0 V|E_0|^2 \begin{pmatrix} \gamma\cos(\alpha)\left(\chi_b - \chi_a\right) - \beta\sin(\alpha)\left(\chi_c - \chi_a\right) \\ \beta\cos(\alpha)\left(\chi_c - \chi_a\right) + \gamma\sin(\alpha)\left(\chi_b - \chi_a\right) \\ -\frac{Vk^3}{6\pi}\chi_b\chi_c \end{pmatrix}. \tag{2.56}$$

Due to the absence of a restoring force, the particle begins to rotate, accompanying the β- and γ-libration couple together. A similar effect is observed in the case of linear polarized light, where the γ-libration tends to zero. However, its rotation is not driven by the optical field

$$\tau_{\text{opt}} = -\frac{1}{4}\varepsilon_0 V|E_0|^2 \begin{pmatrix} 0 \\ \beta\left(\chi_c - \chi_a\cos(\gamma)^2 - \chi_b\sin(\gamma)^2\right) + \alpha\left(\chi_b - \chi_a\right)\sin(2\gamma)/2 \\ \alpha\left(\chi_c - \chi_a\sin(\gamma)^2 - \chi_b\cos(\gamma)^2\right) + \beta\left(\chi_b - \chi_a\right)\sin(2\gamma)/2 \end{pmatrix}, \tag{2.57}$$

instead it evolves in a Brownian motion due to the thermal torque (cf. Equation 2.48) [55].
Sticking to the driven rotation, we finally derive the equation of motion

$$\ddot{q} + \Gamma_q\dot{q} = \frac{\tau_{\text{opt}} + \tau_{\text{th}}}{m_q}, \tag{2.58}$$

which has no steady-state orientation. In thermal equilibrium, however, it has a mean rotation frequency

$$\langle\omega_q\rangle = \frac{\tau_{\text{opt}} + \tau_{\text{th}}}{\Gamma_q m_q} \tag{2.59}$$

that is inversely proportional to the damping Γ_q. It can thus be concluded that the trapping light is capable of transferring angular momentum to the nanoparticle, which lead to optical torques. With an elliptically polarized tweezer the particle librates around its equilibrium position $\Omega = (0, \pi/2, 0)$ and as soon as the polarization changes to circularly or linearly polarized light, two librations couple, while the other starts rotating. In the event of circularly polarized light, an optical torque drives the motion constantly.

CHAPTER 3

Characterization of levitated non-spherical nanoparticles

Since the field of levitated optomechanics has an intensified interest in investigating rotating particles, the characterization of the particle shape becomes more important. While asymmetries barely influence the translational motion, they significantly impact the librations. Consequently, in experiments aiming at full rotational control, it is of critical importance to ascertain the type and shape of the trapped particles.

3.1 Experimental setup

The key component of our optical setup is a single sided-optical tweezer, which consists of a strongly focused laser beam, as shown in Figure 3.1. We use an NKT E15 fiber seed laser (linewidth: < 0.1 kHz,

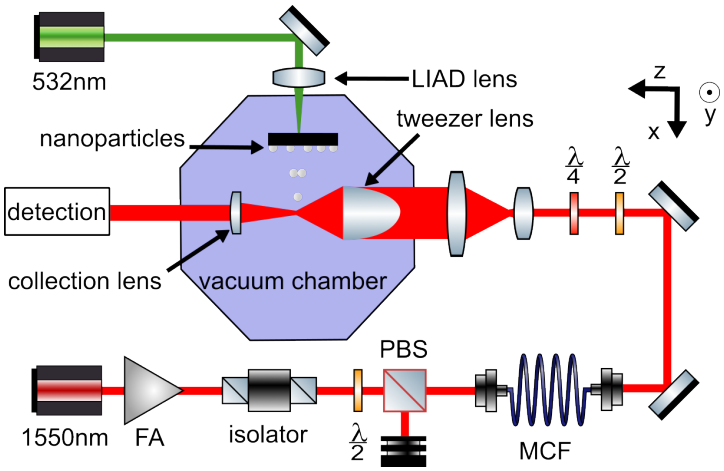

Figure 3.1: Schematic drawing of the employed optical setup feasible for launching silica nanoparticles directly in itermediate vacuum. For trapping the particles, we use a 1 550 nm laser from NKT with a small linewidth. As the mode profile after the amplifier is not Gaussian, the mode cleaning fiber (MCF) restores the profile. In a vacuum chamber capable to reach a minimal pressure around 10^{-9} mbar nanoparticles are loaded in the trap. A green $\lambda = 532$ nm laser is focused on the backside of a sample coated with nanoparticles. The laser waist is approximately 200 µm. The trap is manipulated by regulating the power using the half-wave plate and polarizing beam splitter (PBS), as well as adjusting the polarization with the combination of a half-wave and quarter-wave plate positioned after the MCF. Light scattered from the particle is collected and collimated in forward direction.

$P_{\text{out}} = 40\,\text{mW}$, maximal phase noise at 20 kHz: $0.3\,\mu\text{rad}/\sqrt{\text{Hz}}/\text{m}$) with a wavelength of $\lambda = 1\,550\,\text{nm}$ and its corresponding fiber amplifier, cranking the power to 9 W. After amplification, we send the amplified beam through a mode cleaning fiber to ensure a Gaussian beam for trapping. Deviations will cause unwanted potential deformations, resulting in a non-harmonic trap. The polarization of the trap is controlled using a combination of a quarter and a half-wave plate. Before the vacuum chamber, we expand the beam utilizing a telescope that the diffraction-limited aspherical tweezer lens (NA $= 0.81$, $d = 2.54\,\text{cm}$) is fully illuminated.
We load the trap with silica (SiO_2) nanoparticles using laser-induced acoustic desorption (LIAD). This loading technique is compatible with vacuum, rendering it especially suitable for levitated optomechanics [56]. First established for physical chemistry, the working principle can be extended to nanoparticles and in combination with an optical tweezer successfully applied [57, 58]. The particles diluted in isopropanol are deposit on the front side of a thin plate, here we use a glass slide with a 40 nm thick silicon coating on top. After the isopropanol evaporates, the particles stick to the plate. We place the sample in the focus of a pulsed green laser beam ($\lambda = 532\,\text{nm}, \tau = 9\,\text{ns}, E = 3\,\text{mJ}, w_f = 200\,\mu\text{m}$), illuminating the backside. The light pulses induce an acoustic and thermal wave in the coating. The particles are ablated from the front side, not directly interacting with the laser. As a remark, the ablation process is not fully understood, as it needs to compensate the binding force with an acceleration on the order of $1 \times 10^6\,\text{m/s}^2$. At pressures of approximately $p = 15\,\text{mbar}$ and with a free-fall distance of several millimeters, the particles are slowed to enable stable trapping. For operation, we align the green laser with the tweezer focus, enhancing trapping probabilities, although we observe particles in a wide opening angle [58]. This method represents a cleaner loading technique than nebulization, which is a commonly utilized approach in the field of optomechanics.

3.2 Motional detection in forward scattering

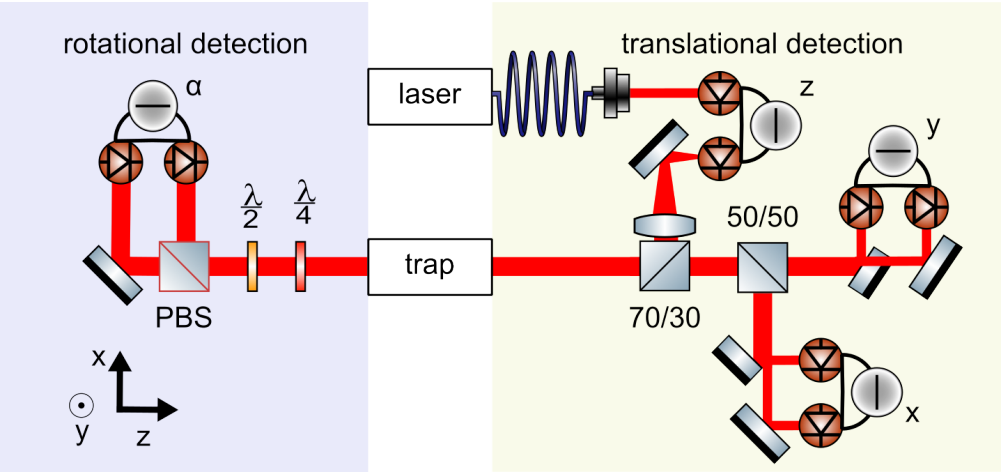

Figure 3.2: Detection of the particle motion in forward scattered light. The detection scheme consists of two parts, a rotational detection; particularly sensitive to the α-libration and rotation and secondly a split detection scheme; sensitive to the translational motion. For the z-detection, we additionally focus the beam to match the active area.

Once a particle is trapped, we observe its motion by collecting forward scattered light, using a collimation lens (NA $= 0.18$) (cf. Figure 3.1). We assume the particle trapped in the potential origin ($\mathbf{r} = (0, 0, 0)$) and stably orientated ($\Omega = (0, \pi/2, 0)$). The induced dipole then radiates a field, which is

modeled with the dyadic Green's function, introduced earlier in section 2.2.1. Here, we now consider its far-field solution, because the detector is approximately half a meter distance from the trapping area. Thereby, the scattered electrical field is given by

$$\mathbf{E}_{\text{scat}}(\mathbf{R}) = k^3 V \frac{\mathrm{e}^{\mathrm{i}kR}}{4\pi kR} \times \begin{pmatrix} 1 - R_x^2/R^2 & -RyRx/R^2 & -R_xR_z/R^2 \\ -R_xR_y/R^2 & 1 - R_y^2/R^2 & -R_yR_z/R^2 \\ -R_zR_x/R_z^2 & -R_zR_y/R^2 & 1 - R_z^2/R^2 \end{pmatrix} \chi \mathbf{E}_t, \tag{3.1}$$

where $\mathbf{R}$ describes the difference between detector and current particle position. If we presume its position close to the optical axis, we can apply the paraxial approach ($R_xR_y \ll R_z$) simplifying the scattered field expression

$$\mathbf{E}_{\text{scat}}(\mathbf{R}) = k^3 V \frac{\mathrm{e}^{\mathrm{i}kR}}{4\pi R} \begin{pmatrix} 1 & 0 & 0 \\ 0 & 1 & 0 \\ 0 & 0 & 0 \end{pmatrix} \chi \mathbf{E}_t = k^3 V E_0 f(\mathbf{r}) \frac{\mathrm{e}^{\mathrm{i}kR}}{4\pi R} \begin{pmatrix} \cos(\psi)\chi_{11} + \mathrm{i}\sin(\psi)\chi_{12} \\ \cos(\psi)\chi_{21} + \mathrm{i}\sin(\psi)\chi_{22} \\ 0 \end{pmatrix}. \tag{3.2}$$

The radiated field, can always be decomposed as a series of spherical waves. The collection lens converts them to plane waves, which maintain their amplitude [50].
Inserting the Gaussian envelope function around the particle position 4.44 and expanding the phase factor $\exp\{\mathrm{i}kR\}$ to the first order, we notice that the scattered light phase depends on the particle motion

$$\phi_{\text{scat}} = -\frac{k}{f}\left(xx' + yy' + zz'\right) + z\left(k - \frac{1}{z_{\text{R}}}\right). \tag{3.3}$$

The primed coordinates refer to the detector position and f denotes the focal length of the collection lens. Due to the small particle size, focused light not necessarily scatter with the particle, which subsequently serve as a reference beam. Through the collection lens, the scattered light is combined with the reference beam. Due to the Gouy-phase this reference beam acquires a phase shift of $\pi/2$ when being tightly focused

$$E_{\text{ref}} = E_t \mid_{\phi=\pi/2} = E_0 f_t(\mathbf{r}) \begin{pmatrix} \mathrm{i}\cos(\psi) \\ -\sin(\psi) \\ 0 \end{pmatrix}. \tag{3.4}$$

To detect the translational motion, we need to measure the scattered field after overlapped with the reference beam. We achieve this with a split detection scheme, as presented in Figure 3.2. The light is divided in three parts for detecting each degree of freedom separately. The two beams utilized for the detection of both the x- and y-motion are split in half employing D-shaped mirrors. The resulting halves are then recorded at the monitor inputs of two balanced detectors. In the first approximation, the Rf-output (difference signal of the two monitor inputs) is proportional to the motion orthogonal to the mirror edge. Displacements along the mirror edge are not detected, since their fraction is the same in both input ports [59]. For z-detection, we balance the scattered light field with light sampled directly from the laser [60].

3.2.1 Rotational detection

In a next step, we derive the framework for rotational detection. Therefore, we drop the oscillating term of the scattered field including the phase imprinted with the translational motion, as the rotational motion predominantly influences the light polarization. Hence, also the forward scattered light also

encodes information regarding the orientation. As shown in Figure 3.2, we split the light using a polarizing beam splitter (PBS) at the monitor inputs. Assuming linear polarized light along either along its fast or slow axis, the input power would at the detector would be imbalanced. Thus, we place a half-wave plate before the PBS at an angle $\Theta = \pi/8$ with respect to the scattered light polarization. To account for circularly polarized light we additionally need a quarter-wave plate as it is essential to turn purely imaginary polarized light real [23]. Hence, the retarder angle needs to be adjusted based on the incoming tweezer polarization. Thus, for detecting librations with elliptical polarization the fast axis of the quarter-wave plate should align with the main scattered polarization axis. For circularly polarized light, the quarter-wave plate needs to be rotated by $\pi/4$. We calculate the expected signal at each input port of the balanced detector $s \in \{x, y\}$ as follows

$$I_s = \frac{c\varepsilon_0}{2} E_0^2 k^6 V^2 \left| J_{\mathrm{PBS}}^{s} J_{\mathrm{HWP}}^{\pi/8} J_{\mathrm{QWP}} \begin{pmatrix} \cos(\psi)\chi_{11} + \mathrm{i}\sin(\psi)\chi_{12} + \mathrm{i}\cos(\psi) \\ \cos(\psi)\chi_{21} + \mathrm{i}\sin(\psi)\chi_{22} - \sin(\psi) \\ 0 \end{pmatrix} \right|^2 , \tag{3.5}$$

where J represents the Jones matrices for both retarders. The initial step is to perform the calculation for elliptical polarized light in a deeply trapped regime, excluding rotations. In this instance, we introduce the Jones calculus, representing the light polarization with a Jones vector and optical elements with Jones matrices. The change of the initial polarization through a set of optical elements is described as a multiplication of these Jones matrices. For the quarter-wave plate with the fast axis along the x-axis, the Jones matrix yields

$$J_{\mathrm{QWP}}^{0} = \begin{pmatrix} 1 & 0 \\ 0 & \mathrm{i} \end{pmatrix}. \tag{3.6}$$

The observed signal is the difference between the output of each monitor port. Expanding the susceptibilities, we determine that the detected signal is only linear dependent on α, while all other librations contribute quadratically. This leads to the highest sensitivity for the α-libration around the tweezer axis

$$\Delta I = I_x - I_y = c\varepsilon_0 E_0^2 k^6 V^2 \left(\chi_c - \chi_b\right) \alpha \cos(2\psi) + O(\Omega^2). \tag{3.7}$$

The detection sensitivity scales with the tweezer ellipticity. The maximal sensitivity is observed for linear polarization, while it is absent for circular polarization. Indeed, the scaling is similar to as observed for the frequency (cf. Equation 2.45), indicating that sensitivity and frequency are maximal for linear polarization and vanish for circular polarization. Sticking to the latter case, we calculated a constant driving torque along the tweezer axis (Equation 2.56) leading the particle to rotate. So we adjust the quarter-wave plate by tilting it about 45°

$$J_{\mathrm{QWP}}^{\pi/4} = \frac{1}{2} \begin{pmatrix} 1+\mathrm{i} & 1-\mathrm{i} \\ 1-\mathrm{i} & 1+\mathrm{i} \end{pmatrix}. \tag{3.8}$$

The resulting measured intensity difference yields

$$\Delta I = \frac{c\varepsilon_0 E_0^2 k^6 V^2}{2} \left(\left(\chi_c - \chi_b\right) \cos(2\alpha) + \frac{1}{2} \left(\chi_c^2 - \chi_b^2\right) \sin(2\alpha) \right). \tag{3.9}$$

As expected, the detected signal oscillates with twice the rotation frequency due to the cyclic nature of rotation. Further, the Rf output depends not on α directly, but it changes cosinusoidal with the angle.

3.3 Trapped nanoparticle

We begin by preparing particle samples with spherical particles from microParticles GmbH that exhibit a nominal diameter of $\Phi = (156 \pm 5)$ nm. At nanoparticle concentrations beyond 2 particles/μm^2, particles stick together, forming dumbbells and trimers, as shown in a scanning electron microscope (SEM) image in Figure 3.3.

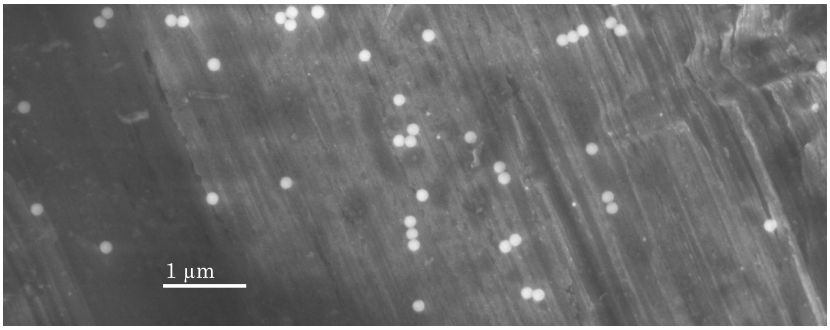

Figure 3.3: Scanning electron microscope image of a used sample coated with spherical nanoparticles, each with a nominal diameter of 156 nm. We observe beside single particles, dumbbells, triangle trimer and chain trimer. The particles are randomly distributed

Once a particle is launched and trapped at 15 mbar, we obtain the motional spectrum with the discussed detection scheme. A combined spectrum of motion is shown in Figure 3.4. The translational PSDs are measured with the split detection scheme, while the α-libration is recorded with the rotational detection setup. The β-libration is recorded from the high frequency part of the x-detection, as the angle deflects the motion along the x-axis. Hence, the libration is partially stored in the phase of the scattered field [23, 55]. The two librations are evidence that a trapped aspherical particle is present, featuring at least two different susceptibilities in the particle frame (Equation 2.45). The oscillation peaks are recorded at 10 mbar with an elliptically polarized tweezer, where every peak is fitted with a Lorentzian shaped function 2.24, allowing the damping and frequency to be free parameters. All motional peaks are well represented by Lorentzian functions, verifying the harmonic trap approximation.
Further, we characterize the trapping potential by calculating the trapping area. From the ratio of the translational frequencies (Equation 2.16) we get the trapping waists with errors estimated small

$$w_x = \frac{\Omega_z}{\Omega_y}\frac{\lambda}{\sqrt{2}\pi} = 1.04\,\mu m, \qquad w_y = \frac{\Omega_z}{\Omega_x}\frac{\lambda}{\sqrt{2}\pi} = 1.1\,\mu m \tag{3.10}$$

for linear polarized light, the minimal and maximal waists we could achieve are $w_x = 0.98\,\mu m$ and $w_y = 1.18\,\mu m$. By utilizing the calculated frequencies and the waist dimensions, we ascertain the power within the trap, thereby completing the tweezer characteristics. The calculated trapping power

$$P = \frac{\Omega_x^2 w_x^3 w_y mc\varepsilon_0 \pi}{4\alpha'} \approx 475\,\mathrm{mW} \tag{3.11}$$

is in good agreement with the measured power before the vacuum chamber of 500 mW. The main loss results from over-illuminating the trapping lens. In order to evaluate the shape of the trapped particle, it

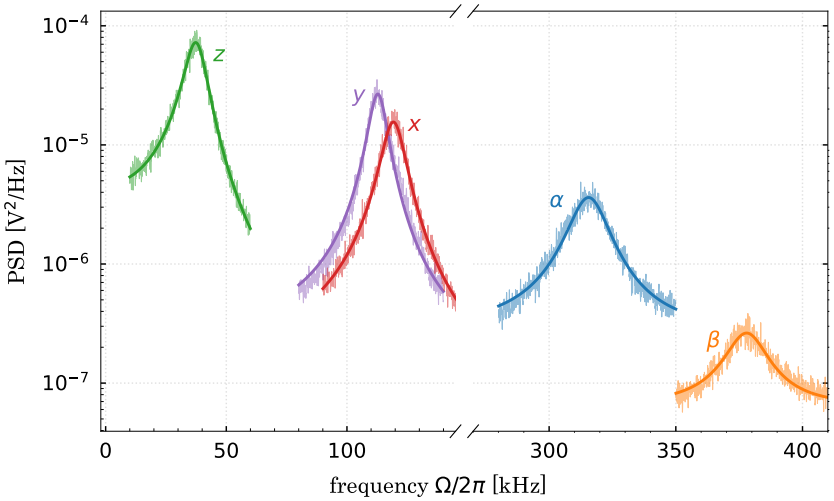

Figure 3.4: Motional spectrum of a trapped nano-dumbbell at $p = 10$ mbar. We observe the three translational peaks in their respective detection, as well as the β-libration in the x-detection. The α-libration is visible in the rotational detection. The trap polarization is elliptical hindering the particle to rotate. The peaks are fitted with a Lorentzian, considering the individual detection noise floors, and leaving the motional damping and frequency as a free parameter. The motional frequencies are $2\pi \times \{38, 113, 120, 315, 378\}$kHz for $\{z, y, x, \alpha, \beta\}$ respectively.

is necessary to calculate the damping ratios, which can be extracted from collisional damping of the nanoparticle by the surrounding gas molecules. These ratios are shape dependent. In the case of a spherical particle, the damping rate in the free molecular regime is given by [61, 62]

$$\Gamma_m = \frac{64}{3} \frac{p}{m\bar{v}_{\text{gas}}} r^2, \tag{3.12}$$

where $\bar{v}_{\text{gas}} = 470$ m/s is the thermal velocity of the nitrogen gas molecules in the chamber and r is the radius. The damping linearly dependence on the pressure p, that lower pressure reduces the damping. However, for aspherical particles this equation must be modified, for example for elliptical shapes r would represent the half of the middle axis of all degrees of freedom [21, 63]. For a proper shape estimation, we need to simulate the gas particles colliding with the nanoparticle. With every collision, the nanoparticle absorbs the total momentum of the impinging gas molecule and afterward the gas molecule is released randomly. Thus, one can calculate the net momentum transfer by the gas molecules, which arises a drag force. This in turn determines the damping of the particle motion. The particle shape is stored in the transfer function describing the collisions between gas molecules and the particle itself. The simulation is implemented as a direct Monte Carlo simulation in [15], where they determine the damping rate ratios for a nano-dumbbell. Since we are only concerned with the damping rate ratios, this method is independent of the pressure and the exact particle size.
From the fitted Lorentzian curves, we obtain the damping ratios for the translational motion $\Gamma_x/\Gamma_y = 1.283 \pm 0.015$, $\Gamma_z/\Gamma_y = 1.245 \pm 0.023$ and $\Gamma_x/\Gamma_z = 1.031 \pm 0.019$. These values are typically for trapped nano-dumbbells. This finding in consistent with the observed particle distribution, which shows a high frequency of dumbbells (Figure 3.3). Further, LIAD is a soft loading technique such that it is likely that particles forming a nano-dumbbell on the sample (Figure 3.3), will remain bonded upon

ablation.
In this case, the trapped nano-dumbbell is not asymmetric in the x-z plane. It should be noted that the damping rates measured are in the laboratory frame. This implies that the x-axis exhibits strongest damping, which corresponds to the particle z-axis with the highest polarizability, as depicted in Figure 3.5a).

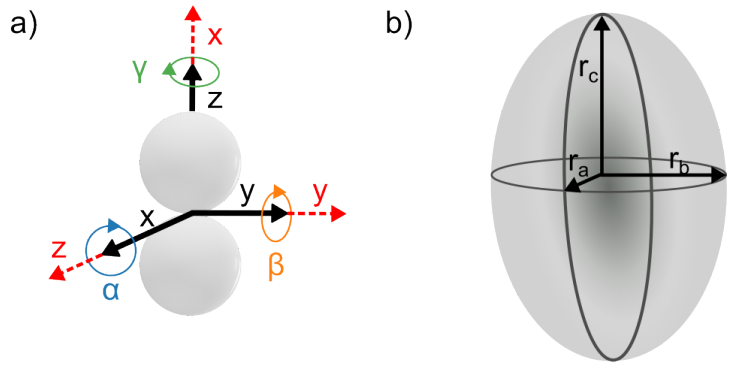

Figure 3.5: a) Sketch of a nano-dumbbell in the particle (black) and in the laboratory/tweezer frame (red), where the tweezer propagates along the z-direction. Both frames are rotated by 90° when the particle is deeply trapped. The Euler angles indicate the librations around their corresponding rotation axis. b) Model of an elliptical particle with the semi-axis r_a, r_b, r_c. This shape serves as a ficitive particle for the trapped anisotropic nano-dumbbells, exhibiting the same optical response.

Among several trapped particles, we have observed slight asymmetries in the plane as well. To precisely measure the damping ratios, we took several time traces at pressures around 10 mbar, ensuring negligible nonlinear effects. Thus, we fit a Lorentzian to each CoM motional peak. The obtained ratios for a particle with three asymmetries is shown in Figure 3.6. For the trapped particle, we assume an overall elliptical

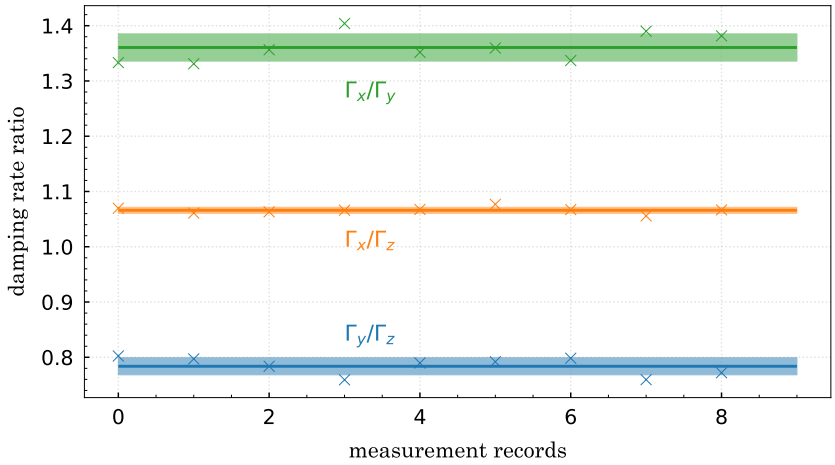

Figure 3.6: Measured damping ratios of one particle at different times. The estimated damping errors are too small to be visible. The shaded area represents the standard deviation to the mean fat lines.

shape. We calculate the median between the measured damping ratios $\Gamma_x/\Gamma_y = 1.361 \pm 0.024$ and $\Gamma_z/\Gamma_y = 1.276 \pm 0.025$, which yields an aspect ratio $a \approx 1.58$ based on a simulation done in [40]. Using the ratio between long and short axis, we optimize the remaining two radii by theoretically calculating the observed translational frequencies. In accordance to Equation 2.51, the translational frequencies are correlated to the electrical susceptibilities, which are defined by [21]

$$\chi_q = \frac{n^2 - 1}{1 + (n^2 - 1)N_q}. \tag{3.13}$$

Here, we introduce the dimensionless depolarization factors N_q, where $q \in \{a, b, c\}$ holds. They are defined by

$$N_q = \frac{r_a r_b r_c}{2} \int_0^\infty \frac{\mathrm{d}s}{\left(s + r_q^2\right)\sqrt{\left(s + r_b^2\right)\left(s + r_y^2\right)\left(s + r_c^2\right)}} \tag{3.14}$$

depending on the particle semi-axis r_a, r_b, r_c as shown in Figure 3.5b). Indeed, the sensitivity of the depolarization factor with respect to the semi-axis is very small and does not affect the particles frequencies to within nanometer precision. Otherwise, the frequencies scale with the particle density. However, in the discussion, we neglect the radiation pressure, which displaces the particle from the center of the trap. This displacement scales linearly with the particle volume

$$z_0 = \frac{V\omega^4 z_R^2 \chi_c}{6\pi c^4}, \tag{3.15}$$

thereby modifying the trapping frequency in accordance with the particle shape. This is exemplified by the z-motion [40]

$$\Omega_z = \frac{\lambda}{\pi w_x w_y}\sqrt{\frac{2P}{c\varepsilon_0 \pi w_x w_y}\frac{z_R^4}{\left(z_0^2 + z_R^2\right)^2}\varepsilon_0 V\left(\chi_c \cos(\psi)^2 + \chi_b \sin(\psi)^2\right)}. \tag{3.16}$$

We simulate the frequencies with the previously determined trapping power and waists for linear polarized light $\psi = 0$. The simulation involves an iterative process, wherein combinations of the two radii are considered and the difference between the determined and measured frequencies is quadratically minimized. The program starts with a range of 100 nm and a step size of 10 nm, then reduces the searching region after each run until a final step size of 0.01 nm is reached. The resulting semi-axis are

$$r_a = (98.8 \pm 0.5)\,\mathrm{nm}, \quad r_b = (100.1 \pm 0.5)\,\mathrm{nm}, \quad r_c = (156 \pm 2)\,\mathrm{nm} \tag{3.17}$$

with the errors arising from the uncertainty in the measured frequency and damping. As expected, the particle exhibits a small asymmetry in the x-z plane, and the assumed elliptical shape matches the long axis we would anticipate for a nano-dumbbell. We took a close up image of a nano-dumbbell in Figure 3.7 and determine its aspect ratio. The nano-dumbbell is fitted with an elliptical shape. The long axis slightly overestimates the shape, while the short axis underestimates the exact shape. Nevertheless, they are in good agreement with the hypothesis that two nominal spheres are sticking together, thereby validating the reconstructed long axis.
The other two axes reconstructed from the damping ratios are too large for a single particle specified by

the nanoparticle supplier, even considering the standard deviation of 5 nm. We ascribe the deviation to the used elliptical model and the fact that we assume the particle anisotropy purely being shape induced. When taking into account the recorded SEM pictures we exclude aspherical shaped particles but the measured anisotropy can also arise from the internal structure. Thus, the particles might exhibit locally regions with a different density, leading to non-isotropic particles. Thus, our determined shape represents a ficitve particle featuring the same optical properties as the trapped one.

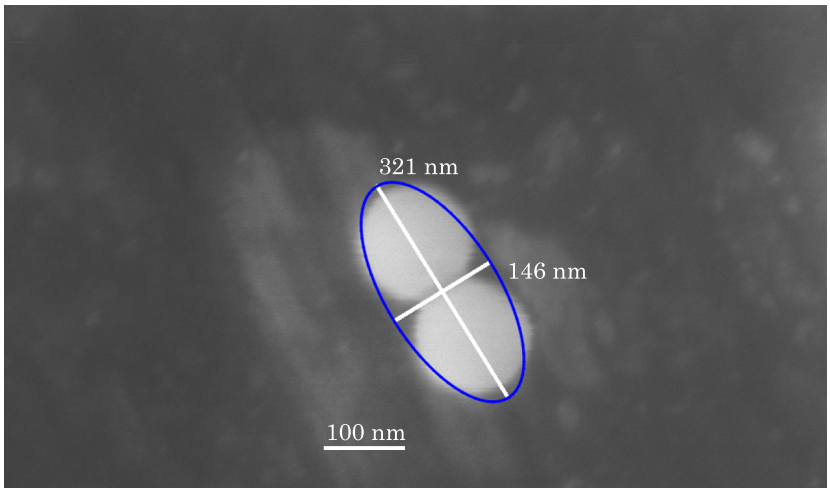

Figure 3.7: Scanning electron microscope image of a nano-dumbbell. The shape is fitted with an elliptic contour to estimate its long and short axis. Based on the fit, the nano-dumbbell is formed by two 156 nm spheres sticking together. The stripes in the image are caused by a high scanning speed.

Another possible explanation is that during the ablation process, a tiny fragment of the silicon coating sticks on top of the nano-dumbbell. Despite that, we would not assume impurities to a large extent or from other materials, as they are likely to absorb the laser light, which in turn leads to an enhanced radiation pressure and trapping as well as keeping the particles stable would be more difficult or even impossible.

3.4 Librations and driven rotations

Although we already indicate in Figure 3.4 that the two observed librations correspond to oscillations around the Euler angles α and β, it is necessary to provide proof of this assertion. Therefore, we measure the behavior of both librations using the aforementioned rotational detection scheme, with the tweezer ellipticity varied in a pressure regime where nonlinearities of the trapping potential were not a concern. We fit the theoretical ellipticity dependencies (Equation 2.45) for α- and β-librations to the data in Figure 3.8. The error estimation of the data results from rotating the tweezer ellipticity by 2π, and thus obtain the frequencies eight times. For circularly polarized light, the frequency fluctuates stronger. This is caused by the $\sqrt{\cos(2\psi)}$ dependency (cf. Equation 2.45) that small ellipticity drifts over time for ψ close to $\pi/4$ cause large frequency shifts. The lack of data points for the β-motion for linearly polarized light is due to the overlap with the α-motion. Minimizing the pressure did not help since nonlinearities and mode splitting occur, changing the expected graph. For ellipticities close to circularly polarized light, the detection sensitivity in the rotation detection scheme is too low. Even in the x- detection, the frequency was not visible. For the rotational detection, a signal linear dependent on β does not exist;

instead, we measure $\alpha^2\beta$. However, the data points are sufficient to prove their characteristic behavior that the observed librations are indeed around α and β. Thus far, our investigation has solely focused on

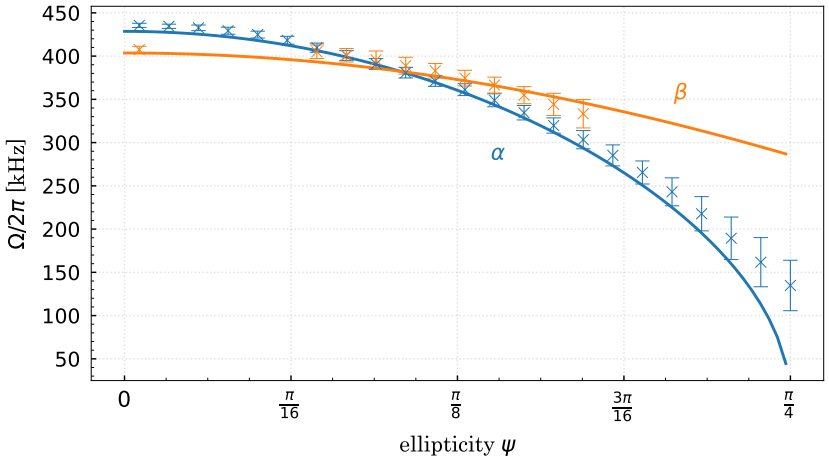

Figure 3.8: Librational frequency of the α- and β-libration in dependence of the tweezer ellipticity. The half- and quarter-waveplate are set such that the x- and y-peak overlap, achieving circular polarization. Then the half-wave plate is rotated in 1° steps for 22.5°, which rotates the ellipticity by twice the angle. The solid lines represent the fits of the theoretical dependency $\Omega_\alpha \propto \sqrt{\cos(2\psi)}$ and $\Omega_\beta \propto \cos(\psi)$.

the ellipticity-frequency dependence, the absolute values of the frequencies have yet to be proven in conjunction with the determined particle shape. As the theoretical frequencies in Equation 2.45 depend additionally on the moment of inertia we define them for an elliptical shape as

$$I_a = \frac{\rho V}{5}(r_b^2 + r_c^2), \qquad I_b = \frac{\rho V}{5}(r_a^2 + r_c^2), \qquad I_c = \frac{\rho V}{5}(r_a^2 + r_b^2). \tag{3.18}$$

We calculate them using the particle geometry from Equation 3.17

$$\begin{aligned} I_a &= (1.024 \pm 0.014) \times 10^{-31}\,\mathrm{kgm}^2, \qquad I_b = (1.016 \pm 0.014) \times 10^{-31}\,\mathrm{kgm}^2, \\ I_c &= (0.589 \pm 0.004) \times 10^{-31}\,\mathrm{kgm}^2. \end{aligned} \tag{3.19}$$

In Figure 3.9 we show the estimated graphs and their errors as the shaded area. The theoretical curves describe the observed librations within their error estimation. Indeed, the α-libration fits the data exactly, proving our shape calculation. In contrast, the β-libration overestimates the measurement. Theoretically, we would not expect that the frequency of the β-libration becomes smaller than the α-frequency. Since, $\chi_a < \chi_b < \chi_c$ and $I_b < I_a$ as well as in the defined interval $\cos(2\psi) < \cos(\psi)^2$ holds, it follows that

$$\frac{\Omega_\beta}{\Omega_\alpha} = \sqrt{\frac{I_a(\chi_c - \chi_a)}{I_b(\chi_c - \chi_b)} \frac{\cos(\psi)^2}{\cos(2\psi)}} > 1, \tag{3.20}$$

Ω_β always exceeds Ω_α. We predict the deviation stemming from the peaks overlapping and thus a bad resolution of the β-libration. Although we are not able to resolve the γ-libration its theoretical graph is shown as well, indicating that the expected frequencies are on the order of the translational ones. In contrast, the β-libration is detectable in linear order when coupled, quadratic to α-, the γ-libration is only detectable quadratically and does not show up in the translational detection.

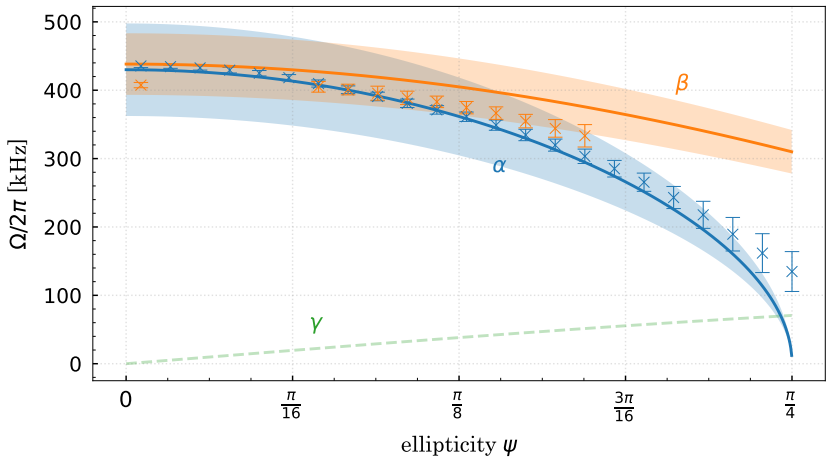

Figure 3.9: Theoretical frequency-ellipticity curve of the three librational frequencies calculated for the measured particle shape $r_a = (98.8 \pm 1.5)$ nm, $r_b = (100.1 \pm 1.5)$ nm and $r_c = (156 \pm 2)$ nm. The shaded area represents the uncertainty with respect to the particle shape determination. The dotted line represents the theoretical prediction for the γ-libration.

3.4.1 Coupling between the librations

We predict that the γ-libration becomes detectable at lower pressure. In the initial stages, the particle undergoes a process of thermalization in velocity through collisions with the surrounding gas, which reduces the motion to a harmonic oscillation. As the damping is reduced, the particle enters a nonlinear trapping regime, leading to non-Lorentzian peaks over the measurement period. We observe this effect for both the translational and rotational modes, with the rotations broadening at $p = 1$ mbar. Finally, as illustrated in Figure 3.10, the rotational peaks experience a splitting phenomenon when the pressure is further reduced ($p = 0.4$ mbar). Each mode then consists of two hybrid modes ω_+ and ω_- appearing as peaks in the spectrum. The splitting occurs from coupling between the α- and β-libration through the remaining γ-rotation, providing a compelling evidence for a diffusive rotating γ-motion [40]. The splitting into two normal modes would not appear if all degrees of freedom are deeply trapped. We further calculate the correlation between the two hybrid modes to be $r = 0.02 \pm 0.01$ at 0.4 mbar, with a consistent decrease starting at $p = 1$ mbar, where we first observe the splitting. For a second particle we determine the correlation at $p = 5 \times 10^{-2}$ mbar to be $r = -0.32 \pm 0.05$. As it is contrary to the trapped motional correlation, we confirm the splitting in two hybrid modes. Consequently, for the purpose of calculation, we revert to the canonical momenta in Equation 2.31 and let γ evolve freely. The Hamilton equations of motion in first order approximation are [40, 53]

$$\ddot{\alpha} + \Omega_\alpha \alpha + \Gamma_\alpha \alpha + \Omega_c \dot{\beta} = \frac{F_{\text{th}}}{I_a} \tag{3.21}$$

$$\ddot{\beta} + \Omega_\beta \beta + \Gamma_\beta \beta - \Omega_c \dot{\alpha} = \frac{F_{\text{th}}}{I_b} \tag{3.22}$$

and exhibit the coupling. The coupling strength $\Omega_c = \omega_\gamma I_c / I_a$ depends on the moment of inertia ratio and the Brownian rotation frequency ω_γ [55]. The γ-motion, even if the polarization is linear, will not be driven optically (Equation 2.57).
We estimate the coupling from fitting the solution of the coupled differential equation of motion. The fitting function does not include the nonlinear effects or second order coupling. However, the

fit is sufficient describing the hybrid modes and their frequency difference, which is proportional to the coupling. As we would expect from both curves the same coupling, we average the couplings $\Omega_c = (27.15 \pm 0.18)\,\mathrm{kHz}$ and determine with the moment of inertia ratio an over 5 s averaged Brownian frequency of $\omega_\gamma = (15.61 \pm 0.26)\,\mathrm{kHz}$. As a remark, the Brownian motion is pressure depend. In

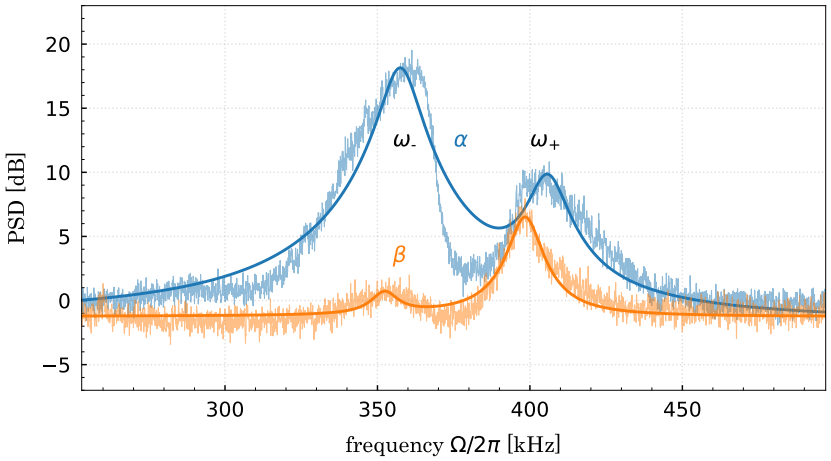

Figure 3.10: Formation of hybrid modes (ω_+, ω_-) in the α- and β-libration at $p = 0.4\,\mathrm{mbar}$ indicating a coupling between α and β through the free or diffusive mode γ. The spectrum for α is recorded in the rotational detection scheme and for β in the x-detection scheme.

analogy to Equation 2.59 the Brownian frequency

$$\omega_\gamma = \frac{\tau_{\mathrm{th}}}{\Gamma_\gamma I_c} \tag{3.23}$$

is inversely proportional to the damping, thus the splitting varies over time. Figure 3.11 illustrates the splitting behavior of a second particle over the measurement period. Here, we observe a negative correlation. As it is visible in the red box, both frequencies move in opposite directions.

3.4.2 Rotation around the tweezer axis

In the pressure regime where we observe the mode splitting $p \approx 0.1\,\mathrm{mbar}$, we also detect a rotation around the tweezer axis when using circularly polarized light. As calculated in Equation 2.56, the restoring torque that aligns the particle long axis with the tweezer polarization axis vanishes. Instead, a constant torque arises from the back action of the scattered light. While the orientation has no steady state solution, the rotation frequency settles. The mean rotational frequency is the ratio of the constant optical torque and the motional damping as shown in Equation 2.59. As a consequence of the fact that the damping is not constant over time due to stochastic gas collisions, the mean rotation frequency fluctuates over time with a mean standard deviation

$$\sigma_\alpha = \sqrt{\frac{k_{\mathrm{B}} T}{I_\alpha}} \tag{3.24}$$

We drive the rotations around the tweezer axis and orientate the quarter and half-wave plate of our detection accordingly. The rotational frequency is measured at twice it frequency, as it scales with $\cos(2\alpha)$. Thus, the PSD does not follow a Lorentzian curve, instead it approaches a delta distribution

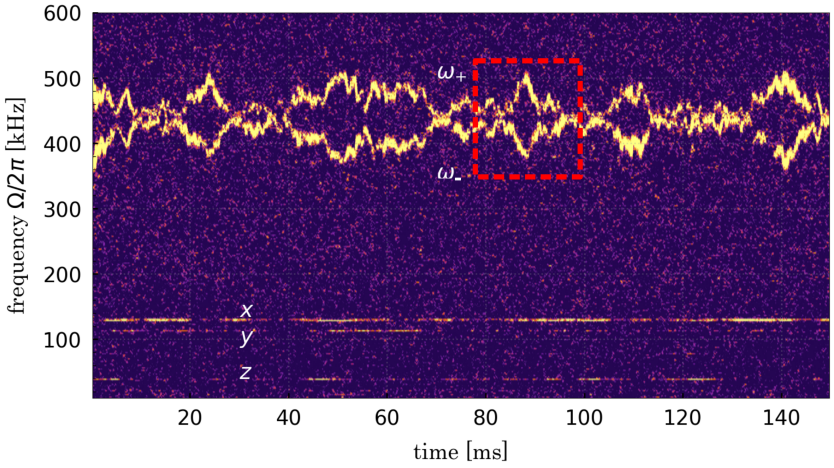

Figure 3.11: Spectrogram of the rotational detection at 5×10^{-2} mbar revealing the behavior of the α libration splitting in ω_+ and ω_- over the time. As the Brownian frequency of the γ libration fluctuates, the mode splitting does it accordingly. The frequencies ω_- and ω_+ are negative correlated, as visualized in the red box, the two modes evolve in opposite directions.

peaked at the mean frequency. For measurement times longer than the damping time, the recorded signal broadens and matches a Gaussian curve with standard deviation σ_α. We measure the rotation around the tweezer axis at 0.16 mbar in Figure 3.12 and fit a Gaussian function. The center frequency is equivalent to twice the actual rotation frequency, which we determine to be $\omega_\alpha = 2\pi \times 1.9$ MHz. From the peak width, we compute I_α under the assumption of no heating or cooling of the rotation, thereby verifying the previously calculated moment of inertia (Equation 3.19). When slicing the time trace in smaller

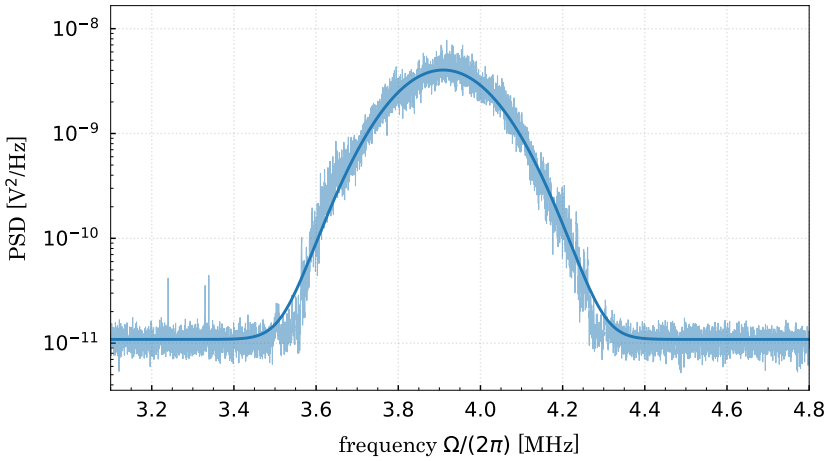

Figure 3.12: PSD of the rotation around the tweezer axis at 0.1 mbar. Since the detection is sensitive to $\cos(2\alpha)$, the spectrum is fitted with a Gaussian function, where its width $\sigma_\alpha = 2\pi(110.47 \pm 0.02)$ kHz corresponds to the moment of inertia $I_a = (1.134 \pm 0.030) \times 10^{-31}$ kgm^2 and the central frequency to twice the actual rotation frequency $\omega_\alpha = 1.9$ MHz.

segments of sufficient duration to resolve the rotation, we observe the graph in Figure 3.13 and the delta peaked traces at four different time steps.

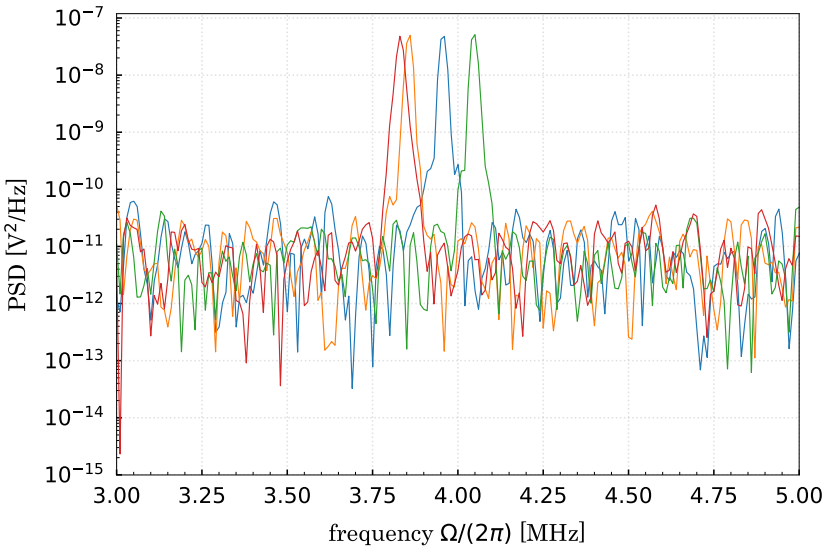

Figure 3.13: PSD of time sliced data at four different times. Each peak approaches a delta peak shape. Their central frequencies change with time, since it is dependent on the current damping.

CHAPTER 4

Coherent scattering cooling

Up to now, we have investigated the rotational dynamics of a trapped asymmetric nanoparticle featuring three distinct electrical susceptibilities. Transferring the particle motion in all six degrees of freedom into the quantum regime, necessitates cooling, such that the mode temperature approaches the ground state energy.
The trapped particle thermalizes with its surrounding environment, which is at room temperature ($T = 300K$). We describe its motion using phonons, and thus following the Bose-Einstein statistics. For each degree of freedom, the mean phonon occupation number is given by

$$n_q = \frac{k_B T}{\hbar \Omega_q}, \tag{4.1}$$

which inversely scales with the corresponding frequency Ω_q. For the trapped nanoparticles, we anticipate occupation numbers in the range of $n_q = 10^7 - 10^8$. Consequently, the motion can be treated classically and must be cooled in order to exhibit quantum mechanical behavior. We employ laser cooling techniques to reduce the motional temperature.
A light beam in thermal equilibrium has a mean thermal photon occupation of $n = 3.2 \times 10^{-10}$, which is significantly below $n = 1$. This indicates that the light field is effectively in its ground state at room temperature and can therefore serve as a cold bath for the harmonic oscillator. By coupling the nanoparticle motion to the light field, cooling can be achieved [52].

4.1 Cooling techniques

Generally, several techniques exist to cool the motion of a levitated nanosphere. One approach involves adjusting the trapping potential based on the nanoparticle position. This method works analogous to the manner by which a child acquires kinetic energy while on a swing. The trapping stiffness is actively increased as the particle moves away from the trapping center and is subsequently decreased as it falls back. When the trapping laser itself is modulated, this method is known as parametric feedback cooling [23, 59]. Since the laser power controls the trap stiffness (Equation 2.9), modulating it at twice the frequency restricts the particle motion. Thus, it is essential to monitor its position continuously, subsequently calculate a suitable feedback and apply it to the laser. However, the feedback signal will inevitably be subject to detection and electronic noise, which will render ground state cooling a challenging endeavor. Despite this, cooling of the three librational motion to below 16 mK has been demonstrated using this technique [25].

Similarly, an electric feedback applied via electrodes can counteract the particle motion, making this technique suitable for charged nanoparticles exclusively [27]. In combination with a Kalman filtering state estimation and a detection efficiency approaching the Heisenberg limit, one-dimensional translational ground state cooling has been achieved [29].
When theoretically calculating the impact of feedback cooling, all techniques have in common the induction of an additional friction force F_{fb}

$$F_{\mathrm{fb}} = -m_q \Gamma_q g \dot{q}, \tag{4.2}$$

which depends on the dimensionless gain g and the oscillator velocity. According to Equation 2.19 this results in a modified equation of motion

$$\ddot{q} + \Gamma_q \dot{q} + \Omega_q^2 q = \frac{F_{\mathrm{th}} + F_{\mathrm{fb}}}{m_q}. \tag{4.3}$$

The feedback force adds to the thermal damping, enhancing it by the gain factor. Consequently, the PSD, as derived in Equation 2.24, is calculated with a total damping $\Gamma_{\mathrm{tot}} = \Gamma_q(1+g)$. Integrating the PSD over the entire frequency range yields the motional variance, which is proportional to the mode temperature

$$\langle q(\omega)^2 \rangle = \frac{1}{2\pi} \int_{-\infty}^{\infty} S_{qq}(\omega) \mathrm{d}\omega = \frac{k_B T}{m \Omega_q^2} \frac{\Gamma_q}{\Gamma_{\mathrm{tot}}}. \tag{4.4}$$

Thus, the ratio of the variance of motion with and without applied feedback leads to an effective mode temperature

$$T_{\mathrm{eff}} = \frac{T}{1+g}, \tag{4.5}$$

which decreases as the gain increases.
In practice, we record a time trace of a thermalized nanoparticle at approximately 10 mbar and state its temperature as $T = 300\,\mathrm{K}$. We extract the spectral density by integrating over the frequencies where the motional peak rises is above the noise floor. The same analysis is then performed for a cooled particle, allowing us to estimate the motional temperature by comparing the spectral areas.

4.2 Coherent scattering cooling

In contrast to active feedback control, coherent scattering cooling is a passive cooling method, which eliminates the need for continuous particle position monitoring and relaxes the requirement for a quantum limited detection. Originally developed for atomic cooling [33], this technique has been adapted for nanoparticles. The oscillator is placed inside an empty optical cavity and scatters tweezer light, which in turn drives the cavity. Instead of coupling the particle motion to the intensity of a light field, it is coupled to the electrical field of the cavity.
The interaction between the incoming light field and the mechanical oscillator can be described by quantizing the light field as well as the mechanical motion. Photons scatter both elastically and inelastically with the phonons. The elastic scattering process, known as Rayleigh scattering, dominates the interaction [32]. In the inelastic scattering process, known as Raman scattering, photons exchange

energy with the phonons, leading to either an increase or decrease in the particle energy

$$\Delta\hbar\Omega = \hbar\omega - \hbar\omega_s, \tag{4.6}$$

where ω_s is the frequency of the scattered photons [64]. The energy difference $\Delta\hbar\Omega$ between the incoming and the scattered photon is absorbed by the phonon. In the event that the scattered photon energy is less than before, the phonon absorbs a positive energy difference. This difference increases the motional temperature, referred to as Stokes scattering.
Conversely, if the scattered photon has a higher energy than before, the phonon will be absorbed, called Anti-Stokes scattering. Anti-Stokes scattered light is enhanced in the optical cavity by blue-detuning its resonance with respect to the tweezer. This effect is similar to the Purcell enhancement [33, 65], where the density of states inside the cavity is increased at the frequency of Anti-Stokes scattering. The probability of populating the cavity with Anti-Stokes scattered light is, according to Fermi's golden rule, thus favorable than for Stokes scattered photons. This leads to a reduction of the motional energy. This technique has successfully demonstrated translational ground state cooling in one [36] and two dimensions [37, 38], and recently, also cooling of six degrees of freedom below 10 mK [40].

4.3 Light-Particle interaction

The framework of coherent scattering cooling relies on the coupling between the optical fields (both tweezer and cavity fields) and the nanoparticle motion. Since the tweeer is tightly focused, we expect an enhanced coupling effect [66].
We mathematically describe the motion in relation to the light fields using Hamiltonian mechanics. To achieve this, we extend Equation 2.9 including the tweezer field $\mathbf{E}_t$ with the cavity field $\mathbf{E}_c$ and express the interaction Hamiltonian in the form

$$H_{\text{int}} = \frac{1}{4}\varepsilon_0 V \left(\mathbf{E}_c + \mathbf{E}_t\right)^* \chi \left(\mathbf{E}_c + \mathbf{E}_t\right). \tag{4.7}$$

This Hamiltonian can be decomposed into three parts, consisting of the tweezer-tweezer interaction H_{TT}, which describes the trapping potential for the particle, the nanoparticle-cavity interaction described by the cavity-cavity interaction H_{CC} and the tweezer-cavity coupling H_{TC}. In the interaction term, we omit the free field contribution. The coupling between the free field and the cavity field provide an additional decay channel for the intracavity field. Additionally, the free field-tweezer interaction lead to recoil heating [67]. Thus, the total decomposed Hamiltonian is

$$H = H_N + H_C + H_{\text{int}} = H_N + H_C + H_{TT} + H_{CC} + H_{TC}, \tag{4.8}$$

where H_N denotes the Hamiltonian for the free particle and H_C represents the Hamiltonian of the cavity field.

4.3.1 Particle Hamiltonian

In Chapter 2, we derived that the librational and translational motions are approximately harmonic oscillations around the particle equilibrium position $\mathbf{r} = (0, 0, 0)$ and orientation $\Omega = (0, \pi/2, 0)$. Consequently, the particle Hamiltonian including the free evolution, as presented in Equation 2.35, and

the optical potential induced by the tweezer, takes the form

$$H = H_N + H_{TT} = \frac{p_q^2}{2m_q} + \frac{1}{2} m_q \Omega_q^2 q^2, \tag{4.9}$$

with the index $q \in \{x, y, z, \alpha, \beta, \gamma\}$. As discussed qualitatively in Section 4.2, the harmonic motion refers to quantized phonons. We can therefore rewrite the Hamiltonian by introducing the ladder operators $\hat{b}_q$ and $\hat{b}_q^\dagger$, which represent the annihilation and creation of a phonon in mode q and are related to the particle position and momentum by

$$q = q_{\mathrm{zpf}} \left(\hat{b}_q^\dagger + \hat{b}_q \right), \qquad p_q = \mathrm{i} q_{\mathrm{zpf}} m_q \Omega_q \left(\hat{b}_q^\dagger - \hat{b}_q \right). \tag{4.10}$$

Here, we introduce the zero-point fluctuation of motion, which is defined by

$$q_{\mathrm{zpf}} = \sqrt{\frac{\hbar}{2 m_q \Omega_q}}, \tag{4.11}$$

describing the minimal extent to which the particle is localized. In the ground state, the motional variance is on the order of the zero-point fluctuation. When inserting the moments of inertia, we obtain the zero-point fluctuation for the librational motion. For the particles we typically trap, the zero-point fluctuations for the librational and translational modes are on the order of

$$x_{\mathrm{zpf}} \approx 2\,\mathrm{pm}, \qquad \alpha_{\mathrm{zpf}} \approx 14\,\mu\mathrm{rad}. \tag{4.12}$$

The librational zero-point fluctuation describes the minimal angle to which we can determine the particle orientation. We continue calculating the quantized particle Hamiltonian for the coherent scattering cooling description as

$$H = \hbar \sum_q \Omega_q \hat{b}_q^\dagger \hat{b}_q, \tag{4.13}$$

where we omit the constant zero-point energy as we are only interested in the dynamics of the system.

4.3.2 Cavity field and nanoparticle coupling

The optical cavity is described as a Fabry-Perot interferometer, where a standing wave is formed between two mirrors facing each other. The electric field inside the cavity can be quantized by a superposition of two electric fields counter-propagating [68, 69]

$$\mathbf{E}_c = \mathbf{E}_+ + \mathbf{E}_- \tag{4.14}$$

where, $\mathbf{E}_+$ and $\mathbf{E}_-$ represent the left and right propagating electric fields, respectively

$$\mathbf{E}_+ = \sum_s \sqrt{\frac{\hbar \omega_c}{2 \varepsilon_0 V_c}} f_c^*(\mathbf{r}) \mathbf{e}_s^* \mathrm{e}^{-\mathrm{i}\omega_c t} \hat{c}_s^\dagger, \tag{4.15}$$

$$\mathbf{E}_- = \sum_s \sqrt{\frac{\hbar \omega_c}{2 \varepsilon_0 V_c}} f_c(\mathbf{r}) \mathbf{e}_s \mathrm{e}^{\mathrm{i}\omega_c t} \hat{c}_s. \tag{4.16}$$

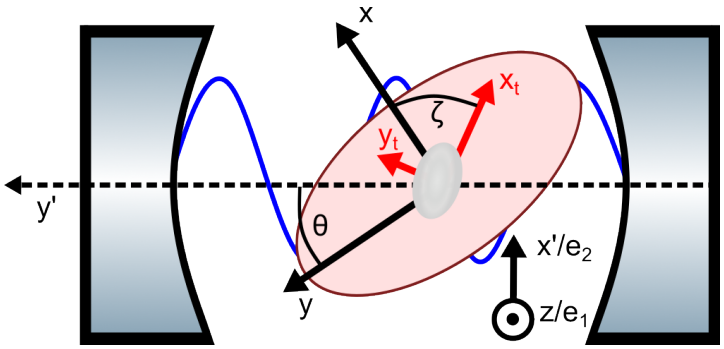

Figure 4.1: Drawing of the orientational relation between the tweezer and the cavity. The solid black coordinate system represents the reference frame in which the particle motion and the tweezer intensity axes are defined. The cavity frame (dotted black) is rotated by an angle θ with respect to the reference frame. The tweezer polarization axes (red), defining the particle orientation, are rotated by the angle ζ with respect to the reference frame. Consequently, the angle $\tilde{\theta} = \theta - \zeta$ describes the polarization orientation between the tweezer and the cavity frame.

Here, the ladder operators $\hat{c}_s$ and $\hat{c}_s^\dagger$ describe the photon annihilation and creation in polarization mode s. We concern two polarization modes, indexed with $s \in \{1, 2\}$. Furthermore, we introduce $f_c(\mathbf{r})$ as the mode function of the cavity and V_c representing the cavity volume.
The Hamiltonian for the cavity field is determined by inserting the cavity field into the expression

$$H_C = \frac{\varepsilon_0}{2} \int \mathrm{d}^3\mathbf{r} \left(\mathbf{E}_c^2 + c^2 \mathbf{B}_c^2 \right). \tag{4.17}$$

This results in the cavity field Hamiltonian describing a harmonic oscillator for each polarization mode

$$H_C = \hbar \sum_s \omega_c \hat{c}_s^\dagger \hat{c}_s, \tag{4.18}$$

where we again neglect the constant terms resulting from the vacuum fluctuations. The intracavity electric field is characterized by the mode function, which describes a standing wave along the cavity axis with a transversal Gaussian profile

$$f_c(\mathbf{r}) = \frac{w_c}{w_c(x')} \exp\left(\frac{-(x'^2 + z^2)}{w(x')^2} \right) \cos(ky' - \phi), \tag{4.19}$$

where w_c is the cavity waist. As illustrated in Figure 4.1, the cavity is placed orthogonal to the tweezer. We introduce the angle θ, which represents the tilt between the radial cavity axis y' and the y-axis of the tweezer coordinate system. When assuming the overlap of the tweezer coordinate system (black) with the tweezer polarization coordinate system (red), the angle θ determines the orientation of the tweezer polarization with respect to the cavity axis. The cavity coordinates in terms of the reference coordinate system are

$$x' = \cos(\theta)x - \sin(\theta)y \tag{4.20}$$
$$y' = \sin(\theta)x + \cos(\theta)y. \tag{4.21}$$

Since the cavity is not translationally displaced with respect to the tweezer, the particle trapping position $\mathbf{r} = (0, 0, 0)$ remains the same in the cavity frame. Hence, the particle position depends on the phase ϕ of the standing wave. According to mode profile in Equation 4.19, if $\phi = 0$ the particle is placed at the anti-node; if $\phi = \pi/2$ the particle is positioned at the node.
Subsequently, we continue calculating the cavity-cavity interaction term

$$H_{CC} = -\frac{1}{4}\varepsilon_0 V \mathbf{E}_c^* \chi \mathbf{E}_c, \tag{4.22}$$

which leads to the expression

$$H_{CC} = -\frac{1}{4}\varepsilon_0 V \frac{\hbar\omega_c}{2\varepsilon_0 V_c} |f_c(\mathbf{r})|^2 \sum_{s,s'} \left((\hat{c}_{s'}^\dagger \mathrm{e}^{-\mathrm{i}\omega_c t} \mathbf{e}_{s'}^* + \hat{c}_{s'} \mathrm{e}^{\mathrm{i}\omega_c t} \mathbf{e}_{s'}) \chi (\hat{c}_s^\dagger \mathrm{e}^{-\mathrm{i}\omega_c t} \mathbf{e}_s^* + \hat{c}_s \mathrm{e}^{\mathrm{i}\omega_c t} \mathbf{e}_s) \right), \tag{4.23}$$

when inserting the electric field. We neglect the cavity birefringence, so both polarization modes oscillate with the same frequency ω_c. We apply the rotating wave approximation (RWA) and thereby omit the terms rotating with twice the cavity frequency, because their oscillation is too fast for the system dynamics. This results in a simplified expression for the cavity-cavity Hamiltonian

$$H_{CC} = -\hbar\omega_c \frac{V}{8V_c} |f_c(\mathbf{r})|^2 \sum_{s,s'} \left((\mathbf{e}_{s'}^* \chi \mathbf{e}_s) \hat{c}_{s'}^\dagger \hat{c}_s + (\mathbf{e}_{s'} \chi \mathbf{e}_s^*) \hat{c}_{s'} \hat{c}_s^\dagger \right). \tag{4.24}$$

Indeed, the motional dependence is stored in the mode function 4.19. By expanding it in a Taylor series up to the linear order around the equilibrium position, the result

$$|f_c(x, y, z)|^2 \approx \cos(\phi)^2 + k y' \sin(2\phi) + O(q^2) \tag{4.25}$$

is linearly dependent on the x- and y-position, but not on the z-position. Consequently, we anticipate that the motion orthogonal to the tweezer propagation exhibits linear coupling, while the z-motion does not.
Next, we calculate the susceptibility with respect to the cavity polarization. Therefore, we extract the orientation of the cavity polarization modes from the angle dependencies as depicted in Figure 4.1.
In this configuration, we introduce an angle ζ between the tweezer polarization (red) and the tweezer intensity axes (black). We describe in the reference x-y-coordinate system the tweezer elliptical shape incorporating its waists (w_x, w_y) and the motion along the respective axes. The cavity, however, operates in its own x'-y'-coordinate system (black dashed), which is rotated by the angle θ relative to the reference frame. Thus, the angle between tweezer polarization and cavity axis is $\tilde{\theta} = \theta - \zeta$.
Instead of rewriting the tweezer polarization, we express the cavity polarization vectors in terms of the tweezer polarization. In fact the cavity polarization modes are orthogonal to its axis y', one mode is polarized along the tweezer propagation axis

$$\mathbf{e}_1 = \mathbf{e}_z. \tag{4.26}$$

The second mode polarized in the plane orthogonal to $\mathbf{e}_1$ is

$$\mathbf{e}_2 = \cos(\tilde{\theta})\mathbf{e}_{tx} + \sin(\tilde{\theta})\mathbf{e}_{ty}, \tag{4.27}$$

where $\mathbf{e}_{tx}$ and $\mathbf{e}_{ty}$ represent the basis of the tweezer polarization frame. In the case, $\theta = \zeta$ the cavity mode $\mathbf{e}_2$ is polarized along the tweezer x-polarization axis.
Since the cavity polarization modes are real, the susceptibility tensor is symmetric and $\chi \in \mathbb{R}$ holds, the

Hamiltonian can be written in the form

$$H_{CC} = -\hbar\omega_c \frac{V}{4V_c} |f_c(\mathbf{r})|^2 \sum_{s,s'} (\mathbf{e}_s \chi \mathbf{e}_{s'}) \left(\hat{c}_s^\dagger \hat{c}_{s'} + \frac{1}{2}\delta_{ss'} \right), \tag{4.28}$$

where the constant term results from the commutator relation $[\hat{c}_{s'}, \hat{c}_s^\dagger] = \delta_{ss'}$. We continue by inserting the mode function approximation for small displacements along the x- and y-axis up to linear order. Accordingly, we split the Hamiltonian in two parts containing a constant and a particle dependent term

$$H_{CC}^{(1)} = -\hbar\omega_c \frac{V}{4V_c} \cos(\phi)^2 \sum_{s,s'} (\mathbf{e}_s \chi \mathbf{e}_{s'}) \left(\hat{c}_s^\dagger \hat{c}_{s'} + \frac{1}{2}\delta_{ss'} \right), \tag{4.29}$$

$$H_{CC}^{(2)} = -\hbar\omega_c \frac{V}{4V_c} k \sin(2\phi)(x \sin(\theta) + y \cos(\theta)) \sum_{s,s'} (\mathbf{e}_s \chi \mathbf{e}_{s'}) \left(\hat{c}_s^\dagger \hat{c}_{s'} + \frac{1}{2}\delta_{ss'} \right). \tag{4.30}$$

Although the first term does not include a motional coupling, the presence of the particle at phase ϕ of the standing wave shifts the cavity frequency. Indeed, the particle induces a change in the refractive index locally, and thus alters the path length for the standing light wave. This results in a cavity frequency

$$\omega_{cs} = \omega_c \left(1 - \frac{V}{4V_c} \cos(\phi)^2 (\mathbf{e}_s \chi \mathbf{e}_s) \right), \tag{4.31}$$

which depends on the particle orientation with respect to the polarization mode. As a result, the assumed degeneracy of the two cavity modes is lifted by the particle. We stress that just the presence of the particle is responsible for this shift. Therefore, we obtain the particle susceptibility in terms of the cavity polarization modes around the equilibrium orientation

$$\mathbf{e}_1 \chi \mathbf{e}_1(0, \pi/2, 0) = \chi_a, \tag{4.32}$$

$$\mathbf{e}_2 \chi \mathbf{e}_2(0, \pi/2, 0) = \cos(\tilde{\theta})^2 \chi_c + \sin(\tilde{\theta})^2 \chi_b, \tag{4.33}$$

$$\mathbf{e}_{1/2} \chi \mathbf{e}_{2/1}(0, \pi/2, 0) = 0, \tag{4.34}$$

where we notice that the cross coupling between the two modes vanishes.
Consequently, the shifted cavity frequencies for the two modes

$$\omega_{c1} = \omega_c \left(1 - \frac{V}{4V_c} \chi_a \right) \tag{4.35}$$

$$\omega_{c2} = \omega_c \left(1 - \frac{V}{4V_c} \left(\cos(\tilde{\theta})^2 \chi_c + \sin(\tilde{\theta})^2 \chi_b \right) \right), \tag{4.36}$$

reveal cavity birefringence based on the orientation dependent susceptibilities. The second Hamiltonian captures the linear coupling between the particle motion and the cavity field. The particle position is expressed using the ladder operators (cf. Equation 4.10), resulting in

$$H_{CC}^{(2)} = -\hbar(g_{sx}(\hat{b}_x^\dagger + \hat{b}_x) + g_{sy}(\hat{b}_y^\dagger + \hat{b}_y)) \left(\hat{c}_s^\dagger \hat{c}_s + \frac{1}{2} \right), \tag{4.37}$$

where g_{sx} and g_{sy} represent the coupling constants for motion along x- and y-motion

$$g_{sx} = \sum_s (\mathbf{e}_s \chi \mathbf{e}_s) \frac{\omega_c V}{4V_c} k \sin(2\phi) \sin(\theta) x_{\text{zpf}}, \qquad g_{sy} = \sum_s (\mathbf{e}_s \chi \mathbf{e}_s) \frac{\omega_c V}{4V_c} k \sin(2\phi) \cos(\theta) y_{\text{zpf}}. \quad (4.38)$$

Here, we include the zero-point fluctuation to obtain a coupling constant frequency, which is better comparable to the motional frequencies.
The coupling strength scales with the ratio between the particle size and the cavity mode volume, such that the coupling is stronger for a bigger particle. Further, the coupling is maximized along the standing wave at $\phi = \pi/4$, while it is minimal at the node and anti-node. Moreover, we can not insert the determined particle orientation in Equation 4.32, since the cavity mode(s) to which each motion couple(s) is unknown. Consequently, an evaluation of the tweezer-cavity interaction is necessary.

4.3.3 Tweezer-cavity interaction

The tweezer-cavity coupling is responsible for coherent scattering cooling [35]. The corresponding Hamiltonian, describes the interaction between the particle motion inside the tweezer and the cavity electric field. We determine from Equation 4.7 the tweezer-cavity Hamiltonian

$$H_{TC} = -\frac{1}{4} \varepsilon_0 V \mathbf{E}_t^* \chi \mathbf{E}_c + \text{H.c.} \quad (4.39)$$

and insert the electric fields for both the tweezer and the cavity (Equation 4.14) considering the two cavity modes. Thus, the inner product of the two fields with respect to the particle susceptibility yields

$$\mathbf{E}_t^* \chi \mathbf{E}_c \propto (E_0 \mathrm{e}^{i\omega t} \mathbf{e}_t + E_0^* \mathrm{e}^{-\mathrm{i}\omega t} \mathbf{e}_t^*) \chi (E_c \hat{c}_s \mathrm{e}^{\mathrm{i}\omega_c t} \mathbf{e}_s + E_c^* \hat{c}_s^\dagger \mathrm{e}^{-\mathrm{i}\omega_c t} \mathbf{e}_s^*), \quad (4.40)$$

where we summarize the terms using the RWA

$$\mathbf{E}_t^* \chi \mathbf{E}_c \propto E_0^* E_c \hat{c}_s \mathrm{e}^{\mathrm{i}\Delta t} \mathbf{e}_t^* \chi \mathbf{e}_s + E_0 E_c^* \hat{c}_s^\dagger \mathrm{e}^{-\mathrm{i}\Delta t} \mathbf{e}_t \chi \mathbf{e}_s^*, \quad (4.41)$$

where we keep only oscillating terms with $\Delta = \omega_c - \omega$. The remaining terms describe the process, where a cavity photon is created, while a tweezer photon is annihilated and the other way around. Thus, these terms describe the energy transfer between the tweezer and the cavity via the particle. The frequency difference between the cavity and the tweezer frequency Δ is known as the detuning. To simplify the analysis, we substitute the oscillating terms in the cavity mode operators with the detuning, as follows

$$\hat{c}_s \exp(\mathrm{i}\Delta t) \rightarrow \hat{c}_s. \quad (4.42)$$

Given that the mode functions for both the tweezer and the cavity are real ($f_{t,c}^*(\mathbf{r}) = f_{t,c}(\mathbf{r})$) and $\mathbf{E}_c$ comprises solely Hermitian operators, the interaction Hamiltonian reduces to the form

$$H_{TC} = -\frac{1}{2} \varepsilon_0 V \sqrt{\frac{4P}{c\varepsilon_0 \pi w_x w_y}} f_t(\mathbf{r}) \sqrt{\frac{\hbar\omega_c}{2\varepsilon_0 V_c}} f_c(\mathbf{r}) \sum_s \left(\mathbf{e}_t^* \chi \mathbf{e}_s \hat{c}_s + \text{H.c.} \right). \quad (4.43)$$

The coupling to the translational modes is imprinted in the mode functions, while for the librations it is included in the inner product of tweezer and cavity polarization. To derive the translational coupling we

therefore expand both mode functions to their linear dependence in $q \in \{x, y, z\}$

$$f_t(\mathbf{r}) \approx 1 + \mathrm{i}\left(k - \frac{1}{z_r}\right) z + O(q^2), \tag{4.44}$$

$$f_c(\mathbf{r}) \approx \cos(\phi) + \sin(\phi) k \left(x \sin(\theta) + y \cos(\theta)\right) + O(q^2). \tag{4.45}$$

By inserting these approximations back into the Hamiltonian, we obtain

$$\begin{aligned} H_{TC} \approx -\hbar \sqrt{\frac{PV^2\omega_c}{2\hbar c \pi w_x w_y V_c}} \left(\cos(\phi) + \mathrm{i}\cos(\phi)\left(k - \frac{1}{z_r}\right) z + \sin(\phi) k \left(x \sin(\theta) + y \cos(\theta)\right)\right) \\ \times \left(\mathbf{e}_t^* \chi \mathbf{e}_1 \hat{c}_1 + \mathbf{e}_t^* \chi \mathbf{e}_2 \hat{c}_2 + \mathrm{H.c.}\right). \end{aligned} \tag{4.46}$$

The inner product $\mathbf{e}_t^* \chi \mathbf{e}_s$ imprints the information how the tweezer couple to the cavity mode through the particle. In the same manner we developed the cavity-cavity coupling constants, we evaluate the term for both cavity modes

$$\mathbf{e}_t^* \chi \mathbf{e}_1 = \cos(\psi)\chi_{13} - \mathrm{i}\sin(\psi)\chi_{23} \tag{4.47}$$

$$\mathbf{e}_t^* \chi \mathbf{e}_2 = \cos(\psi)(\chi_{11}\cos(\tilde{\theta}) + \chi_{12}\sin(\tilde{\theta})) - \mathrm{i}\sin(\psi)(\chi_{21}\cos(\tilde{\theta}) + \chi_{22}\sin(\tilde{\theta})). \tag{4.48}$$

In order we are interested in the translational motion we insert the equilibrium orientation and determine

$$\mathbf{e}_t^* \chi \mathbf{e}_1(0, \pi/2, 0) = 0, \tag{4.49}$$

$$\mathbf{e}_t^* \chi \mathbf{e}_2(0, \pi/2, 0) = \cos(\tilde{\theta})\cos(\psi)\chi_c - \mathrm{i}\sin(\tilde{\theta})\sin(\psi)\chi_b, \tag{4.50}$$

which indicates that only $\hat{c}_2$ couples to the translational motion. In analogy, we summarize the terms in coupling constants G_{sq}, where the translational ones read

$$G_{2x} = \sqrt{\frac{PV^2\omega_c}{2\hbar c \pi w_x w_y V_c}} \sin(\phi) k \sin(\theta) \left(\cos(\tilde{\theta})\cos(\psi)\chi_c - \mathrm{i}\sin(\tilde{\theta})\sin(\psi)\chi_b\right) x_{\mathrm{zpf}}, \tag{4.51}$$

$$G_{2y} = \sqrt{\frac{PV^2\omega_c}{2\hbar c \pi w_x w_y V_c}} \sin(\phi) k \cos(\theta) \left(\cos(\tilde{\theta})\cos(\psi)\chi_c - \mathrm{i}\sin(\tilde{\theta})\sin(\psi)\chi_b\right) y_{\mathrm{zpf}}, \tag{4.52}$$

$$G_{2z} = \sqrt{\frac{PV^2\omega_c}{2\hbar c \pi w_x w_y V_c}} \mathrm{i}\cos(\phi)\left(k - \frac{1}{z_r}\right) \left(\cos(\tilde{\theta})\cos(\psi)\chi_c - \mathrm{i}\sin(\tilde{\theta})\sin(\psi)\chi_b\right) z_{\mathrm{zpf}}. \tag{4.53}$$

Since the translational motion couples to $\hat{c}_2$ solely the cavity-cavity coupling constants 4.30 are

$$g_{2x} = \frac{\omega_c V}{4V_c} k \sin(2\phi) \sin(\theta) \left(\cos(\tilde{\theta})^2 \chi_c + \sin(\tilde{\theta})^2 \chi_b\right) x_{\mathrm{zpf}}, \tag{4.54}$$

$$g_{2y} = \frac{\omega_c V}{4V_c} k \sin(2\phi) \cos(\theta) \left(\cos(\tilde{\theta})^2 \chi_c + \sin(\tilde{\theta})^2 \chi_b\right) y_{\mathrm{zpf}}. \tag{4.55}$$

Consequently, the coupling strengths G and g exhibit similar orientational dependence. As illustrated in Figure 4.1, the strongest coupling occurs when the tweezer axis aligns with the cavity axis and the polarization is orientated orthogonal to both. For the x-motion, this corresponds to $\theta = \zeta = \pi/2$, while for the y-motion, it corresponds to $\theta = \zeta = 0$.

In difference to the cavity-cavity coupling, the tweezer-cavity interaction maximizes for the x- and y-motion at the node, whereas the z-motion achieves its maximum coupling at the anti-node.
Beside the particle orientation, these couplings scale differently, while the cavity-cavity interaction is determined only by the particle and cavity properties, the tweezer-cavity coupling can be controlled by regulating the optical power.
Finally, we complete the interaction analysis by calculating the librational coupling constants. Therefore, we evaluate the inner product to the linear order in each angle and determine that α also couples exclusively to $s = 2$, whereas the β- and γ-libration couple only to the $s = 1$ cavity mode e.g.

$$\mathbf{e}_t^* \chi \mathbf{e}_1(0, \beta; \pi/2, 0) \approx \cos(\psi)(\chi_c - \chi_a)\beta \tag{4.56}$$

$$\mathbf{e}_t^* \chi \mathbf{e}_2(0, \beta; \pi/2, 0) = 0 \tag{4.57}$$

Thus, the librational coupling constants are given by

$$G_{2\alpha} = \sqrt{\frac{PV^2\omega_c}{2\hbar c\pi w_x w_y V_c}} \cos(\phi)\left(\chi_c - \chi_b\right)\left(\cos(\psi)\sin(\tilde{\theta}) - \mathrm{i}\sin(\psi)\cos(\tilde{\theta})\right)\alpha_{\mathrm{zpf}}, \tag{4.58}$$

$$G_{1\beta} = \sqrt{\frac{PV^2\omega_c}{2\hbar c\pi w_x w_y V_c}} \cos(\phi)\left(\chi_c - \chi_a\right)\cos(\psi)\beta_{\mathrm{zpf}}, \tag{4.59}$$

$$G_{1\gamma} = \sqrt{\frac{PV^2\omega_c}{2\hbar c\pi w_x w_y V_c}} \cos(\phi)\mathrm{i}\left(\chi_b - \chi_a\right)\sin(\psi)\gamma_{\mathrm{zpf}} \tag{4.60}$$

and are maximal at the anti-node. Further, their coupling scales similarly to their respective frequency (cf. Equation 2.45). With linearly polarized light, the γ-libration transitions into diffusive rotational motion, to which the cavity can not interact, since the coupling is zero. Rotating the tweezer ellipticity to circularly polarized light, the α-libration is forced to rotate, despite the cavity still couples to the motion. However, we have shown that each librational particle mode couples to one cavity mode exclusively. In the same manner, as we obtain the translational cavity-cavity coupling we evaluate the link to the librational motion by expanding Equation 4.37, which resulting constants read

$$g_{2\alpha} = \frac{\omega_c V}{4V_c}\cos(\phi)^2\sin(2\tilde{\theta})\left(\chi_c - \chi_b\right)\alpha_{\mathrm{zpf}}, \tag{4.61}$$

$$g_{1\beta} = \frac{\omega_c V}{4V_c}\cos(\phi)^2\pi(\chi_c - \chi_a)\beta_{\mathrm{zpf}}, \tag{4.62}$$

$$g_{1\gamma} = \frac{\omega_c V}{4V_c}\cos(\phi)^2(\chi_a - \chi_c)\gamma_{\mathrm{zpf}}. \tag{4.63}$$

In addition to the coupling terms, we find a constant term in Equation 4.46, which is identified as the cavity drive. In steady state, as we calculate for the translational motion, only the mode $s = 2$ is populated. The driving term yields

$$E_d = \sqrt{\frac{PV^2\omega_c}{2\hbar c\pi w_x w_y V_c}} \cos(\phi)\left(\cos(\tilde{\theta})\cos(\psi)\chi_c - \mathrm{i}\sin(\tilde{\theta})\sin(\psi)\chi_b\right), \tag{4.64}$$

and represents the anticipated cosinusoidal altering, such that at the cavity anti-node, the scattering in the mode is maximized.

So far, we analyzed the tweezer-cavity interaction, thereby determining the coupling of every degree of freedom $q \in \{x, y, z, \alpha, \beta, \gamma\}$ and extracting the cavity drive. Thus, we summarize the terms in the interaction Hamiltonian, which then yields

$$H_{TC} = -\hbar \sum_{q,s} \left(G_{qs} \hat{c}_s \left(\hat{b}_q^\dagger + \hat{b}_q \right) + E_d \hat{c}_2 + \text{H.c.} \right). \tag{4.65}$$

In conclusion, we have derived all the components involved in the light-nanoparticle Hamiltonian, which mathematically captures the interaction between light and the nanoparticle 4.8), such that the Hamiltonian yields

$$\begin{aligned} \frac{H}{\hbar} = &\sum_q \Omega_q \hat{b}_q^\dagger \hat{b}_q + \sum_s \omega_{cs} \hat{c}_s^\dagger \hat{c}_s - \sum_{s,q} \left(G_{sq} \hat{c}_s \left(\hat{b}_q^\dagger + \hat{b}_q \right) + E_d \hat{c}_2 + \text{H.c.} \right) \\ &- \sum_{s,q} g_{sq} \left(\hat{b}_q^\dagger + \hat{b}_q \right) \hat{c}_s^\dagger \hat{c}_s. \end{aligned} \tag{4.66}$$

Since we are particularly interested in the dynamics of the system –specifically, how the cavity manipulates the particle motion– we focus on deriving the equations of motion. Before doing so, we transform the Hamiltonian in a more convenient rotating frame by applying the unitary transformation

$$U(\omega) = \exp\left(-\mathrm{i}\omega \hat{c_s}^\dagger \hat{c}_s \right), \tag{4.67}$$

where ω is the frequency of the tweezer. This transformation shifts the cavity frequency ω_c by the frequency ω, resulting in a Hamiltonian depending on the aforementioned detuning $\Delta = \omega_c - \omega$. In a second step, we displace the operators to focus on the displacements around the steady state. Since we have already calculated that the cavity mode $\hat{c}_2$ is populated, while $\hat{c}_1$ remains empty, the cavity is displaced by γ_2

$$\hat{c}_s \to \hat{c}_s + \gamma_2. \tag{4.68}$$

After cancelling all constant terms, we arrive the following reduced expression

$$\begin{aligned} \frac{H}{\hbar} = &\sum_q \Omega_q \hat{b}_q^\dagger \hat{b}_q + \sum_s \left(\Delta_s - \sum_q g_{sq} \left(\hat{b}_q^\dagger + \hat{b}_q \right) \right) \hat{c}_s^\dagger \hat{c}_s \\ &- \sum_{s,q} \left(\left(G_{sq} + g_{sq} \gamma_2^* \right) \hat{c}_s \left(\hat{b}_q^\dagger + \hat{b}_q \right) + E_d \hat{c}_2 + \text{H.c.} \right) \end{aligned} \tag{4.69}$$

$$= \sum_q \Omega_q \hat{b}_q^\dagger \hat{b}_q + \sum_s \Delta_{\text{eff}} \hat{c}_s^\dagger \hat{c}_s - \sum_{s,q} \left(\left(G_{sq} + g_{sq} \gamma_2^* \right) \hat{c}_s \left(\hat{b}_q^\dagger + \hat{b}_q \right) + E_d \hat{c}_2 + \text{H.c.} \right), \tag{4.70}$$

where Δ_{eff} incorporates the change of the cavity frequency caused by the presence of the particle and thus the detuning.

4.3.4 Effective mode temperature

Based on the derived Hamiltonian we descirbe the the time evolution of the cavity and particle operator using the von Neumann equation

$$\dot{\hat{b}} = \frac{\mathrm{i}}{\hbar}\left[H, \hat{b}\right] - \Gamma\hat{b} + F, \tag{4.71}$$

where we modify them by adding a damping term Γ and a thermal stochastic force F describing the interaction with the thermal bath. These terms are explicitly relevant for describing the particle dynamics, hence they include the terms arising from the interaction between free-field and cavity or tweezer field, which we did not calculate specifically. The latter will lead to a recoil limit, while the cavity-free-field interaction will induce an additional decay channel for the cavity field [67]. For the dynamics of the cavity mode operator $\hat{c}_s$ the modified von Neumann equation is

$$\dot{\hat{c}}_s = -\mathrm{i}\Delta_{\mathrm{eff}}\hat{c}_s - \frac{\kappa}{2}\hat{c}_s + \mathrm{i}\left(G_{sq} + g_{sq}\gamma_2^*\right)^* q_{\mathrm{zpf}}\left(\hat{b}_q^\dagger + \hat{b}_q\right) + \mathrm{i}E_d^*\delta_{s2}, \tag{4.72}$$

where κ is the full width at half maximum of the cavity response function and hence expresses the cavity field decay. From the steady state, where we set $\dot{\hat{c}}_s = 0$ and the particle motional dependency disappears, we obtain the photon number inside the cavity. For the displacment parameter γ_2, we determine the expression

$$\gamma_2 = \frac{\mathrm{i}E_d^*}{\kappa/2 + \mathrm{i}\Delta_{\mathrm{eff}}}, \tag{4.73}$$

which relates to the cavity drive. The final photon number inside the cavity from coherent scattered light is

$$n_{\mathrm{cav}} = |\gamma_2|^2 = \frac{|E_d|^2}{(\kappa/2)^2 + \Delta_{\mathrm{eff}}^2} \tag{4.74}$$

dependent on the cavity response function, incorporating the linewidth and detuning. A different approach of calculating the photon number is derived in the Appendix B, where we investigate the orientation between particle and cavity mode and discuss the mode overlap in detail.
Nevertheless, we are committed to identifying the Langevin equation that describes the dynamics of the particle. Between the position and the momentum the relation $\dot{q} = p_q/m_q$ holds such that the motional dynamics are given by

$$\dot{p}_q = -\Omega_q^2 m_q q + \sqrt{2\hbar m_q \Omega_Q}\left(\left(G_{sq} + g_{sq}\gamma_2^*\right)\hat{c}_s + \mathrm{H.c.}\right) - \Gamma p_q + F_{th}, \tag{4.75}$$

$$\ddot{q} = -\Omega_q^2 q - \Gamma_q \dot{q} + \sqrt{\frac{2\hbar\Omega_q}{m_q}}\left(\left(G_{sq} + g_{sq}\gamma_2^*\right)\hat{c}_s + \mathrm{H.c.}\right) + \frac{F_{th}}{m_q}. \tag{4.76}$$

We solve this set of equations by transforming to Fourier space ($\mathcal{F}[q] = \tilde{q}(\omega)$), which reduces the differential equations of second order in linear order frequency space

$$\hat{\tilde{c}}_s = \frac{\mathrm{i}}{\mathrm{i}\left(\omega + \Delta_{\mathrm{eff}}\right) + \kappa/2}\left(G_{sq} + g_{sq}\gamma_2^*\right)^* \frac{\tilde{q}}{q_{\mathrm{zpf}}}, \tag{4.77}$$

$$\hat{\tilde{c}}_s^\dagger = \frac{-\mathrm{i}}{\mathrm{i}\left(\omega - \Delta_{\mathrm{eff}}\right) + \kappa/2} \left(G_{sq} + g_{sq}\gamma_2^*\right) \frac{\tilde{q}}{q_{\mathrm{zpf}}}, \tag{4.78}$$

$$\tilde{q} = \chi_m(\omega) \left(\sqrt{\frac{2\hbar\Omega_q}{m_q}} \left(\left(G_{sq} + g_{sq}\gamma_2^*\right) \hat{\tilde{c}}_s + \mathrm{H.c.} \right) + \frac{F_{th}}{m_q} \right). \tag{4.79}$$

We combine them and rewrite the solution in the form of Equation 2.22 as

$$\tilde{q} = \tilde{\chi}_m(\omega) \frac{F_{th}}{m_q}, \tag{4.80}$$

with an adapted susceptibility that covers and additional damping to the motion arising from the developed interaction terms

$$\tilde{\chi}_m(\omega)^{-1} = \Omega_q^2 - \omega^2 - \mathrm{i}\Gamma_q\omega + \left|G_{sq} + g_{sq}\gamma_2^*\right|^2 \frac{4\Omega_q\Delta_{\mathrm{eff}}}{\left(\mathrm{i}\left(\omega + \Delta_{\mathrm{eff}}\right) + \kappa/2\right)\left(\mathrm{i}\left(\omega - \Delta_{\mathrm{eff}}\right) + \kappa/2\right)} \tag{4.81}$$

$$\approx \Omega_q^2 - \omega^2 - \mathrm{i}\omega\Gamma_{\mathrm{tot}}(\omega). \tag{4.82}$$

The total damping therefore reads

$$\Gamma_{\mathrm{tot}}(\omega) = \Gamma_q + \Gamma_{\mathrm{CS}}(\omega) = \Gamma_q + \frac{4\Omega_q\Delta_{\mathrm{eff}}\kappa\left|G_{sq} + g_{sq}\gamma_2^*\right|^2}{\left(\left(\omega + \Delta_{\mathrm{eff}}\right)^2 + \kappa^2/4\right)\left(\left(\omega - \Delta_{\mathrm{eff}}\right)^2 + \kappa^2/4\right)}. \tag{4.83}$$

Additional to the thermal damping an additional damping arises from the couplings, which connects to all degrees of freedom over their coupling rates. As shown in Equation 4.5 the mode temperature decreases with the total damping. Thus, we derive an effective temperature

$$T_{\mathrm{eff}}(\omega) = \frac{m\Omega_q^2}{k_B}\langle q^2\rangle = \frac{m\Omega_q^2}{k_B}\frac{k_BT}{m\Omega_q^2}\frac{\Gamma_q}{\Gamma_q + \Gamma_{\mathrm{CS}}}. \tag{4.84}$$

For each degree of freedom, we develop the maximal damping. Therefore, we minimize the denominator of Equation 4.83 at the particle frequency. As we are working in a sideband resolved regime, indicating that $\kappa < \Omega_q$, the detuning should either be $+\Omega_q$ or $-\Omega_q$. In case where the cavity is red detuned (negative detuning $\Delta_{\mathrm{eff}} = -\Omega_q$) with respect to the tweezer, meaning the cavity frequency is smaller than the tweezer, the particle motion is heated, since it enhances the Stokes scattered sideband. For the opposite extrema, where the cavity is blue-detuned (positive detuning $\Delta_{\mathrm{eff}} = \Omega_q$), the Anti-Stokes scattering process is enhanced, such that the particle motion experience maximal cooling.
The effective mode temperature for assuming the cavity to be detuned for maximal cooling is

$$T_{\mathrm{eff}}(\Omega_q) = T\left(1 + \frac{4\left|G_{sq} + g_{sq}\gamma_s^*\right|^2}{\Gamma_q\kappa}\right)^{-1}. \tag{4.85}$$

Although we ignore the limits of cooling, we have shown that the cavity couples to all six degrees of freedom. The cavity does not require to be driven externally, the particle itself populates the cavity in mode $s = 2$. Motional cooling works simultaneously in all six degrees of freedom by optimizing the position along the cavity axis ϕ and setting an elliptical polarization ψ and rotating the polarization plane by, θ, ζ as well as choosing a detuning within the motional frequency range.

4.4 Optical setup

We extend the optical setup, as used in Chapter 3, to enable coherent scattering cooling. Therefore, we incorporate a high-finesse optical cavity in the vacuum chamber, as illustrated in Figure 4.2. Note that this drawing is rotated by 90° compared to Figure 3.1. We orientate the cavity orthogonal to the tweezer propagation direction and ensure the trapping center coincide with the cavity center. To correct for displacements, we mount the tweezer lens on a three-dimensional translation stage from SmarAct, allowing to place the particle within nanometer precision along the standing wave. The two spherical

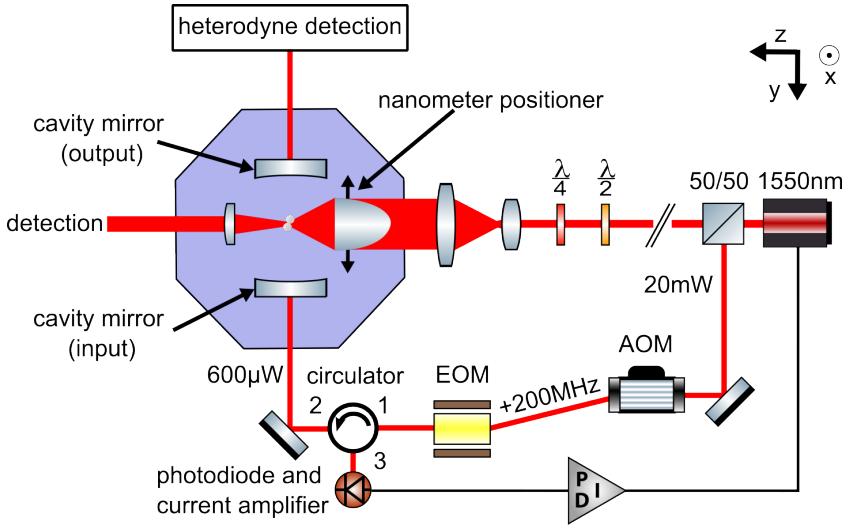

Figure 4.2: The cavity is placed orthogonal to the tweezer propagation direction. The trapping center and cavity center overlay. For positioning the particle along the standing wave, the tweezer lens is mounted to a motorized translation stage from SmarAct, capable to operate at high-vacuum. The cavity is locked with ~ 600 µW optical power. To shift the frequency by a free spectral range, the acousto-optical modulator (AOM) and electro-optical modulator (EOM) are incorporated. The EOM additionally imprints the PDH sidebands, to lock the cavity. The back-reflex is extracted using a circulator and based on the generated error signal the laser is locked via a PID regulator.

cavity mirrors are clamped to an Invar holder, which is depicted in Figure 4.3. Each mirror is hold in place with a screw. The holder maintains a stable cavity length since the material experiences low thermal expansion and the inclined design suppresses Fano resonances within the holder. Through the top opening, we launch the nanoparticles utilizing LIAD. We realign the LIAD laser beam to intersect with both tweezer focus and cavity center. During particle trapping, a bunch of particles is ablated from the sample, so we protect the sensitive cavity mirrors with a moveable cover.

4.4.1 Cavity characteristics

The optical cavity is a Fabry-Pérot interferometer, consisting of spherical mirrors from FiveNine Optics. They are specified with a reflectance $R \geq 0.99999$, a radius of curvature (RoC) of 2.5 cm and a diameter of $d = 7.75$ mm. We pre-align the cavity using a 1 330 nm diode. A sufficient large amount of light enters the cavity to observe the beam on a detector card. The light reflects by three round trips, and by adjusting the coupling mirrors we overlay the reflections and improve their profile to a circular shape in order to achieve aligning in the TEM_{00} mode. After pre-alignment, we switch back to the 1 550 nm laser modulating its frequency and improve the cavity transmission by observing the light leaking through the

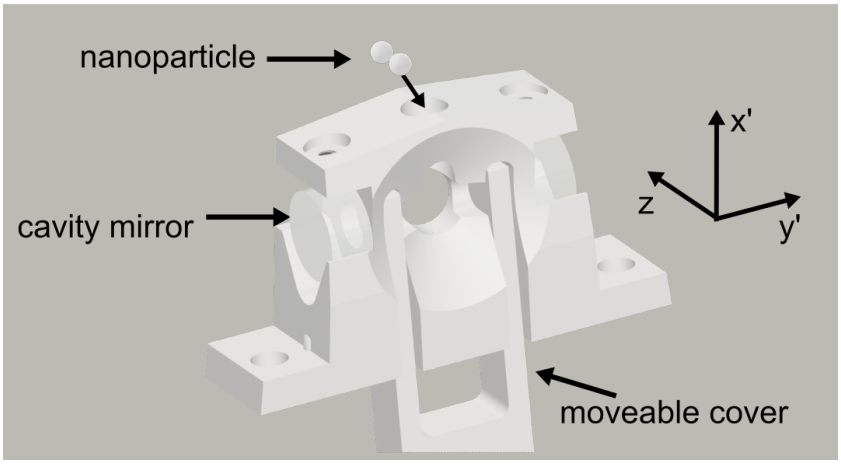

Figure 4.3: Model of the cavity holder made out of Invar. The mirrors are clamped in the holes at the side of the holder, and fixed with a screw from the top. Thus, they have three supporting points, allowing a stable mount. From the opening at the top the nanoparticles are launched while the sided cone-shaped opening allow to position the tweezer. A moveable cover can protect the inside of the cavity mirrors when launching particles.

output mirror with an attached photodiode. In the spectrum, we observe the characteristic transmission peaks as Airy peaks separated by the free spectral range. We improve for a clean mode-profile and enhance the transmission.
Further, we determine the free spectral (FSR) range by imprinting sidebands to the laser frequency employing an electro-optical modulator (EOM) (cf. Figure 4.2). We overlay the adjacent spectral peaks with the sidebands and determine a free spectral range $\nu_{\mathrm{FSR}} = (9.65190 \pm 0.00001)\,\mathrm{GHz}$, which uncertainty results from the resolution of the spectral peaks in detection. Using the free spectral range, we back-calculate the cavity length with the relation

$$L = \frac{c}{2\nu_{\mathrm{FSR}}}. \tag{4.86}$$

In our configuration, we determine a cavity length of $(15.53023 \pm 0.00015)\,\mathrm{mm}$, which is small relative to the RoC, confirming working in a stable cavity regime as per the stability criteria

$$0 \leq g_1 g_2 \leq 1, \tag{4.87}$$

where $g_1 = g_2 = 1 - L/R$. The values of g_1 and g_2 are close to zero, indicating that the cavity is operated near a confocal configuration. Along with the high stability, the waist is

$$w_c = \sqrt{\frac{\lambda}{2\pi}\sqrt{L\,(2 \times \mathrm{RoC} - L)}} \approx 75.55\,\mu\mathrm{m} \tag{4.88}$$

large compared to concentric configurations. As we align the Cavity in the TEM_{00} mode, its volume depends quadratically on the waist

$$V_c = \frac{\pi}{4} w_c^2 L \approx 0.07\,\mathrm{mm}^3. \tag{4.89}$$

and thereby leads to a large mode volume. Consequently, the coupling will be reduced as the constants scale inversely with the cavity volume (cf. Equation 4.51). In addition to the coupling, the cooling

efficiency further depends on the cavity finesse and linewidth. The cavity finesse determines the light enhancement and the cavity transmission function. Theoretical we predict a finesse of at least

$$\mathcal{F} = \frac{\pi\sqrt{R}}{1-R} \approx 300\,000, \tag{4.90}$$

which we verify experimentally employing a frequency-swept measurement, particularly suitable for high-finesse cavities. In analogy to the alignment procedure, we modulate the laser and observe the cavity response in transmission. When the cavity mode is reached, light builds up in the cavity for approximate one round trip. Due to the high reflectivity of the mirrors, the decay of the light field is slow that the cavity linewidth κ is small compared to the modulation frequency f_{mod} of our laser

$$\kappa/2\pi \approx 32\,\mathrm{kHz} \ll 4\,\mathrm{GHz} = f_{\mathrm{mod}}. \tag{4.91}$$

Thus, the cavity remains populated even when light with a different frequency impinges, causing interference of both the decaying field in the cavity and the incoming field. The resulting beating is visible in the transmission signal as Fizeau fringes (ringing) [70, 71]. For a scanning frequency approaching the free spectral range the ringing diminishes, the spectrum will look like recorded with a slow modulation frequency [71]. In conclusion, the shape of appearing fringes is related to the free spectral range and the ratio of modulation frequency to the linewidth. It is important to account for discrepancies with respect to the Airy peaks, otherwise the determined peak width gets overestimated [72]. We observe the ringing effect with our cavity scanned by 4 GHz/s in Figure 4.4. We measure the transmission with the photodiode, set to a 30 dB gain and a 260 kHz bandwidth. Using the relation for the transmitted power [73]

$$P_{\mathrm{trans}}(t) \propto \mathrm{e}^{-\kappa t}\left|\mathrm{erfc}\left\{\frac{1}{4}\frac{(1+\mathrm{i})(\kappa - 2\mathrm{i}f_{\mathrm{mod}}t)}{\sqrt{-f_{\mathrm{mod}}}}\right\}\right|^2 \tag{4.92}$$

we fit the linewidth to $\kappa = 2\pi \times (17.76 \pm 0.07)$ kHz. The modulation frequency $f_{\mathrm{mod}} = (4.9 \pm 0.1)$ GHz/s is also determined as a free parameter, matching with the anticipated outcome based on the laser settings. Of particular significance is the finesse calculation,

$$\mathcal{F} = 2\pi\frac{\nu_{\mathrm{FSR}}}{\kappa} = 543\,559 \pm 2\,091, \tag{4.93}$$

which corresponds to a reflectivity of $R = 0.9999942$, exceeding the minimum value specified by the supplier. However, it is probable that during the cavity alignment we encountered a region where the coating and, consequently, the reflectivity were superior to what we expected. To demonstrate the efficiency of our cover in safeguarding the cavity mirrors during trap loading, we conducted frequent finesse measurements and observe no notable decline. Our data consistently indicate a finesse of approximately, $\mathcal{F} = 500\,000$ with a decay rate $\kappa = 2\pi \times 20$ kHz, which we will utilize as a reference point throughout our subsequent discussions. The decay rate is small compared to the particle frequency $\kappa \ll \Omega_q$, confirming that we are operating in a sideband resolved regime and ensuring efficent cooling.

4.4.2 Cavity locking

Before running cooling experiments, we need to lock the cavity to the laser. Therefore, we employ the Pound-Drever Hall (PDH) technique [74]. To prevent interference between the locking light and the coherently scattered light from the trapped nanoparticle, we offset the lock by a free spectral range.

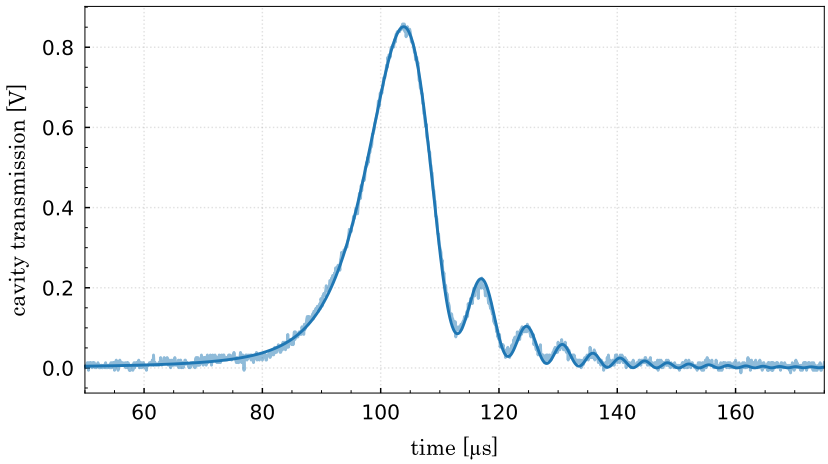

Figure 4.4: The laser internal modulates its frequency over 8 GHz with a frequency of 0.5 Hz. The transmission spectrum of the frequency swept is recorded with a photodiode set to a bandwidth of 260 kHz, which is large enough to record the cavity ringing. From the fitted ringing we extract a finesse of $\mathcal{F} \approx 500\,000$.

Nevertheless, the locking light exerts radiation pressure on the particle motion. Thus, we aim for minimal power in the locking mode.
We extract 20 mW of vertically polarized light directly from the laser to perform PDH locking, as shown in Figure 4.2. The locking technique requires a laser sideband separated in frequency from its carrier by more than the cavity linewidth ($\kappa = 2\pi \times 20\,\text{kHz}$). Therefore, we use the EOM generating sidebands at 10 MHz. When the carrier frequency becomes resonant with the cavity, it gets populated, forming a standing wave. As the light leaves the cavity through the input mirror it is phase-shifted by π, in fact each transmission through a mirror acquire a phase shift of $\pi/2$. In contrast, the sidebands, being far away from the cavity resonance and hence not populating the cavity, are reflected without a phase shift at the incoming mirror. Both the back-reflected sidebands and the phase shifted carrier signal interfere and are detected on a photodiode. For extracting the back-reflex from the incoming light, we employ a circulator. As the phase difference between the carrier and the unaltered sidebands reveal how far the laser is tuned from resonance, we extract the phase difference by demodulating the signal. Based on this, an error signal is generated, which we feed to a PID regulator locking the laser frequency.
In order to shift the lock a free spectral range away from the trapping frequency, we additionally incorporate an acousto-optical modulator (AOM). The AOM shifts the light by 200 MHz before it passes the EOM. The EOM then adds sidebands of the frequency $\nu_{\text{FSR}} - 200\,\text{MHz}$. This results in three frequency components,

$$\nu_1 = 200\,\text{MHz}, \quad \nu_2 = -\nu_{\text{FSR}} + 400\,\text{MHz}, \quad \nu_3 = \nu_{\text{FSR}}, \tag{4.94}$$

where ν_3 has the desired frequency. Modulating the phase of the EOM with 10 MHz generates the necessary PDH sidebands for ν_2 and ν_3. Thus, the combination of AOM and EOM allow locking the laser a free spectral range away. The sidebands with improper frequency (ν_1, ν_2) are rejected at the cavity input mirror and contribute to the detection noise floor.
Of the initial 20 mW laser power, a small fraction of about 600 µW enters the cavity as a lock, since most of the light is lost in the AOM, which we use to regulate the actual power. This ensures minimal radiation pressure on the particle while maintaining effective cavity locking.

4.4.3 Heterodyne detection

Once the cavity is locked a free spectral range away from the trap, the trapped particle positioned inside the cavity populates the cavity with its scattered light. To investigate this, we implement a heterodyne detection scheme by replacing the photodiode at the output mirror with the setup shown in Figure 4.5. In this scheme, the transmitted light is combined with a strong local oscillator in order to amplify the particle signal. The heterodyne detection technique thereby preserves the phase of the signal, making it sensitive to phase changes induced by the particle motion. In addition to the measurement of the phase quadratures, this detection technique is also suitable for detecting the amplitude quadratures of the scattered light. In conclusion, we can monitor the motion of the particle similar to the forward detection. In order to observe the Stokes and Anti-Stokes sidebands of the particle, the local oscillator is frequency-shifted by $\Omega_q \ll \omega_{\mathrm{lo}} = 2\pi \times 5\,\mathrm{MHz}$.

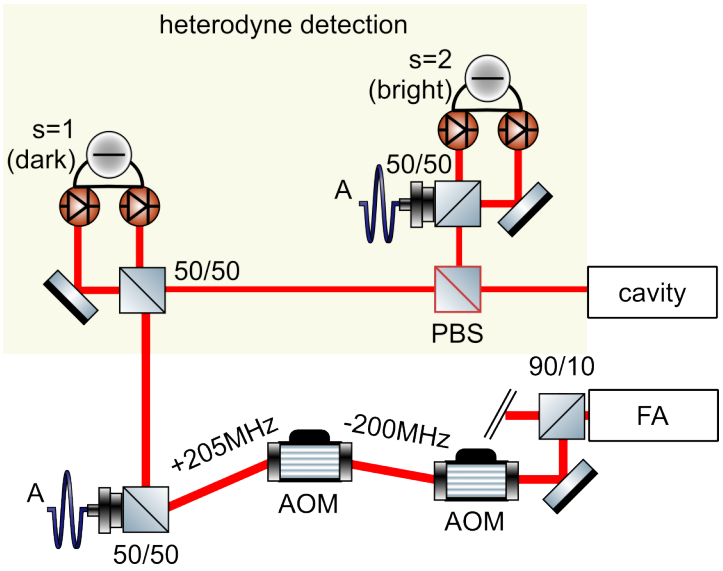

Figure 4.5: Setup for the heterodyne detection of the light leaking out the cavity mirror. The local oscillator power is extracted after the fiber amplifier. Its frequency is shifted with two AOM by 5 MHz. The signal from the cavity is split at the PBS and combined with the local oscillator at 50/50 beamsplitter. The balanced photodetectors are shot noise limited and operated close to the saturation of the Rf output.

As calculated in Section 4.3.3 the motional degrees of freedom couple to two different cavity modes $s = 1$ and $s = 2$. As the modes are orthogonal to each other, we split them utilizing a PBS. We ramp up the local oscillator power to $P = 2\,\mathrm{mW}$ for each detector, maximizing its input power, but not saturating the Rf detection output. The AC part of the amplified signal oscillates with the frequency difference between the local oscillator and the cavity signal ω_{sig}, given by

$$\Delta_{\mathrm{lo}} = \omega_{\mathrm{lo}} - \omega_{\mathrm{sig}}. \tag{4.95}$$

In the heterodyne spectrum the particle Stokes and Anti-Stokes scattered sidebands are visible as

Lorentzian shaped curves around the center frequency ω_{lo} [37, 52], that the PSD reads

$$S_{\mathrm{het}}(\omega) = \frac{1}{2} + \eta\kappa \left(\frac{\left|G_{sq} + \gamma_2^* g_{sq}\right|^2}{\kappa^2/4 + (\Delta_{\mathrm{lo}} + \omega - \Delta)^2} S_{qq}(\Delta_{\mathrm{lo}} + \omega) + \frac{\left|G_{sq} + \gamma_2^* g_{sq}\right|^2}{\kappa^2/4 + (\Delta_{\mathrm{lo}} - \omega - \Delta)^2} S_{qq}(\Delta_{\mathrm{lo}} - \omega) \right). \tag{4.96}$$

To account for losses in the detection channel and generally, not collected light transmitting through the cavity mirror, we introduce the efficiency factor η. The peak heights in the heterodyne spectrum are dependent on their coupling to the cavity mode that for example the motional z-peak is maximal visible at the anti-node, while it is strongly suppressed in the node (cf. Equation 4.51).
In the event, the cavity is on resonant with the trapping laser $\Delta = 0$ the motional peaks are symmetric around the local oscillator frequency. When detuning the cavity, its response function enhances the peaks in proximity to the detuning, while suppressing the other sidebands, as the scattering is amplified if the process is on resonance with the cavity.
For both cavity modes, we record the heterodyne spectrum in Figure 4.6. The gray signal corresponds to

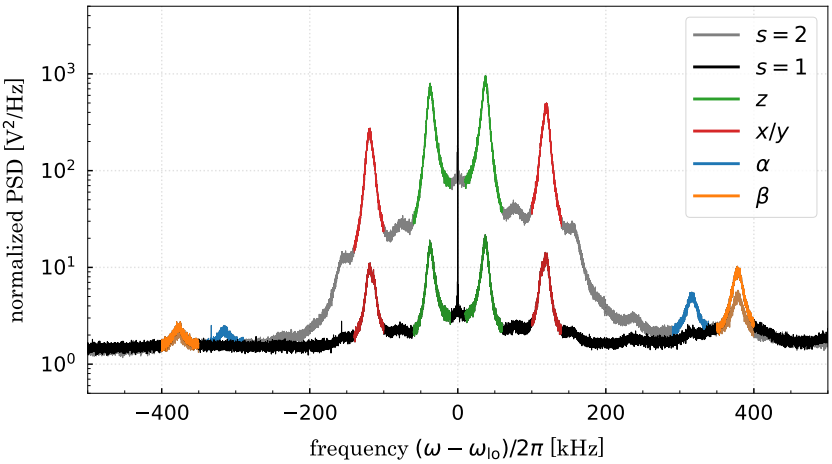

Figure 4.6: Heterodyne spectra of the two cavity modes. While most of the light is scattered in the bright mode, where the translational modes and the α-libration couple, the other mode remains dark. The light leaking in the dark mode results from the tilt between the cavity and the tweezer z-axis.

the populated mode $s = 2$, while the black curve refers to the dark mode $s = 1$. The cavity detuning is set to $\Delta = 2\pi \times 800\,\mathrm{kHz}$, that at a pressure of $p = 11\,\mathrm{mbar}$, cooling effects are insignificant. We observe the translational degrees of freedom as well as the α-libration most prominent in the bright mode, which is in accordance with the theory. Further, the noise floor around zero detuning is enhanced in the bright mode due to the Rayleigh scattering.
The β-libration is primarily visible in the dark mode. However, we also detect the translational motion with $\sim 10\,\mathrm{dB}$ suppression in this mode. Theoretically, this mode does not couple to the CoM motion. We attribute the observed deviation to a slight alignment tilt between the tweezer and the cavity. While we stated in Section 4.3.3 the tweezer and cavity to be orthogonal to each other, a perfect orthogonal alignment is experimentally challenging. Consequently, we introduce a small tilt ϑ between the tweezer propagation axis z and the cavity axis z', as illustrated in Figure 4.7.
It allows for forward scattered light to partially drive the cavity mode with the fraction of $\sin(\vartheta)^2$. We

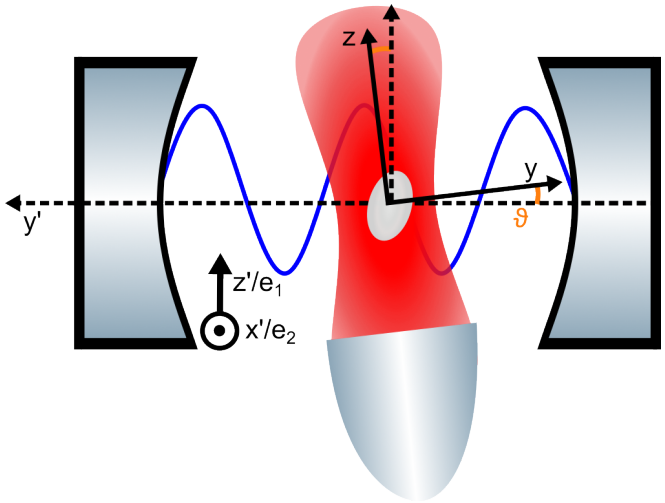

Figure 4.7: Drawing of the tweezer and cavity orientation from the top (rotated by 90° compared to Figure 4.1). The tweezer is tilted by the angle ϑ due to the alignment of cavity and tweezer itself.

measure this angle by rotating the polarization from orthogonal to parallel with respect to the cavity axis. For perfectly orthogonal alignment, we can rotate the polarization that it is parallel to the cavity axis and the light is scattered out of the cavity. In the event, where we account the small angle ϑ, the cavity is still populated, with the amount of light depending on the tilt. For both polarization configurations, we measure its corresponding heterodyne spectrum, as shown in Figure 4.8.

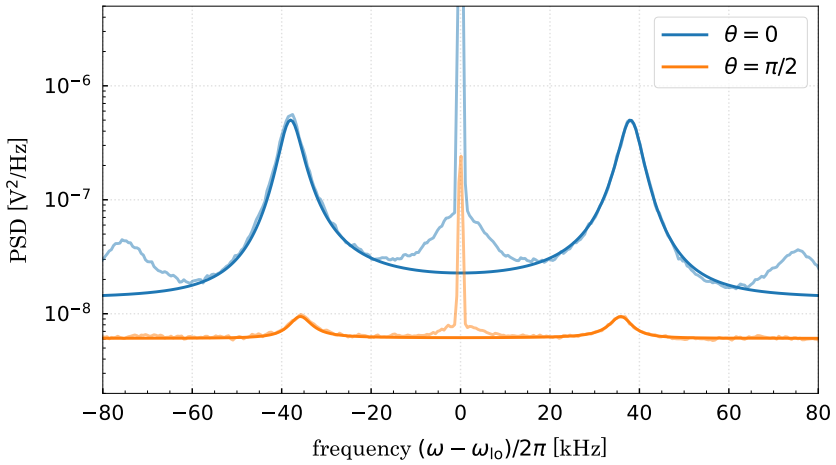

Figure 4.8: Measurement of the angle between tweezer propagation axis and cavity polarization axis $\mathbf{e}_1$. The z-peak in the orange spectrum is suppressed by 18 dB, which results from the angle tilt ϑ. For $\vartheta = 0$ the peak would not appear in the orange spectrum.

We determine for both spectra the height of z-peak (h^z_θ) by fitting a Lorentzian, from which we back-calculate the angle using the relation

$$\vartheta = \arcsin\left(\sqrt{\frac{h^z_{\pi/2}}{h^z_0}}\right) \approx 7.2^\circ. \tag{4.97}$$

Thus, we need to modify the derived theoretical framework by correcting the polarization vectors of the cavity. We find the new modes by rotating the two vectors $\mathbf{e}_1$ and $\mathbf{e}_2$ by ϑ around the x-axis using the rotation matrix

$$R_x = \begin{pmatrix} 1 & 0 & 0 \\ 0 & \cos(\vartheta) & -\sin(\vartheta) \\ 0 & \sin(\vartheta) & \cos(\vartheta) \end{pmatrix}. \tag{4.98}$$

Finally, the polarization vectors are given by

$$\tilde{\mathbf{e}}_1 = R_x \mathbf{e}_1 = \begin{pmatrix} 0 \\ -\sin(\vartheta) \\ \cos(\vartheta) \end{pmatrix}, \qquad \tilde{\mathbf{e}}_2 = R_x \mathbf{e}_2 = \begin{pmatrix} \cos(\Theta) \\ \sin(\Theta)\cos(\vartheta) \\ \sin(\Theta)\sin(\vartheta) \end{pmatrix}, \tag{4.99}$$

and lead to a coupling of the cavity mode $s = 1$ to the translational degrees of freedom as

$$\mathbf{e}_t^* \chi \tilde{\mathbf{e}}_1 = \mathrm{i}\sin(\psi)\chi_b \sin(\vartheta) \tag{4.100}$$

holds. The induced coupling is small as $\sin(\vartheta) \approx 0.12$, such that the modification can safely be neglected as long as the coupling to mode $s = 2$ does not tend to zero.
However, the small angle is the reason that the dark mode involves the translational motion and that the bright mode additionally couples to the β-libration.

4.5 Cavity population

In the heterodyne spectra, the peak on resonance corresponds to the Rayleigh scattered photons and hence the amount of light populating the cavity. As we derived in Equation 4.74 the number of photons depends on the position along the standing wave and the cavity detuning, which we keep at $\Delta = 0$. Thus, we can derive a conversion from the measured peak height to the actual photon number. Therefore, we add both heterodyne detection channels in order to minimize polarization deviations and overcome the angle deviation ϑ. When the particle is moved along the cavity axis using the translation stage in steps of 20 nm, we observe a periodic change in the peak height, indicating that the number of photons scattered alters periodically. We then extract the peak height of the PSD h_{RS} and back-calculate the expected photon number. Therefore, we assume a detection efficiency of $\eta = 0.83$ of the balanced detectors and a conversion gain of $G = 250 \times 10^3$ V/W. Thus, the expression for the power of the signal emerging from the cavity P_{out} reads

$$P_{\mathrm{out}} = \frac{h_{\mathrm{RS}}}{\eta G^2} \frac{1}{P_{\mathrm{lo}}}, \tag{4.101}$$

where P_{lo} is 2 mW. From this result, we determine the intracavity power and covert it to the photon number

$$n_{\mathrm{cav}} = \frac{\mathcal{F}}{\pi} \frac{P_{\mathrm{out}}}{\hbar\omega\nu_{\mathrm{FSR}}}, \tag{4.102}$$

where the output mirror transmission is given by $T = \pi/\mathcal{F}$. The resulting photon number is shown as the blue data in Figure 4.9. We proceed to fit the expected $\cos(\phi)^2$-dependence to the data. Based on the curve, we calibrate the particle position to the position along the cavity, thereby referring the distance

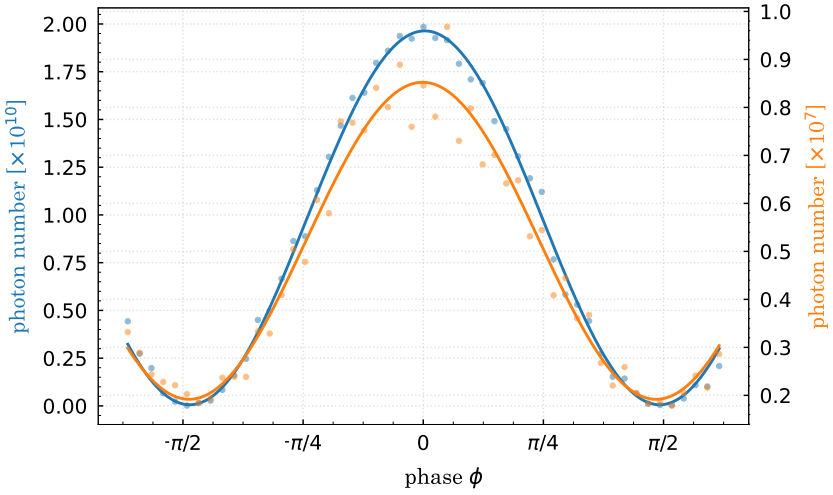

Figure 4.9: Photons populating the cavity from scattered light of the particle as a function of its position inside the cavity. The photon number is back-calculated from the recorded heterodyne spectrum with a local oscillator power $P = 2\,\mathrm{mW}$. While the photon number depends on the cavity detuning the blue dots refer to $\Delta = 0\,\mathrm{kHz}$ and the orange ones to $\Delta = 2\pi \times 600\,\mathrm{kHz}$. The measured data is represented by a $\cos(\phi)^2$ curve. The absolute photon number is also in accordance with the theoretical prediction.

between the two minima to the phase difference of π. In fact the mode function scales with $\cos(ky' - \phi)$ (cf. Equation 4.19), we expect the anti-node at $\phi = 0$ and the node at $\phi = \pi/2$. Beside the cosinusoidal dependency, we compare the absolute photon number with the theoretical prediction from Equation 4.74. For the theoretical calculation, we need to consider the shape and orientation of the trapped scattering particle. As this measurement was performed using a spherical particle ($r = 78\,\mathrm{nm}$), we can neglect the orientational dependency in Equation 4.74. Additionally, we maximized the light scattered in the cavity, adjusting the polarization angle. We calculate the photon number at the anti-node for $\Delta = 0$ to be

$$n_{\mathrm{cav}}(0) = \frac{1}{(\kappa/2)^2} \frac{P\omega_c}{2c\pi w_x w_y V_c} V^2 \chi_c^2 \approx 3.6 \times 10^{10}, \tag{4.103}$$

and compare it with the maximum photon number we measure, which was $n_{\mathrm{cav}} = 2 \times 10^{10}$. Both values are in the same order of magnitude and correspond to an intracavity power of $P > 25\,\mathrm{W}$. Note that we underestimate the measured photon number in the back-calculation. We presume only the detection efficiency η but did not consider the amount of light leaking out of the cavity but not being collected for detection. Additionally, we neglected the light losses in the optical path to the detector. Thus, we can confirm the measured photon number is in line with the prediction.

We record the measurement by finding the scattering minimum and move in 20 nm step size in each direction, recording the spectra. We choose 20 nm steps even the motor would allow a minimal step size of 1 nm in order to run the experiment faster, thereby minimizing slow drifts from affecting the measurement. Beside positional drifts of the particle along the standing wave, we observe the tweezer polarization drifting as well.

The minimal photon number we measure is $n = 4 \times 10^7$, which theoretically is supposed to be zero. Taking into account the motor precision, specified by SmarAct $\Delta y = 1\,\mathrm{nm}$. This corresponds to a minimal photon number, which is technical feasible. We calculate it by evaluating $\cos(kx - phi)^2$ in a

Taylor series around the node and determine

$$n_{\mathrm{cav}}(\pi/2) \approx n_{\mathrm{cav}}(0)k^2(\Delta y)^2 \approx 3 \times 10^5. \tag{4.104}$$

As the measured value is higher, we obtain the experimental distance to the node, which is 11 nm. In fact, this is significantly higher than we would expect, we investigate the position jittering over time. Therefore, we observe the fluctuation of the photon number at the measured node over time and convert it in a displacement. We observe in Figure 4.10 that the particle jitters around the measured minimal position with a standard deviation of 6.5 nm. Hence, we would not expect to position the particle closer to a specific position than ±6.5 nm. Further, The fluctuations are asymmetric around the measured node, indicating that the particle tends to move further away from the node rather than towards the node. The reason for that is the quadratic behavior of the photon number around the node. We conclude that in addition to the imprecision of the translation stage, there are other noise sources disturbing the particle position. From the PSD we obtain that sharp frequencies at 20 Hz, 130 Hz, and a broad peak between 50 Hz and 75 Hz dominate the positional jittering. The sharp frequency peak at 20 Hz arises from the flowbox while the other noise peaks result from the bellow, which damps the high frequency rotation (1 kHz) of the turbo pump. We record the displacement around the node with the flowbox switched off, and a hand placed on the bellow damping its low frequencies in Figure C.3. As a result, the particle jittering amplitude is smaller, with a standard deviation of 4 nm.

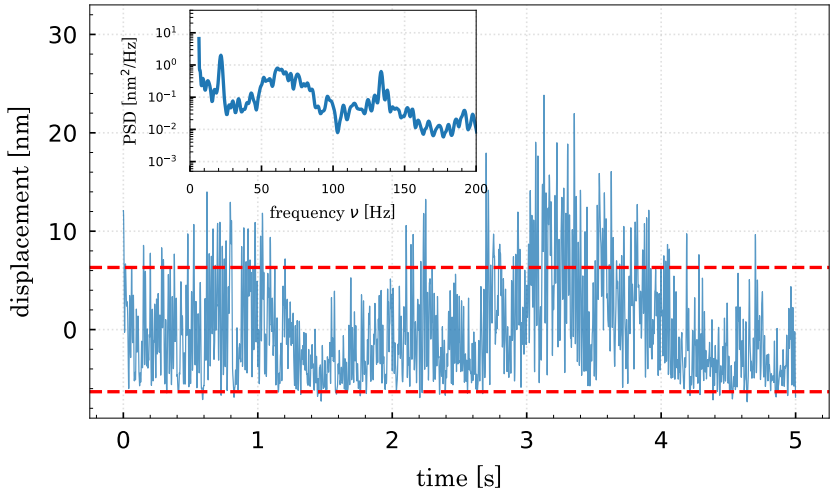

Figure 4.10: The particle jitters around the measured node (0) with an asymmetric displacement on the timescale of seconds. The red bars indicate the standard deviation, which means that the particle jitters within ±6.5 nm around the position. The PSD of noise indicates the disturbing noise peaks at 20 Hz , 60 Hz and 130 Hz

In fact, the photon number depends on the detuning of the cavity, we run the same measurement for a detuning of $\Delta = 2\pi \times 600$ kHz (Figure 4.9 orange data). As expected, the overall photon number decreases, but we still observe the position dependency. The recorded data fit well with the theory of maximal 1×10^7 photons compared to the measured 9×10^6 photons. In conclusion, we prove the scattering behavior of a spherical particle in the cavity, calibrate the position of node and anti-node and state to approach the node by a minimal distance of 11 nm.

4.6 Coupling between the motion and cavity

We continue characterizing the trapped spherical particle and henceforth analyze its motional coupling to the cavity modes. As we derived in Section 4.3, we consider the interaction between tweezer and cavity mode, as well as the self interaction of the cavity mode. In fact the cavity-cavity interaction scales with γ_2^*, the coupling strength depends on the detuning. The cavity-cavity interaction becomes stronger when more photons populate the cavity. For our purpose, we calculate the ratio of tweezer-cavity interaction to the total coupling in dependence of the detuning and demonstrate its relation in Figure 4.11. To obtain the curve, we assume the nanoparticle placed between node and anti-node maximizing the coupling g from Equation 4.38.

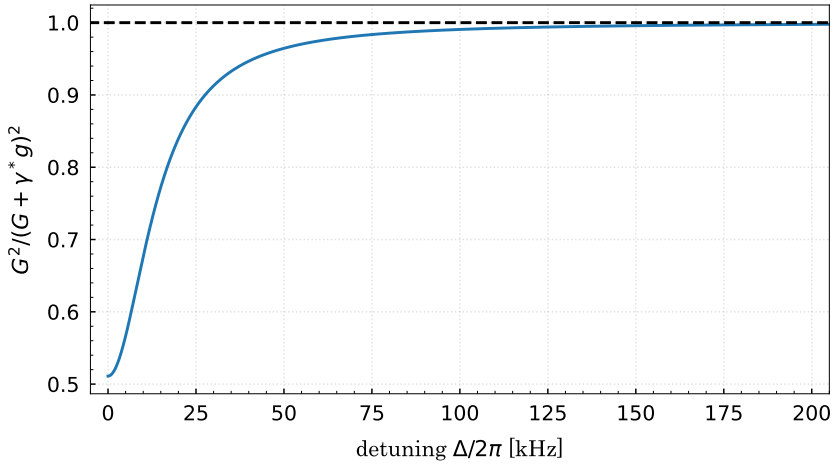

Figure 4.11: Coupling ratio of the tweezer cavity coupling and the total coupling as a function of the cavity detuning. The contribution of the cavity-cavity interaction is significantly at small detuning, in fact it scales with the photon number, which is indeed maximal for $\Delta = 0$. At detunings the experiment is typically operated with $\Delta \geq 2\pi \times 100\,\mathrm{kHz}$, $|\gamma_2^* g|^2$ is negligible, since the ratio yields $G^2/(G+\gamma_2^* g)^2 \geq 0.99$. Note that g is maximized by choosing a position between node and anti-node.

As a remark the graph holds only for the x- and y-motion, in fact for the z-motion no linear cavity-cavity coupling exists. We observe that the cavity-cavity contribution becomes less important with increasing detuning. At detunings we typically work with $\Delta \geq 2\pi \times 100\,\mathrm{kHz}$ the contribution becomes negligible as the ratio is ≥ 0.99.
In a first experiment, we keep the detuning at $\Delta = 2\pi \times 600\,\mathrm{kHz}$, so we would expect that the coupling is solely described by G. We measure the coupling for the x- and z-mode as shown in Figure 4.12. The data is obtained by extracting the peak height of the heterodyne detection sensitive to $s = 2$. According to Equation 4.96 the measured peak height corresponds to the respective coupling quadratically as long as the cavity does not introduce an asymmetry ($\Delta \gg \Omega_q$). We observe the phase shift between G_{2z} and G_{2x} as the expected dependencies are $|G_{2x}|^2 \propto \sin(\phi)^2$ and $|G_{2z}|^2 \propto \cos(\phi)^2$. We then use the calibration derived from the measurement of the photon number to obtain the position along the cavity standing wave.
From the coupling to the y-motion, which is significantly smaller, we determine the angle θ. Therefore, we use the ratio

$$\frac{|G_{2x}|}{|G_{2y}|} = \tan(\theta) \tag{4.105}$$

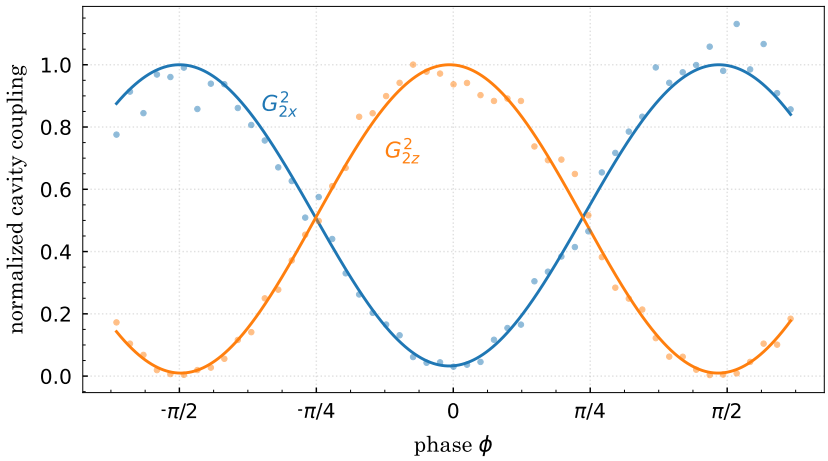

Figure 4.12: Normalized linear coupling between the translational motions and the cavity polarization mode $s = 2$. The coupling strengths G^2_{2z} and G^2_{2x} are out of phase by $\pi/2$ meaning the coupling exhibit strongest at the node for the x-motion while for the z-motion the coupling is maximal at the anti-node. The data is acquired at 10 mbar with 600 kHz detuning, so no cooling effects the measurement. The cavity is scanned in 20 nm steps and the heterodyne detection recorded.

and extract an angle of $(\theta = 0.327 \pm 0.008)\pi$, as shown in Figure 4.13. At the anti-node, we observe a plateau instead of a curve following the $\sin(\phi)^2$ dependency. The reason for this is the third harmonic of the z-motion, which arises at the anti-node and disturbs the measurement. According to Equation 4.44 the third harmonic couples to $\cos(\phi)$ as well and in terms of frequencies they coincide with each other ($\Omega_z = 36$ kHz and $\Omega_y = 105$ kHz). Hence, for extracting the angle, we dismiss the data between the black bars. Based on the determined angle, we calculate the expected coupling rates for the CoM motion. As we work with a spherical particle, we do not need to consider its orientation inside the tweezer, that the coupling rates

$$|G_{2x}| \approx 109\,\text{kHz} \times \sin(\phi), \qquad |G_{2y}| \approx 87\,\text{kHz} \times \sin(\phi), \qquad |G_{2z}| \approx 223\,\text{kHz} \times \cos(\phi) \tag{4.106}$$

solely depend on the position along the standing wave. We anticipate the coupling along the z-axis to be the strongest, because it is independent of the polarization angle and feature the largest zero-point fluctuation.

4.7 Demonstration of coherent scattering cooling

We perform coherent scattering cooling with different trapped particles following the same procedure. We start with loading a particle using LIAD at moderate pressures $p = 15$ mbar and adjusting the particle position within the cavity. Prior to commencing the locking procedure, a series of time traces in forward detection are recorded as a reference for an uncooled particle. From the recorded data sets, we determine the particle geometry and compare predicted librations with the respective measurement. Then we start locking the cavity. Despite the fact that the gas damping at this pressure exceeds any heating induced by the cavity, we proceed to lock on the cooling side, doing so at a distance that is far away from resonance. In events the trapped particle is librating, the ellipticity is rotated in proximity to circularly polarized light, thereby narrowing the gap between the librational and translational frequencies. Typically, we set the detuning between the translational and the librational modes before carefully reducing the pressure and

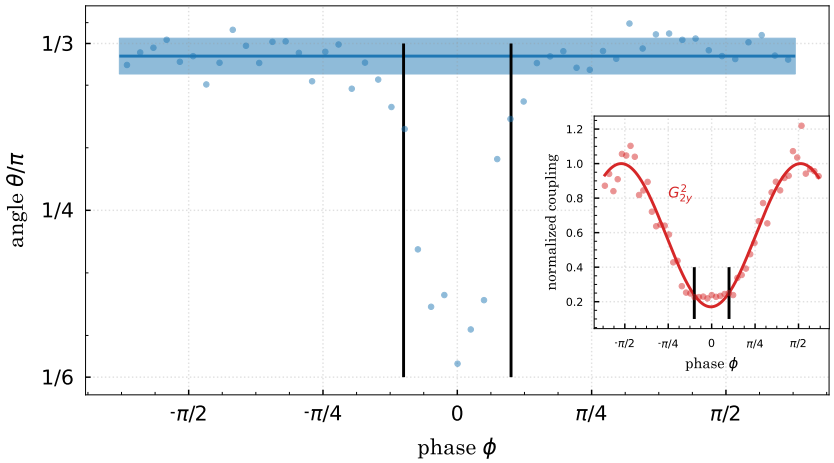

Figure 4.13: Determination of the polarization angle θ. From the ration of G_{2x}/G_{2y} the angle θ is obtained along the cavity standing wave. Around the anti-node the y-coupling tends to zero, but simultaneously the third harmonic of the z-motion arises leading to a disturbance around the anti-node. The effect is visible between the black bars and hence for the determination of θ neglected. The polarization is determined to be $(\theta = 0.327 \pm 0.008)\pi$, with the blue area indicating the error estimation.

observing the particle motion in all detection channels. The adiabatic change is slow enough to let the particle thermalize with its environment. The heterodyne spectrum with a detuning of $\Delta = 2\pi \times 180\,\mathrm{kHz}$ at $p = 2\,\mathrm{mbar}$ is shown in Figure 4.14.

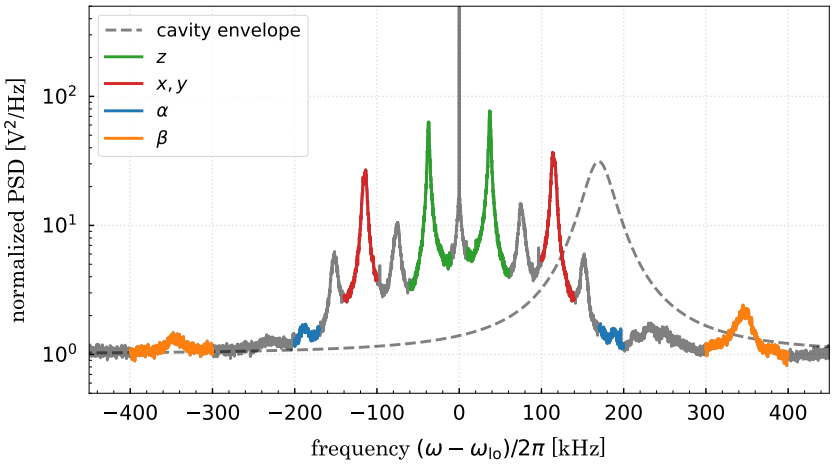

Figure 4.14: Heterodyne spectrum at $p = 2.5\,\mathrm{mbar}$ of a librating particle. The polarization is close to circularly, indicating that the x- and y-peaks are not separated. The cavity induces due to its response function characterized by its finesse and linewidth, an asymmetry. The cavity is blue-detuned with $\Delta = 2\pi \times 180\,\mathrm{kHz}$, enhancing the Anti-Stokes scattered peaks.

We observe the enhancement of the Anti-Stokes sidebands relative to the Stokes sidebands and recalculate the cavity transmission function accordingly. The cavity has a filtering effect, which induces

an asymmetry visible in the peak heights, expressed as

$$A_{\mathrm{cav}} = \frac{\kappa^2/4 + (\Delta + \Omega_q)^2}{\kappa^2/4 + (\Delta - \Omega_q)^2}. \tag{4.107}$$

In addition to the induced imbalance, there is an intrinsic asymmetry stemming from the scattering process itself. The Anti-Stokes scattering rate scales with the phonon number in this mode (n_q), while the Stokes process scales with $n_q + 1$ the asymmetry is quantified as

$$A = \frac{n_q}{n_q + 1}. \tag{4.108}$$

By carefully extracting the cavity asymmetry from the peaks and balancing the noise floor for the Stokes and Anti-Stokes sidebands, the peak heights reveal an absolute temperature measurement of the mechanical motion. As the occupation number at room temperature is on the order of $n_q = 10^7 - 10^8$, the method is only suitable for sufficiently cooled particles. Depending on the detection efficiency, we would expect to perform sideband thermometry for occupation numbers below $n_q = 10$.
As this requires high vacuum, we implement a combination of a scroll pump for pre-vacuum and a turbopump to reach pressures down to $p = 1 \times 10^{-9}$ mbar. While pumping, we implement a program continuously adjusting the cavity lock, since the refractive index and hence the optical cavity length decreases.

4.7.1 Translational cooling

With a trapped spherical particle, we lock the cavity with a detuning of $\Delta = 2\pi \times 110\,\mathrm{kHz}$ and place the particle where all translational modes are cooled. When adiabatic lowering the pressure, we record the time traces of the split and heterodyne detection. With a reference trace at $p = 8\,\mathrm{mbar}$ we determine the mode temperature from the spectral area ratio in forward detection as described in Section 4.1. While cooling, we observe a decrease in the peak height, whereby the linewidth narrows due to the pressure reduction.

The reference PSD as well as a cooled spectrum at $p = 9 \times 10^{-5}$ mbar is shown in Figure 4.15. The colored area beneath the peaks is the spectral area where the signal is above the noise floor and therefore considered for the temperature calculation. We proceed with recorded data at different pressures in the same manner, which yields the temperature-pressure dependence in Figure 4.16. We divide the curve along the pressure in three parts. In the pressure range between 0.1 mbar and 1×10^{-3} mbar the temperature reduces linearly. Then the temperature flattens, reaching a plateau before the y- and z-motional temperature decreases further at $p = 4\times10^{-5}$ mbar reaching the lowest measured temperatures of below 10 mK. The linear reduction is as anticipated, combining the effective temperature calculation from Equation 4.84 with the thermal damping in Equation 3.12, this results in

$$T_{\mathrm{eff}}(\Omega_q) \approx \frac{T\left(\left(\Omega_q + \Delta\right)^2 + \kappa^2/4\right)\left(\left(\Omega_q - \Delta\right)^2 + \kappa^2/4\right)}{4\Omega_q \Delta\kappa |G_{sq}|^2}\Gamma_q \tag{4.109}$$

$$= \frac{T\left(\left(\Omega_q + \Delta\right)^2 + \kappa^2/4\right)\left(\left(\Omega_q - \Delta\right)^2 + \kappa^2/4\right)}{4\Omega_q \Delta\kappa |G_{sq}|^2}\frac{64r^2}{3\bar{v}_{\mathrm{gas}}}p. \tag{4.110}$$

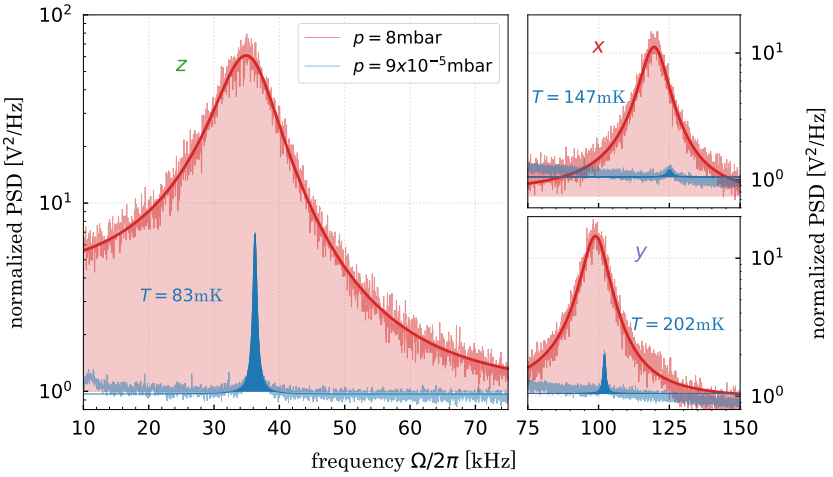

Figure 4.15: Coherent scattering cooling of the translational motion. The data in red refers to an uncooled nanoparticle at 8 mbar, serving as a reference. The mode temperature at 9×10^{-5} mbar is the relation of the two spectral areas (shaded areas). Weakest cooling is measured for the y-axis. This is caused by the tweezer polarization, which is almost linear along the y-axis ($\theta = 0.3\pi$), leading to less scattering of the motion in the cavity. The z-motion exhibits strongest cooling, since the particle is placed close to the anti-node $(0.098 \pm 0.009)\pi$.

Thus, we fit the data for each degree of freedom with a linear function. From this analysis, we extract the coupling constants for each mode, as summarized in Table 4.1. We calculate the position ϕ along the standing wave by determine the ratio of G_{2x} and G_{2y} (cf. Equation 4.51). For the polarization angle, we insert the before obtained value $\theta = 0.3\pi$ and evaluate $\phi = (0.098 \pm 0.009)\pi$. The particle is positioned near the anti-node, which maximizes the number of photons inside the cavity. According to Equation 4.74, we calculate a photon number of $n_{\mathrm{cav}} = (1.7 \pm 0.2) \times 10^8$.
At pressures below $p = 1 \times 10^{-3}$ mbar, we observe the temperature curve flattens, which is caused by phase noise heating. Phase noise arises from the used laser itself, which occurs due to different influences. Most prominent is the spontaneous photon emission of the gain medium in the laser resonator [75–77]. The phase of the emitted photon is not in line with the circulating photons caused by stimulated emission and thus adds a phase noise. In combination with cavity instabilities, the phase noise translates into amplitude noise of the interactivity field. Since the coupling scales with the number of photons, it fluctuates. As we have already observed, the impact of $\gamma_2^* g$ for the total coupling is small, this contributes less. More important is the stochastic force arising from the amplitude fluctuations. They drive the mechanical oscillator, preventing further cooling [78]. As a result, the final temperature scales with the intracavity photon number

$$T_q = \frac{\hbar \Omega_q}{k_B} \frac{S_{\dot{\phi}\dot{\phi}}}{\kappa} n_{\mathrm{cav}} + T_{\mathrm{eff}}(\Omega_q), \tag{4.111}$$

where the first term includes the phase noise limited temperature with the frequency noise $S_{\dot{\phi}\dot{\phi}}$. We fit the function to the data in Figure 4.16 and extract from the free parameters the frequency noise,

$$S_{\dot{\phi}\dot{\phi}} = \frac{k_B T_q \kappa}{\hbar \Omega_q n_{\mathrm{cav}}}. \tag{4.112}$$

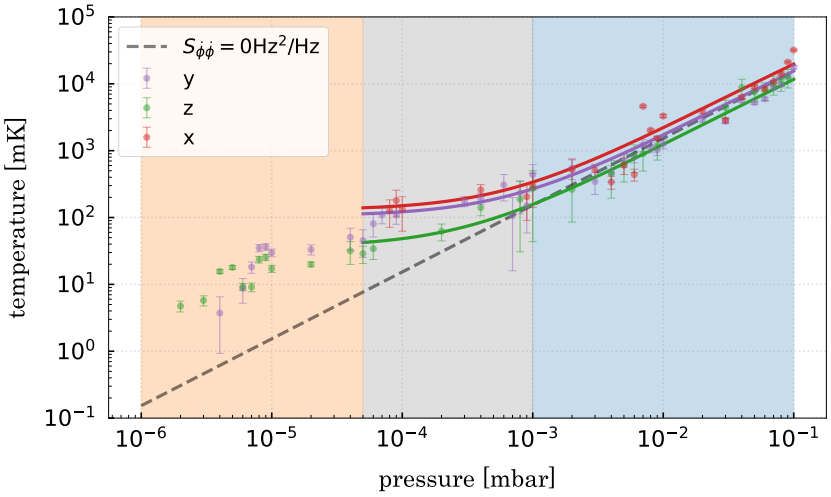

Figure 4.16: Fit of the measured temperature-pressure dependency. Ignoring any noise sources, the temperature scales linear with the pressure (dashed line). The temperature follows the linear reduction until 1×10^{-3} mbar (blue shaded area). At 100 mK cooling becomes inefficient, limiting the temperature for each degree of freedom (gray shaded area). Thereby, the solid curves represent the fitted temperature dependency including the phase noise contribution, resulting in a fitted frequency noise $S_{\dot{\phi}\dot{\phi}} = 16\,\mathrm{Hz}^2/\mathrm{Hz}$. For pressures below 4×10^{-5} mbar, the particle is positioned closer to the node, reducing the phase noise and leading to further cooling until the peaks disappear in the noise floor (orange shaded area).

The final mode temperatures for the CoM motion are

$$T_x = (129 \pm 3)\,\mathrm{mK}, \qquad T_y = (105.4 \pm 1.5)\,\mathrm{mK}, \qquad T_z = (36.2 \pm 0.6)\,\mathrm{mK}, \tag{4.113}$$

which we calculate in the phonon number according to Equation 4.1

$$n_x = (21.5 \pm 0.5) \times 10^3, \qquad n_y = (21.3 \pm 0.3) \times 10^3, \qquad n_z = (19.8 \pm 0.3) \times 10^3. \tag{4.114}$$

For each mode we evaluate the respective frequency noise and average them, thus we obtain

$$S_{\dot{\phi}\dot{\phi}} = (16 \pm 2)\,\mathrm{Hz}^2/\mathrm{Hz}. \tag{4.115}$$

Although the phase noise reduces with frequency, we average over the calculated frequency noise values, as the motional frequencies are in the same order of magnitude. The typical phase noise of the laser is specified at $f = 10\,\mathrm{kHz}$ as, $S_{\phi\phi} = -135\,\mathrm{dB(rad/\sqrt{Hz}/m)}$ which we calculate back in the frequency noise. Since the phase noise measured arises from the effective optical path length inside the cavity, we determine

$$L_{\mathrm{opt}} = \frac{\mathcal{F}}{\pi} \frac{c}{2\nu_{\mathrm{FSR}}} \approx 2.5\,\mathrm{km}, \tag{4.116}$$

where $\mathcal{F}/\pi$ denotes the number of roundtrips inside the cavity. Thus, we expect a typical frequency noise on the order of

$$S_{\dot{\phi}\dot{\phi}} = S_{\phi\phi} L_{\mathrm{opt}} f^2 \approx 20\,\mathrm{Hz}^2/\mathrm{Hz} \tag{4.117}$$

at $f = 10\,\mathrm{kHz}$, which is in good agreement to the frequency noise we extract from the fits. We summarize

the determined cooling characteristics for each translational mode in Table 4.1.

Table 4.1: Determined parameters for cooling the translational motion simultaneously at a pressure of $p = 1 \times 10^{-4}$ mbar and a position close to the anti-node $\phi = (0.098 \pm 0.009)\pi$. The final temperature is limited due to the phase noise arising inside the cavity.

mode	coupling $\lvert G_{2q} \rvert$	temperature	occupation number	cooperativity C_q
x	(34 ± 4) kHz	(129 ± 3) mK	$(21.5 \pm 0.5) \times 10^3$	0.06
y	(27 ± 3) kHz	(105.4 ± 1.5) mK	$(21.3 \pm 0.3) \times 10^3$	0.03
z	(212 ± 3) kHz	(36.2 ± 0.6) mK	$(19.8 \pm 0.3) \times 10^3$	0.65

In the heterodyne spectrum as shown in Figure 4.17, we observe similarly to the forward detection a continuous peak height decrease. We extract the cavity response function from the spectrum and show the Stokes and Anti-Stokes sidebands for the x- and y-motion. For pressures below 1×10^{-3} mbar, we observe the Anti-Stokes scattered x-peak to dip in the noise floor. This phenomenon is known as noise squashing. Since we exhibit strong cooling due to a high-finesse cavity and subsequently a high coupling, squashing occur for the blue-detuned peaks, while anti-squashing occurs for the red-detuned sidebands [79]. The noise floor for Anti-Stokes scattered light cancels, and the noise floor around the Stokes peaks gets amplified. Thus, the peak heights of Stokes and Anti-Stokes peaks differ despite considering the cavity and internal asymmetry. This prevents extracting the correct spectral area from the peaks, under- or overestimating the final temperature [80, 81].

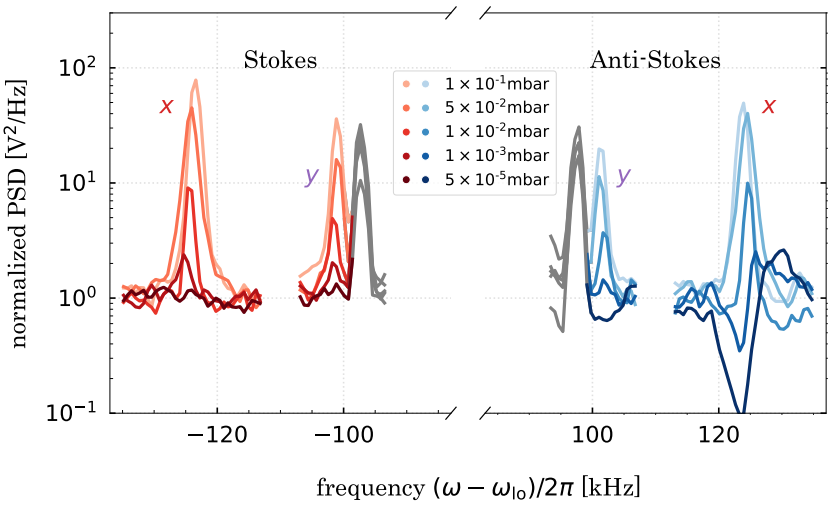

Figure 4.17: Heterodyne spectrum of the Stokes and Anti-Stokes sidebands for different pressures. At a detuning of $\Delta = 2\pi \times 110$ kHz the peak height decreases and at $p = 1 \times 10^{-3}$ mbar noise squashing at the x-peak appear, indicating cooling stronger than the noise floor can resolve. At $p = 5 \times 10^{-5}$ mbar the y-peak exhibit noise squashing as well. The dip indicates the cooling locally cancels the phase noise, thus the spectral shape is changed, underestimating the actual peak height. For the Stokes sidebands the phase noise is amplified (anti-squashing), overestimating the actual peak height. The gray peaks indicate an amplitude noise peak from the laser.

At $p = 4 \times 10^{-5}$ mbar, we adjust the position of the particle to move it closer to the node. This reduces the number of photons scattered in the cavity and therefore minimizes the impact of phase noise heating. As a result shown in Figure 4.16 the y- and z-motion are cooled further. For the x-motion, we are not able to resolve a peak, because we approach the detection limit. We report the lowest measured

temperature for the z- and y-motion to (4.5 ± 0.8) mK and (3 ± 3) mK respectively. Hence, the final observed occupation number is $n_z = (2.6 \pm 0.4) \times 10^3$ and $n_y = (0.6 \pm 0.6) \times 10^3$. The uncertainty of the y-motion rises from the detected peak. The peak is barely visible in the spectrum and would require a better signal-to-noise ratio for a precise measurement. Therefore, we need longer measurement times and a better detection efficiency. Thus, we average the spectrum over approximately one minute of measurement time, but we are not able to resolve motional peaks at lower pressures. In the heterodyne detection, sideband thermometry will offer an absolute temperature, if we account for the aforementioned discrepancies in the shape and peak height. As we obtained the occupation number around 1×10^3, even a careful analysis accounting to the squashing effects will not provide a temperature measurement, since the discrepancy in the occupation is on the order of0.1 %. Although, the detection efficiency prevents us detecting lower temperatures, the particle is still cooled, in fact coherent scattering does not require the continuous motional read out. Thus, we simulate the final occupation number for the translational motion and the particle placed at the node. Around the node, the coupling for the z-motion tends to zero (cf. Equation 4.51). In the discussion, we omit the alignment tilt ϑ of the tweezer with respect to the cavity. According to the modified polarization vectors in Equation 4.99 the coupling rate to polarization mode $s = 2$ is given by

$$G_{2z}^{\mathrm{tot}} = \sqrt{\frac{PV^2\omega_c}{2\hbar c\pi w_x w_y V_c}} \left(\mathrm{i}\cos(\phi)\left(k - \frac{1}{z_R}\right) - \sin(\phi)k\sin(\vartheta)\right) \times \left(\cos(\tilde{\theta})\cos(\psi)\chi_c - \mathrm{i}\sin(\tilde{\theta})\sin(\psi)\chi_b\right), \tag{4.118}$$

such that the coupling rate does not diminish. This ensures that the particle still experiences cooling even when positioned near the node. As calculated in Section 4.5, we are able to find the node with an uncertainty of 11 nm, leading to an intracavity photon number of $n_{\mathrm{cav}} = 4 \times 10^5$. Based on this, we simulate the final motional temperatures

$$T_x = 283\,\mu\mathrm{K}, \qquad T_y = 231\,\mu\mathrm{K}, \qquad T_z = 79\,\mu\mathrm{K}, \tag{4.119}$$

which we theoretically reach at a pressure around $p = 1 \times 10^{-9}$ mbar. The corresponding occupation number (cf. Equation 4.1) are

$$n_x = 47, \qquad n_y = 46, \qquad n_z = 44, \tag{4.120}$$

above the ground state. In conclusion, we need to discuss the heating effects hindering the particle from ground state cooling.

4.7.2 Heating mechanism

The mechanical oscillator damping rate determines the reachable occupation (cf. Equation 4.84). The system is influenced by residual gas collisions (Γ_q^{th}), radiation pressure (Γ_q^{rec}) and the coherent scattering cooling (Γ_q^{CS}) [82]. While the latter one leads to cooling the other process heat the motion and the overall damping from Equation 4.83 is extended to

$$\Gamma_{\mathrm{tot}} = \Gamma_q^{\mathrm{th}} + \Gamma_q^{\mathrm{rec}} + \Gamma_q^{\mathrm{CS}}. \tag{4.121}$$

As derived in Equation 4.85 the lowest possible temperature is related to the coupling-damping ratio. For less optical coupling, a lower pressure is required, to reach the same temperature. The final occupation

number is limited by the pressure (cf. Equation 4.111), which we calculate at $p = 1 \times 10^{-9}$ mbar to be

$$n_x^{\mathrm{th}} \approx 0.006, \qquad n_y^{\mathrm{th}} \approx 0.005, \qquad n_z^{\mathrm{th}} \approx 5. \tag{4.122}$$

We emphasize that for n_z^{th} the main limitation stems from the far detuned cavity (36 kHz < 110 kHz). For the x- and y-motion the pressure does not pose a significant limit on cooling.
Next, we investigate the radiation pressure, leading to recoil heating due to the scattering of the photons. Each photon carries a momentum, and when scattered by the particle, the momentum difference is transferred to the particle, which results over time in a scattering force. The backaction scales with the optical power, when increasing it, the scattering force is increased, while on the other hand the position uncertainty in detection decreases [83]. The recoil heating rates yield for the translational motion [21]

$$\begin{aligned}\Gamma_q^{\mathrm{rec}} = \frac{1}{5}\frac{2PV^2}{\pi\hbar c w_x w_y}\frac{k^3}{6\pi}q_{\mathrm{zpf}}\Bigg((\chi_c^2\cos(\psi)^2 + \chi_b^2\sin(\psi)^2)\left(2 + 5\left(k - \frac{1}{z_R}\right)^2\delta_{qz}\right) \\ -\chi_c^2\cos(\psi)^2\delta_{qx} - \chi_b^2\sin(\psi)^2\delta_{qy}\Bigg),\end{aligned} \tag{4.123}$$

where the prefactor arises from the scattered field from Equation 2.53. The contribution to the final temperature results from the PSD as [62, 83]

$$n_q^{\mathrm{rec}} = \frac{\kappa\Gamma_{\mathrm{rec}}}{4G_{sq}^2} \tag{4.124}$$

Thus, we obtain the occupation number due to recoil heating with the coupling strength we assumed at the node

$$n_x^{\mathrm{rec}} \approx 0.012, \qquad n_y^{\mathrm{rec}} \approx 0.044, \qquad n_z^{\mathrm{rec}} \approx 30. \tag{4.125}$$

While the recoil heating does also not affect the x- and y-motion occupation, it does for the z-motion. The reason is the weak coupling of the z-motion to the cavity.

Comparing the damping factors limiting the cooling, the recoil heating dominates over the thermal damping rate. We define the optomechanical cooperativity as

$$C_q = \frac{4G_{sq}^2}{\Gamma_q^{\mathrm{rec}} + \Gamma_q^{\mathrm{th}}} \approx \frac{1}{n_q^{\mathrm{rec}}} \tag{4.126}$$

the ratio between optical coupling strength and the coupling to the effective optical noise and thermal bath [79]. A large cooperativity is necessary to perform quantum experiments and transfer the particle to its motional ground state. As we calculated for the phase noise limited cooling at $p = 1 \times 10^{-4}$ mbar (cf. Table 4.1) the cooperativities are below $C_q < 1$. In a quantum experiment, that would mean that the decoherence of the quantum state is faster than the optical state transfer [84]. Generally, the cooperativity for each mode can be enhanced, in fact it is directly related to the Purcell factor. Thus, the cavity finesse and the ratio of light scattered in the cavity mode determine the cooperativity for this mode [62]. As a result, we aim for higher couplings by choosing a position closer to the node, reducing the recoil heating and as it is still the main limiting factor reducing the phase noise. The position can be adjusted easily with the translation stage up to the 11 nm. For reducing the optical noise, we can either reduce the laser power or launch smaller particles. Leaves us with the remaining issue, reducing the phase noise.

4.7.3 Phase noise reduction

Despite the NKT E15 laser offers the lowest achievable phase noise on the market for $\lambda = 1\,550\,\text{nm}$, we need to reduce it further. Therefore, we implement the setup shown in Figure 4.18, which is typically used measuring the linewidth of a laser. As the linewidth and the phase noise are correlated, the setup

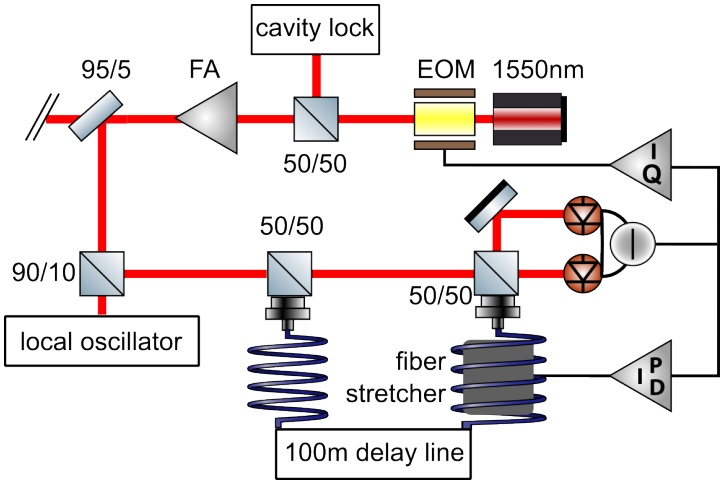

Figure 4.18: Setup to reduce the phase noise. An EOM is incorporated directly after the laser to compensate the phase noise. After the amplifier, the splits to interfere in an unbalanced Mach-Zehnder interferometer. One part of the light is delayed by a 100 m fiber line. The phase difference measured in the balanced detector is dependent on the phase noise. A PID regulates a fiber stretcher correcting slow thermal drifts, while an I/Q modulator controls the EOM, reducing the phase noise at a desired frequency.

is suitable. It is based on an unbalanced Mach-Zehnder Interferometer, where we expand one arm with a 100 m fiber delay line. Both parts are recombined at a 50/50 beamsplitter, where a balanced photodetector measures both outputs. We ensure equal optical power in both arms. In the difference signal of the detector, we measure the phase difference of the two arms, which is induced by the laser phase noise. In detection, we also acquire shot noise and fiber noise. We reduce them by using high optical power, close to detection saturation and choosing a long fiber delay line.
Based on the detected signal, we generate a feedback signal steering the EOM after the laser. Therefore, we use the I/Q module in the RedPitaya FPGA architecture [77]. First, the signal is demodulated using an electrical signal oscillating at the frequency we want to achieve phase noise reduction. Subsequently, the demodulated signal is low-pass filtered and amplified by an adjustable gain. When again mixing the signal with the electrical signal oscillating at the desired frequency, we add a phase to the signal. In fact the phase difference drifts between the two interferometer arms, we simultaneously adjust the fiber length using a fiber stretcher. This ensures a stable measurement sensitivity. We measure the signal shown in Figure 4.19. With the applied feedback at $\omega = 2\pi \times 50\,\text{kHz}$, we can reduce the phase noise by 20 dB. While the noise floor in proximity to the desired frequency is lowered, at frequencies further away the phase noise is increased. This results from adding to the fiber noise with the active feedback signal and from the phase setting. As the chosen phase is suitable for ω, it is inappropriate for frequencies further away. In combination with a high gain setting, this leads to a phase noise increase. By setting up multiple I/Q modulators and summing up their feedback signal for different frequencies, we can reduce the phase noise around different frequencies simultaneously. Thus, we can reduce the frequency noise by a factor of 100, which theoretically results in the ground state cooling for the trapped particle from previous discussion. For the translational at 1×10^{-9} mbar around the node, we would expect a final

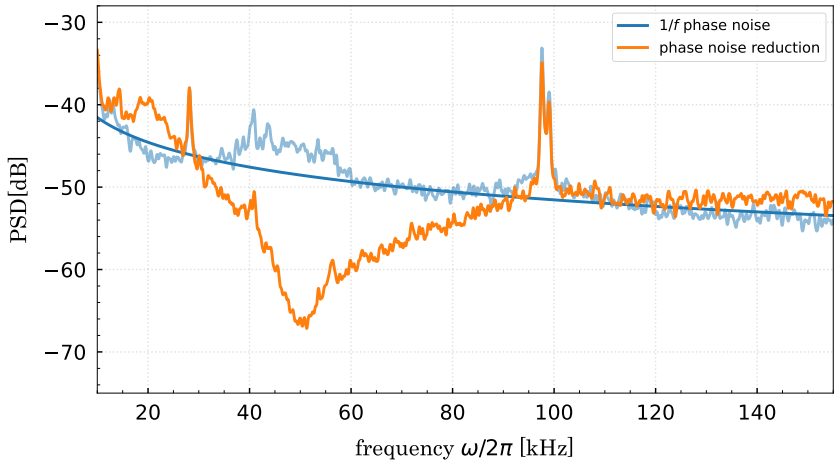

Figure 4.19: The measured laser phase noise (blue) fitted with the $1/f$ dependence. With phase modulating an EOM, the phase noise is reduced locally at 50 kHz by 20 dB (orange). At 20 kHz the phase noise is enhanced, in fact the feedback parameters are improper for this frequency.

occupation of

$$n_x \approx 0.5, \qquad n_y \approx 0.5, \qquad n_z \approx 35. \tag{4.127}$$

While the x- and y-mode are ground state cooled, the z-mode is limited due to the small cooperativity at the node and thus can only be cooled further by reducing the recoil heating.

4.7.4 Librational cooling

As we aim for rotational cooling, we are rather interested in cooling non-spherical particles. We proceed in the same manner as we do it for the spherical particles. Despite the same circumstances, we frequently lose librating particles at pressures below $p = 0.1$ mbar. In case we let the particle rotate around the tweezer axis using circularly polarized light, we circumvent this issue. In Figure 4.20 we record the stability of the translational frequencies for a trapped dumbbell. We observe at 50 ms an instability in the x- and y-motion which might arise from the diffusive γ-motion. In figure 3.11 we observe theα-libration splitting. As both traces are recorded from the same measurement record, we can compare them. At 50 ms, we observe maximal splitting for the librational mode. Thus, the translational instability occurs when mode splitting is maximal. In this event, the rotating frequency ω_γ is maximal. If we reduce the pressure further, ω_γ increases and thereby destabilizing the particle motion until the particle falls out of the trap. In comparison, the x- and y-motion for a rotating particle keep stable over the measurement time, as presented in Figure 4.21. As the γ-motion couple through the α- and β-libration, we need to cool them further in this pressure range. So we should keep the tweezer at linear polarization that both frequencies are close to each other, accompanying a maximal distance to the translational modes. Further, we need to place the particle around the anti-node and setting the detuning on resonance with the librational modes. With a rotating particle, we record the same continuous decrease of the CoM motional temperature as for the spherical particles. Additionally, the temperature is also limited by the phase noise and as the α-rotation constantly drives the particle, at some point the bound of the two particles break. We lose the particles at 1×10^{-4} mbar, where similar studies observe rotation frequencies in the GHz region [11, 18]. Further, the study [15] uses similar sized dumbbell rotating at 1.2 GHz. According to

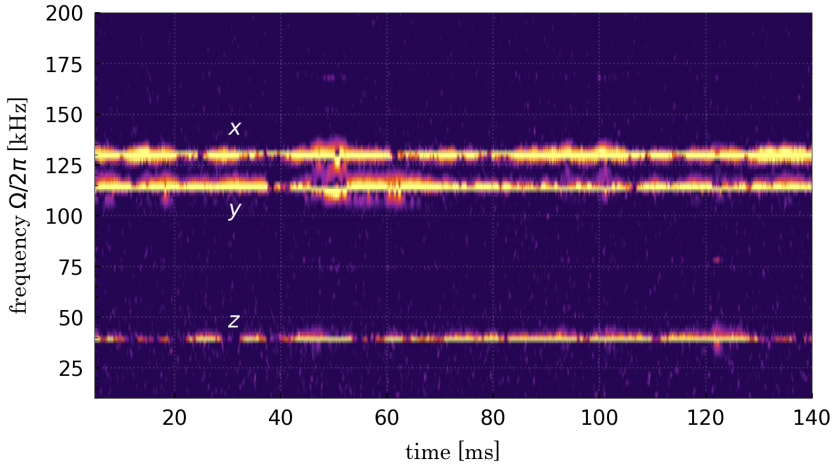

Figure 4.20: Stability of the translational frequencies for a librating particle at $p = 5 \times 10^{-2}$ mbar. Due to the diffusive γ-libration the x- and y-motion is perturbed at 50 ms destabilizing the trapped particle.

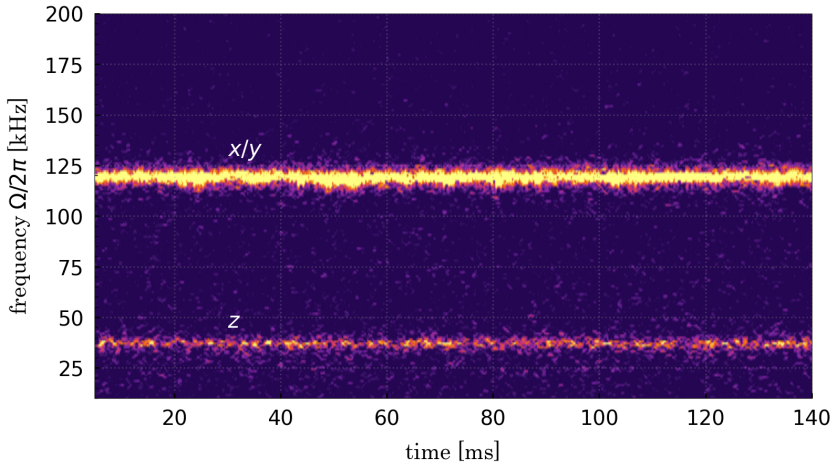

Figure 4.21: Stability of the translational frequencies for a rotating particle at $p = 5 \times 10^{-2}$ mbar.

their findings, this exhibits a stress of 13 GPa on the dumbbell, which is close to the breaking point. So we conclude, that we lose the particle, quite likely due to the fact they tear apart.

4.7.5 Simulation for librational cooling

Assuming the different approaches work out, and the particle is transferred to a state where all modes are deeply trapped such that γ is no longer diffusive, we simulate the librational cooling. Therefore, we consider a particle shaped as obtained in Equation 3.17. The simulation includes the discussed damping rates: thermal damping, recoil heating and coherent scattering damping as well as the reduced phase noise heating. To minimize the recoil heating contribution, the laser power is reduced to 100 mW. When the particle motion is cooled at low pressure around 1×10^{-6} mbar, we could experimentally lower the trapping power to 200 mW. A lower tweezer power reduces the trapping stiffness and therefore requires a high damping, which prevents the particle to escape from the trap. Consequently, it reduces the trapping frequency. However, reducing trapping power below $P = 100$ mW is not feasible, as noise

peaks appear below $2\pi \times 10\,\mathrm{kHz}$ in the heterodyne spectrum, making it difficult to extract the particle motion from the noise floor. For 100 mW the trapping frequencies are sufficiently high as listed in Table 4.2. An advantage of the reduced trapping power, is that the particle frequencies close up, which is beneficial since we aim for cooling all modes simultaneously, due to the small linewidth of the cavity transmission function ($\kappa = 2\pi \times 20\,\mathrm{kHz}$). We run our simulation at $p = 1 \times 10^{-9}$ mbar, being currently the lowest pressure, which is feasible in our setup. The program optimizes for the cavity detuning, tweezer ellipticity and polarization orientation. In analogy to the method for determining the most probable particle shape, we iterate through all possible configuration for $\psi \in [0, \pi/4], \zeta \in [0, \pi], \theta \in [0, \pi]$ and $\Delta/2\pi = (0-200)\mathrm{kHz}$ optimizing the combined lowest occupation number ($n = \sum_q n_q$). The dependence of the occupation number on the particle position is shown in Figure 4.22. Since the phase noise still

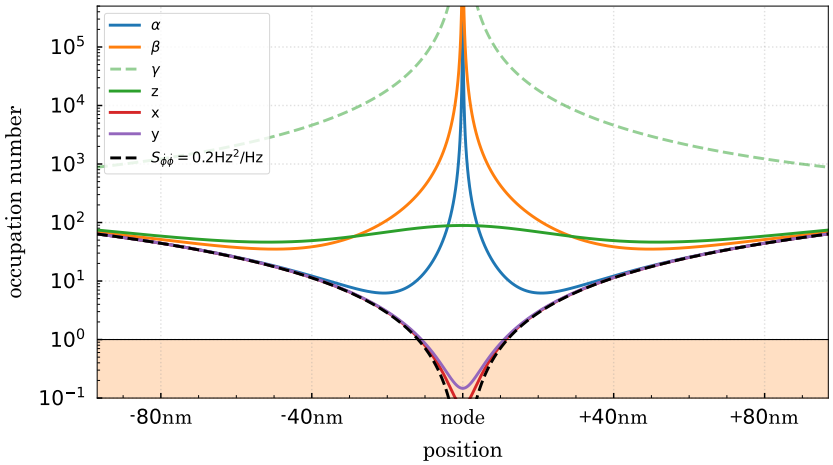

Figure 4.22: Final occupation number at a pressure $p = 1 \times 10^{-9}$ mbar, a tweezer power of $P = 100\,\mathrm{mW}$, and the particle shape calculated in Equation 3.17. Assuming a phase noise reduction of 20 dB over the frequency range. The orange marked area denotes the area where the occupation number is below 1. For cooling all degrees of freedom simultenously, only the translational motion x-and y-approach their ground state.

dominates the noise contribution, we expect the lowest achievable occupation number around the node. With the detuning of $\Delta = 2\pi \times 70\,\mathrm{kHz}$, we could achieve ground state cooling of the two translational degrees of freedom x and y. Therefore, the particle must be positioned within 12 nm around the node. Given the experimental uncertainty of 11 nm, this is within reach. However, despite the non-vanishing coupling around the node for the z-motion, it is not ground state cooled. The limitation arises on the one hand from the distance to the cavity detuning and on the other from the resolved sideband assumption, which is not fulfilled for the z-motion $\Omega_z \approx \kappa$.
For the libration we assume no significant coupling at the node. Nonetheless, the α-libration is cooled to 14 phonons at 10 nm away from the node. As expected the γ libration is barely cooled, due to the small asymmetry the coupling is small. The parameters resulting from the simulation are summarized in Table 4.2.

In a second simulation, as shown in Figure 4.23, we optimize the parameters for best librational cooling. Indeed, at the same pressure and in the region $(40 - 100)$nm away from the node, we calculate ground state cooling for the β- and α-libration. The translational modes are not ground state cooled due to the discrepancy between motional frequency and cavity detuning. The corresponding temperatures and occupation numbers are presented in Table 4.3.

We conclude that our setup is capable of cooling the trapped nano-dumbbells to their librational ground state. However, achieving the six-dimensional ground state remains unfeasible due to phase noise

Table 4.2: Determined parameter for cooling all six degrees of freedom simultaneously at $p = 1 \times 10^{-9}$ mbar and with a detuning of $\Delta = 2\pi \times 70$ kHz. With the paramters ($\psi = 0.22\pi, \theta = 0.77\pi, \zeta = 0.22\pi, \pm 11$ nm) the combined occupation number of all degrees is minimal at 11 nm away from the node.

mode q	frequency Ω_q	coupling $\lvert G_{sq}\rvert$	occupation number n_q	cooperativity C_q
α	$2\pi \times 73$ kHz	1.8 kHz	14	0.08
β	$2\pi \times 138$ kHz	1.4 kHz	428	0.12
γ	$2\pi \times 26$ kHz	0.11 kHz	72×10^3	3×10^{-4}
z	$2\pi \times 18$ kHz	26 kHz	82	0.56
x	$2\pi \times 60$ kHz	71 kHz	0.07	40
y	$2\pi \times 50$ kHz	93 kHz	0.14	56

Table 4.3: Determined parameter for cooling, especially the libration at $p = 1 \times 10^{-9}$ mbar with a detuning of $\Delta = 2\pi \times 183$ kHz. The parameters ($\psi = 0, \theta = 0.66\pi, \zeta = 0.11\pi, \pm 50$ nm) allow reaching the ground state for the α- and β- libration 50 nm qaway from the node.

mode q	frequency Ω_q	coupling $\lvert G_{sq}\rvert$	occupation number n_q	cooperativity C_q
α	$2\pi \times 177$ kHz	8 kHz	0.4	3.5
β	$2\pi \times 180$ kHz	8 kHz	0.3	3.6
z	$2\pi \times 18$ kHz	13 kHz	6×10^3	0.1
x	$2\pi \times 60$ kHz	28 kHz	35	5.9
y	$2\pi \times 50$ kHz	18 kHz	136	1.9

heating. In future experiments, we aim to launch dumbbells consisting of smaller spheres. Although they exhibit a smaller coupling, since it scales with $\sqrt{V}$, their recoil heating will decrease proportionally to V^2. Thus, the cooperativity will increase, rendering additionally ground state cooling for the z-motion feasible, soon.

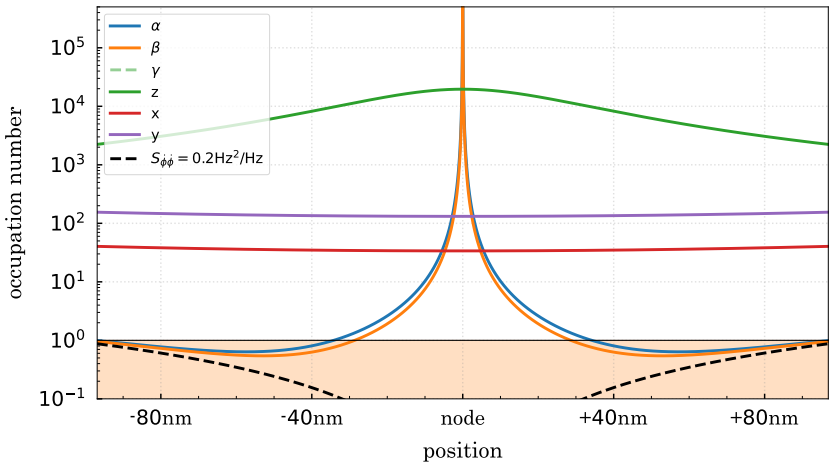

Figure 4.23: Final occupation number at a pressure $p = 1 \times 10^{-9}$ mbar, a tweezer power of $P = 100$ mW, and the particle shape calculated in Equation 3.17. Assuming a phase noise reduction of 20 dB over the frequency range. The orange marked area denotes the area where the occupation number is below unity. Detuning and angles are optimized for cooling the librations the strongest. Ground state cooling for the α- and β-libration is in experimental reach between 40 nm and 100 nm awy from the node.

CHAPTER 5

Conclusion and Outlook

We successfully demonstrated the trapping of nano-dumbbells composed of two spherical silica nanoparticles. The particle shape is acutely estimated, calculating the damping ratios of the CoM motion. Although we predicted the presence of two asymmetries in a dumbbell-shape, some particles exhibit three. Therefore, we reconstruct the particle shape as elliptical. Despite ruling out initially launching aspherical shaped particles, we infer that the particles are anisotropic. The reconstructed elliptical shape is thus a fictive particle shape featuring the same optical properties with the dimensions $r_a = (98.8 \pm 0.5)$ nm, $r_b = (100.1 \pm 0.5)$ nm and $r_c = (156 \pm 2)$ nm.
By adjusting the ellipticity of the tweezer polarization, the librational frequencies are altered accordingly. We attribute the measured frequencies to the α- and β-libration, and their behavior aligned well with simulations based on the determined particle shape. Due to the symmetry of dumbbells along their long axis, the γ-libration can evolve freely. Additionally, the γ-motion of the elliptical particle is not trapped at pressures around 10^{-2} mbar, leading to Brownian rotation, which causes observed mode-splitting in the librational frequencies. We characterize this free rotation by measuring the Brownian frequency from the frequency splitting, which scales inversely with pressure. At a pressure of 0.4 mbar, we record a frequency of $\omega_\gamma = (15.61 \pm 0.26)$ kHz. The free mode destabilize the x- and y-frequency, at pressures below 1×10^{-2} mbar, it ultimately causes the particle falling out of the trap. Driving the α-libration into rotation, the particle stability is maintained. This, in combination with coherent scattering cooling, allows the particle to be transferred in high-vacuum. The final pressure is limited by the binding strength of the two particles that form the dumbbell.

We employ a clean and soft loading technique that enables the incorporation of a high-finesse optical cavity. To protect the cavity mirrors, we designed a cover and prove its effectiveness by frequently measuring the finesse. All records consistently yield $\mathcal{F} = 500\,000$ and $\kappa = 2\pi \times 20$ kHz. Utilizing the cavity ability to enhance the scattered light from the nanoparticle, we successfully cool the CoM motion of a trapped spherical particle. We demonstrate the theoretical coupling between the mechanical motion and the cavity electrical field. To achieve simultaneous cooling of the z-, x- and y-motion, the particle is placed close to the node of the standing wave $\phi \approx \pi/10$, which enhances the light scattered into the cavity. We confirm the photon number populating the cavity as a function of the standing wave and its detuning. When comparing the measured photon numbers to the theoretical predictions, the photon number during cooling is found to be $n_{\mathrm{cav}} = (1.7 \pm 0.2) \times 10^8$. With the determined frequency noise of the laser $S_{\dot{\phi}\dot{\phi}} = (16 \pm 2)\,\mathrm{Hz}^2/\mathrm{Hz}$ around the CoM frequencies, this limits the cooling performance to temperatures of $T_x = (129 \pm 3)$ mK, $T_y = (105.4 \pm 1.5)$ mK and $T_z = (36.2 \pm 0.6)$ mK. The corresponding occupation numbers for each mode are around 20×10^3. In an effort to cool the motion further, the particle is

placed closer to the node, which we can reach up to 11 nm. The absolute positioning is limited due to low-frequency noise from the flowbox and the bellow. Although the motional temperature decreases further, with our detection efficiency in both the forward and the heterodyne detection, we could not resolve lower temperatures than 3 mK. However, we calculated that even the phase noise around the node hinders us from ground state cooling. To address this, we utilized an unbalanced Mach-Zehnder interferometer with a delay over 100 m in one arm, allowing us to directly measure the laser phase noise and reduce it by 20 dB around desired frequencies. With this reduction, we simulate ground state cooling of the translational x- and y-motion at pressures of 1×10^{-9} mbar within 12 nm around the node.
For the librational motion, we predict occupation numbers of $n_\alpha = 14, n_\beta = 428$ and $n_\gamma = 72 \times 10^3$. Since their coupling to the cavity is minimal, with cooperativities less than unity, we do not expect these modes to reach their ground state. We simulate that they are ground state cooled 40 nm away from the node.
In conclusion, we performed fundamental measurements and characterizations of the trapped nano-dumbbells. The experimental setup shows promise for simultaneously achieving six-dimensional cooling into the quantum regime, along with recording the librational ground state in the near future.

5.1 Quantum interference

The quantum control over the nanoparticle motion opens the door to interference experiments that uncover their quantum nature. In current state-of-the-art experiments, optically levitated silica nanoparticles with diameters of 100 nm (10^8 amu) are delocalized along the z-axis with a coherence length of approximately 100 nm, exceeding the zero-point fluctuation [42]. This delocalization is achieved by adjusting the trap potential within pulses synchronized with the particle frequency. By softening the trap, thereby lowering the restoring force, over the time t the delocalization increases. To counteract acquired momentum gained from stray fields, the trap stiffness is restored for a quarter of the mechanical period, flipping the orientation in phase space and the sign of the momentum. After a second delocalization period with the duration t, the trap is restored again. This results in the state alternating periodically between delocalization and localization along the z-axis.
For delocalization beyond the particle extent, rotational interference experiments are suggested.

5.1.1 Quantum state revivals

A proposed method for rotational interference experiments involves quantum state revivals, which are particularly suitable for levitated aspherical nanoparticles [45]. To achieve this, the particle must be tightly orientated within the trap. This initial step requires cooling the librational motion below one Kelvin, but not to its librational ground state. While cooling the CoM motion is not essential, it would enhance the stability [12] and minimize disturbance arising from the mode coupling. Based on our simulations, the setup shows promise for realizing this state. If the particle orientation is sufficiently confined, hundreds to thousands of angular momenta $\mathbf{J}$ are occupied in Fourier space. Releasing the particle by switching off the tweezer laser leads to a free evolution of the orientational state. The time evolution of the state in the angular momentum basis $|jm_j\rangle$ is given by

$$|\psi(t)\rangle = \sum_{j,m_j} \exp\left(-\mathrm{i}\frac{\hbar}{2I} t j(j+1)\right) |jm_j\rangle, \tag{5.1}$$

where I denotes the moment of inertia around the rotation axis, which for a dumbbell corresponds to its long axis. Since the angular quantum number j takes only integer values, the state is restored after the revival time

$$t_{\mathrm{rev}} = \frac{2\pi I}{\hbar}. \tag{5.2}$$

Hence, the particle returns to its initial orientation after multiples of the revival time. One can measure this orientation using a probe beam, provided no decoherence effect destroys the delocalization. The proposal assumes that a single collisional event localizes the particle. For reducing the collisions with the residual gas, a pressure of 1×10^{-9} mbar is sufficient. Additionally, the particle emits black body radiation depending on its internal temperature, which suggests the experiment should be conducted within a cryostat.
For the trapped dumbbells in our experiment, we would expect a revival time of $t_{\mathrm{rev}} \approx 100\,\mathrm{min}$. During this period, the particle falls in the gravity field approximately 1×10^6 km. Thus, probing the orientational revival is only feasible with smaller particles like dumbbells formed of particles with a diameter of 20 nm (1×10^7 amu). The revival time is significantly smaller that the particle falls a few millimeters. After observing the quantum revival, the particle could be recaptured when switching the trap back on, allowing the interference experiment to be repeated with the same particle.

5.1.2 Tennis racket flips

Another rotational interference experiment is based on the classical observed tennis racket flips [44, 46]. An elliptical particle feature three different moments of inertia around which the particle could rotate. While the rotation around the largest and the smallest moment of inertia is stable, the rotation around the mid-axis is unstable. After a full rotation around the mid-axis, the axis itself undergoes a rotation of π [85]. For a classical rotor, aligned for mid-axis rotation the tennis racket flips decay quickly, in fact their flipping periods for the occupied angular momenta state are widely spread. However, for a quantum mechanical rotator, the tennis racket flips are preserved and last longer than classically expected. For a quantum mechanical system, a probability for tunneling between states with opposite angular momentum exists. With strong support in the region of tunneling, the quantum flips lasts longer than classical. The tunneling probability can be enhanced by reducing the motional temperature [46]. Therefore, this scheme also requires millikelvin cooled librational modes and a controlled drive for regulating the rotation around the mid-axis. After the rotation evolve freely, when switching off the optical fields, one can probe the mid-axis orientation. Compared to the quantum state revival scheme, this technique requires free evolution times of a few microseconds and is thus suitable for the particle sizes we currently trap, rendering the rotational interference experiment doable.

APPENDIX A

Euler angles

The transformation of the susceptibility tensor from the particle to the laboratory frame is given by Equation 2.27. For the sake of completeness and transparency of the calculations provided in the main text, we derive the components of the transformed susceptibility tensor in terms of the Euler angles:

$$\chi = \begin{pmatrix} \chi_{11} & \chi_{12} & \chi_{13} \\ \chi_{12} & \chi_{22} & \chi_{23} \\ \chi_{13} & \chi_{23} & \chi_{33} \end{pmatrix} \tag{A.1}$$

diagonal terms:

$$\begin{aligned} \chi_{11} = {} & \chi_a \left(\cos(\alpha)\cos(\beta)\cos(\gamma) - \sin(\alpha)\sin(\gamma)\right)^2 \\ & + \chi_b \left(\cos(\alpha)\cos(\beta)\sin(\gamma) + \sin(\alpha)\cos(\gamma)\right)^2 \\ & + \chi_c \cos(\alpha)^2 \sin(\beta)^2 \end{aligned} \tag{A.2}$$

$$\begin{aligned} \chi_{22} = {} & \chi_a \left(\sin(\alpha)\cos(\beta)\cos(\gamma) + \cos(\alpha)\sin(\gamma)\right)^2 \\ & + \chi_b \left(\cos(\alpha)\cos(\gamma) - \sin(\alpha)\cos(\beta)\sin(\gamma)\right)^2 \\ & + \chi_c \sin(\alpha)^2 \sin(\beta)^2 \end{aligned} \tag{A.3}$$

$$\chi_{33} = \chi_a \cos(\alpha)^2 \sin(\beta)^2 + \chi_b \sin(\alpha)^2 \sin(\beta)^2 + \chi_c \cos(\beta)^2 \tag{A.4}$$

off-diagonal terms:

$$\begin{aligned} \chi_{12} = {} & \chi_a \left(\sin(\alpha)\cos(\beta)\cos(\gamma) + \cos(\alpha)\sin(\gamma)\right) \\ & \times \left(\cos(\alpha)\cos(\beta)\cos(\gamma) - \sin(\alpha)\sin(\gamma)\right) \\ & + \chi_b \left(\sin(\alpha)\cos(\beta)\sin(\gamma) - \cos(\alpha)\cos(\gamma)\right) \\ & \times \left(\cos(\alpha)\cos(\beta)\sin(\gamma) - \sin(\alpha)\cos(\gamma)\right) \\ & + \chi_c \sin(\beta)^2 \sin(2\alpha)/2 \end{aligned} \tag{A.5}$$

$$\begin{aligned}\chi_{13} = \chi_a &\left(\sin(\alpha)\sin(\gamma) - \cos(\alpha)\cos(\beta)\cos(\gamma)\right)\cos(\gamma)\sin(\beta) \\ &- \chi_b \left(\cos(\alpha)\cos(\beta)\sin(\gamma) + \sin(\alpha)\cos(\gamma)\right)\sin(\gamma)\sin(\beta) \\ &+ \chi_c \cos(\alpha)\sin(2\beta)/2\end{aligned} \tag{A.6}$$

$$\begin{aligned}\chi_{23} = \chi_a &\left(\sin(\alpha)\cos(\beta)\cos(\gamma) + \cos(\alpha)\sin(\gamma)\right)(-1)\cos(\gamma)\sin(\beta) \\ &+ \chi_b \left(\cos(\alpha)\cos(\gamma) - \sin(\alpha)\cos(\beta)\sin(\beta)\right)\sin(\gamma)\sin(\beta) \\ &+ \chi_c \sin(\alpha)\sin(2\beta)/2\end{aligned} \tag{A.7}$$

APPENDIX B

Scattering properties of small particles

It is of vital importance to study the distinctive scattering behavior of the nanoparticles, as the scattered light leads to cooling inside the optical cavity. The particle itself is small compared to the light 1 550 nm wavelength. Therefore, we can simplify the interaction, by assuming that the particle placed within a homogenous electric field $\mathbf{E}_T$ and applying the dipole approximation [47]. For the induced dipole moment, the relation

$$\mathbf{p} = \alpha \mathbf{E}_T \tag{B.1}$$

holds, where the polarizability α is expressed as $\varepsilon_0 V \chi$ (Rayleigh-Gans approximation). The radiated dipole field from the nanoparticle

$$\mathbf{E}_{\mathrm{rad}}(\xi, R) = \frac{\mathrm{e}^{\mathrm{i}kR} k^2 \sin(\xi) V \chi}{4\pi R} \mathbf{E}_T \tag{B.2}$$

consists of spherical waves and has an angular dependency ξ, with respect to the dipole axis. Thus, the scattered filed is suppressed along the dipole axis and its maximum when orientated orthogonally to it. If the incoming tweezer polarization coincide with the cavity axis, light is scattered out off the cavity. The strongest overlay is achieved when polarizing the light orthogonal to the cavity axis. Furthermore, the ratio of scattered light populating the cavity is depending on the mode overlap. We can not presume the particle radiating solely in the TEM_{00} mode. So we calculate the overlap, where we suppose the cavity axis along the x-axis and any radial displacement to be ρ. The mode matching β value is the surface integral over radiated and cavity field [62], where we only concern the cavity mode orthogonal to the tweezer propagation ($s = 2$), as the other can not be populated

$$\beta = \frac{2V}{w_c^2 \pi} \frac{\mathbf{e}_T \chi \mathbf{e}_2}{\mathbf{e}_T \mathbf{e}_2} \int_0^{2\pi} \mathrm{d}\phi \int_0^{\infty} \mathrm{d}\rho E_c E_T \frac{k^2 \sin(\xi)}{4\pi} \frac{\mathrm{e}^{\mathrm{i}k\left(x+\rho^2/2x\right)}}{x} = \frac{kV}{w_c^2 \pi} \frac{\mathbf{e}_T \chi \mathbf{e}_2}{\mathbf{e}_T \mathbf{e}_2} \sin(\xi) \tag{B.3}$$

As described qualitatively, the mode matching is maximal for $\xi = \pi/2$ and vanishes for $\xi = 0$. Its absolute value is mainly dependent on the ratio kV/w_c^2. Given that the particle is way smaller than the wavelength and the cavity waist, the ratio is 1×10^{-6} leading to a mode matching is significantly smaller than unity. Nevertheless, the particle drives the cavity mode, which electric field becomes

$$\mathbf{E} = \mathrm{i}\beta \mathbf{E}_T. \tag{B.4}$$

As a remark we consider the particle sitting in the cavity, such that the electric field is scattered in both directions in the cavity, consequently, we need to multiply the resulting power by a factor of 2

$$P_{\mathrm{scat}} = 2|\beta|^2 \frac{w_c^2}{w_x w_y} P. \tag{B.5}$$

Additionally, the cavity enhances the scattered power by $2\mathcal{F}/\pi$. Notably, the two mirrors exhibit a similar high reflectivity, such that $(1-R)^{-1} \approx \mathcal{F}/\pi$ holds. The maximum intracavity power for $\xi = \pi/2$ is

$$P_c = \frac{\nu_{\mathrm{FSR}}}{(\kappa/2)^2} \frac{P\omega k}{2\pi w_x w_y V_c} V^2 \left((\cos(\tilde{\theta})\cos(\psi)\chi_c)^2 + (\sin(\tilde{\theta})\sin(\psi)\chi_b)^2 \right) \cos(\phi)^2 \tag{B.6}$$

with the cavity mode dependent on θ. In the calculation, the cavity volume $V_c = \pi L w_c^2/4$ is introduced. Furthermore, the optical power is converted in the photon number

$$n = \frac{P}{\hbar\omega\nu_{\mathrm{FSR}}}, \tag{B.7}$$

which yields the same result as obtained in Equation 4.74 without considering the detuning.

APPENDIX C

Additional cooling results

While cooling the nanoparticle motion using coherent scattering cooling, we observe characteristic effects accompanying the cooling results from the main text in Section 4.7. Here, we investigate how the tweezer polarization influences the translational cooling and analyze neglected quadratic effects deforming the tweezer trapping potential

C.1 Polarization dependent cooling

We can adjust the cooling strength of the translational x- and y-mode by rotating the polarization. As the coupling strength depends on the polarization orientation with respect to the cavity, we can calibrate the used half and quarter waveplates. At $p = 1 \times 10^{-3}$ mbar we rotate the polarization, maximizing the cooling for the x-mode. As shown in the forward detection spectrum in Figure C.1 the x-peak at $\Omega_x = 2\pi \times 123\,\mathrm{kHz}$ vanishes for $\theta = \pi/2$, while the y-peak is less cooled at $\Omega_y = 2\pi \times 110\,\mathrm{kHz}$. As the curve shaped deviates from the Lorentzian shaped fit, we conclude that the amplitude of the oscillation is still large enough to encounter non-linear trapping regions. When rotating the polarization by $\pi/2$ that $\theta = 0$ we observe the y-mode being cooled while the x-motion is heated. The frequency change of the mode is caused by the change in coupling. The effect is also visible for the z-motion. C.1

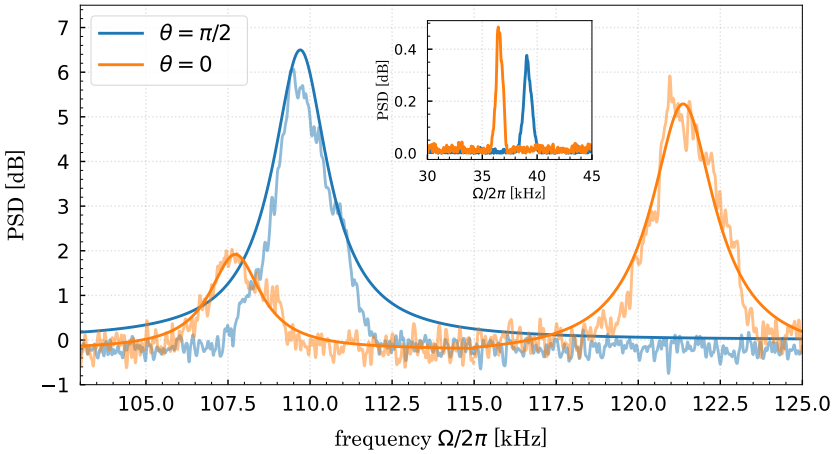

Figure C.1: Recorded traces at 1×10^{-3} mbar with a tweezer polarization orthogonal to the cavity axis ($\theta = 0$) and along the axis ($\theta = \pi/2$)

C.2 Effective motional frequency

In the theoretical analysis of coherent scattering cooling (cf. Section 4.3), we linearized the mode functions of the cavity and the tweezer to calculate the motional couplings. Thus, we omit quadratic terms arising from the cavity that influence the trapping potential. We derive these effects for the translational motion by extending Equation 4.25 to the second order

$$f_c(\mathbf{r}) \approx \cos(\phi) + \sin(\phi)k(x\sin(\theta) + y\cos(\theta)) - \frac{1}{2}\cos(\phi)k^2(x\sin(\theta) + y\cos(\theta))^2 + O(q^3). \quad \text{(C.1)}$$

From inserting the second order terms in Equation 4.43 we derive the quadratic coupling terms

$$\mathcal{G}_x = -\frac{1}{2}G_{2x}k\sin(\theta)\frac{\cos(\phi)^2}{\sin(\phi)}x_{\mathrm{zpf}}, \quad \text{(C.2)}$$

$$\mathcal{G}_y = -\frac{1}{2}G_{2y}k\cos(\theta)\frac{\cos(\phi)^2}{\sin(\phi)}y_{\mathrm{zpf}}, \quad \text{(C.3)}$$

$$\mathcal{G}_z = -\frac{1}{2}G_{2x}\left(k - \frac{1}{z_r}\right)z_{\mathrm{zpf}}. \quad \text{(C.4)}$$

We continue by adding the coupling Hamiltonian

$$\frac{H}{\hbar} = -\sum_q \left(\mathcal{G}_q\hat{c}_s\left(\hat{b}_q^\dagger + \hat{b}_q\right)^2\hat{c}_2 + \mathrm{H.c.}\right) \quad \text{(C.5)}$$

to the total interaction Hamiltonian in Equation 4.66. After displacing the cavity operators 4.68 we combine the terms proportional to $\hat{b}_q^\dagger\hat{b}_q$. Thus, the motional frequency is modified, which absolute value we calculate by solving the equations of motion

$$\Omega_{q,\mathrm{eff}}(\omega) = \sqrt{\Omega_q^2 - \frac{4\Omega_q\Delta_{\mathrm{eff}}\kappa|G_{sq}|^2\left(\Delta_{\mathrm{eff}}^2 - \omega^2 + \kappa^2/4\right)}{\left(\left(\omega + \Delta_{\mathrm{eff}}\right)^2 + \kappa^2/4\right)\left(\left(\omega - \Delta_{\mathrm{eff}}\right)^2 + \kappa^2/4\right)}}. \quad \text{(C.6)}$$

The motional frequency of a trapped particle is influenced by the cavity coupling, its transmission function and its detuning. We observe during coherent scattering cooling the motional frequency in dependence of the pressure as shown in Figure C.2. We attribute the linear increase with decreasing pressure to the change in detuning. With decreasing pressure, the refractive index and thus the cavity resonance changes. The effective detuning thus decreases as well and lead to a small frequency increase. In the pressure range between 0.1 mbar and 1×10^{-4} mbar the frequencies change by 1.8 %. At 1×10^{-4} mbar we change the position along the cavity axis towards the node, thereby, the coupling rates of the x- and y-mode increase. This results in a decrease of the frequency. The effect is similarly visible for the y-mode, also it is weaker due to the overall smaller coupling. For the z-motion, the coupling around the node becomes weaker and therefore the motional frequency increases further.

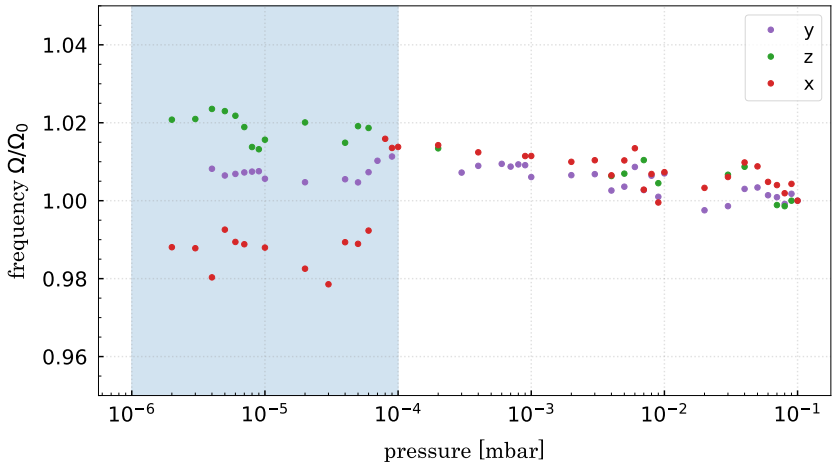

Figure C.2: The motional frequency depends on the cavity parameters. While cooling the motion and simultaneously transferring the particle to high vacuum, the particle frequency increases. The frequency for each mode is normalized to the measured frequency Ω_0 in absence of the cavity. For pressures below $p = 1 \times 10^{-4}$ mbar (marked in blue) the particle is shifted towards the node, leading to a change in the coupling constants.

C.3 Particle jittering

Placing the particle at the node of the cavity standing wave is limited by external noise sources. Here, we investigate their origin. As stated in the main, the particle fluctuates within 6.5 nm around the node (cf. Figure 4.10). We find, that the noise sources are in a low frequency range. In our experimental setup, we use a flowbox to protect the sensitive optics from dust and carry away the heat from the electrical components and the laser. When switching it off, we observe the fluctuations decreasing. Furthermore, the bellow damping the motion of our turbopump has a resonance frequency at lower frequencies. By holding a hand on the bellow, thereby damping it, the displacement noise reduces further. We record in Figure C.3 the improved positional displacement noise. The mean displacement is reduced to 4 nm.

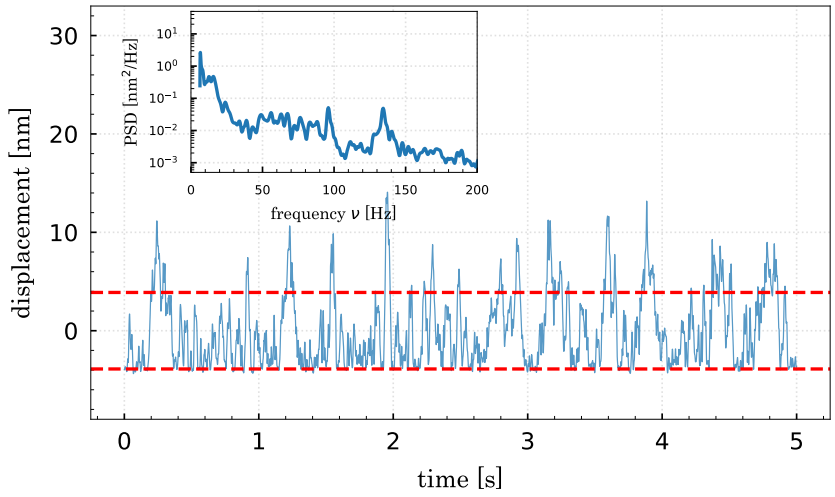

Figure C.3: Measurement of the particle jittering around the node, without disturbance from the flowbox and a manually damping of the bellow. In the noise spectrum, the peaks at 20 Hz and 75 Hz are suppressed, thus that the mean displacement reduces to ±4 nm

Although this is an improvement, it is above the minimal resolution of our translation stage (1 nm). This might arise from its operation mode. In fact, the pressure decrease influence we need to adjust the position during pumping. Therefore, we apply a voltage to the motor, moving the particle to the desired position, the stage then automatically adjusts for drifts by varying the voltage around the set offset. This correction is less precise when the voltage level is not set to zero. Thus, for minimizing the displacement noise, we should place the particle and set the voltage back to zero, before performing measurements.

Bibliography

[1] A. Ashkin, J. M. Dziedzic, J. E. Bjorkholm, and S. Chu, "Observation of a single-beam gradient force optical trap for dielectric particles," Opt. Lett. **11**, 288–290 (1986).

[2] A. Ashkin, "Optical trapping and manipulation of neutral particles using lasers," Proc. Natl. Acad. Sci. USA (1997).

[3] S. Kuhn, B. A. Stickler, A. Kosloff, F. Patolsky, K. Hornberger, M. Arndt, and J. Millen, "Optically driven ultra-stable nanomechanical rotor," Nat Commun **8**, 1670 (2017).

[4] F. Monteiro, S. Ghosh, A. G. Fine, and D. C. Moore, "Optical levitation of 10-ng spheres with nano- g acceleration sensitivity," Phys. Rev. A **96**, 063841 (2017).

[5] C. Timberlake, G. Gasbarri, A. Vinante, A. Setter, and H. Ulbricht, "Acceleration sensing with magnetically levitated oscillators," arXiv:1910.07078 [cond-mat, physics:physics, physics:quant-ph] (2019).

[6] T. M. Fuchs, D. G. Uitenbroek, J. Plugge, N. van Halteren, J.-P. van Soest, A. Vinante, H. Ulbricht, and T. H. Oosterkamp, "Measuring gravity with milligram levitated masses," Science Advances **10**, eadk2949 (2024).

[7] A. Arvanitaki and A. A. Geraci, "Detecting High-Frequency Gravitational Waves with Optically Levitated Sensors," Phys. Rev. Lett. **110**, 071105 (2013).

[8] S. Bose, A. Mazumdar, G. W. Morley, H. Ulbricht, M. Toroš, M. Paternostro, A. A. Geraci, P. F. Barker, M. Kim, and G. Milburn, "Spin Entanglement Witness for Quantum Gravity," Phys. Rev. Lett. **119**, 240401 (2017).

[9] E. Howard, R. Roberts, C. Laplane, and T. Volz, "Detecting gravitational waves with optically-levitated nanoparticles," in *2020 Conference on Lasers and Electro-Optics Pacific Rim (CLEO-PR),* (2020), pp. 1–2.

[10] S. Kuhn, A. Kosloff, B. A. Stickler, F. Patolsky, K. Hornberger, M. Arndt, and J. Millen, "Full rotational control of levitated silicon nanorods," Optica, OPTICA **4**, 356–360 (2017).

[11] R. Reimann, M. Doderer, E. Hebestreit, R. Diehl, M. Frimmer, D. Windey, F. Tebbenjohanns, and L. Novotny, "GHz Rotation of an Optically Trapped Nanoparticle in Vacuum," Phys. Rev. Lett. **121**, 033602 (2018).

[12] F. van der Laan, R. Reimann, A. Militaru, F. Tebbenjohanns, D. Windey, M. Frimmer, and L. Novotny, "Optically levitated rotor at its thermal limit of frequency stability," Phys. Rev. A **102**, 013505 (2020).

[13] F. van der Laan, R. Reimann, F. Tebbenjohanns, J. Vijayan, L. Novotny, and M. Frimmer, "Observation of radiation torque shot noise on an optically levitated nanodumbbell," Phys. Rev. Lett. **127**, 123605 (2021).

[14] P. Ju, Y. Jin, K. Shen, Y. Duan, Z. Xu, X. Gao, X. Ni, and T. Li, "Near-field GHz rotation and sensing with an optically levitated nanodumbbell," (2023).

[15] J. Ahn, Z. Xu, J. Bang, Y.-H. Deng, T. M. Hoang, Q. Han, R.-M. Ma, and T. Li, "Optically Levitated Nanodumbbell Torsion Balance and GHz Nanomechanical Rotor," Phys. Rev. Lett. **121**, 033603 (2018).

[16] K. Zeng, X. Xu, Y. Wu, X. Wu, and D. Xiao, "Optically levitated gyroscopes with a MHz rotating micro-rotor," (2023).

[17] J. Ahn, Z. Xu, J. Bang, P. Ju, X. Gao, and T. Li, "Ultrasensitive torque detection with an optically levitated nanorotor," Nat. Nanotechnol. **15**, 89–93 (2020).

[18] Y. Jin, J. Yan, S. J. Rahman, J. Li, X. Yu, and J. Zhang, "6 GHz hyperfast rotation of an optically levitated nanoparticle in vacuum," Photon. Res. **9**, 1344 (2021).

[19] Z. Xu and T. Li, "Detecting Casimir torque with an optically levitated nanorod," Phys. Rev. A **96**, 033843 (2017).

[20] Z. Xu, Z. Jacob, and T. Li, "Enhancement of rotational vacuum friction by surface photon tunneling," Nanophotonics **-1** (2020).

[21] H. Rudolph, J. Schäfer, B. A. Stickler, and K. Hornberger, "Theory of nanoparticle cooling by elliptic coherent scattering," Phys. Rev. A **103**, 043514 (2021).

[22] J. Gieseler, B. Deutsch, R. Quidant, and L. Novotny, "Subkelvin Parametric Feedback Cooling of a Laser-Trapped Nanoparticle," Phys. Rev. Lett. **109**, 103603 (2012).

[23] T. Seberson and F. Robicheaux, "Parametric feedback cooling of rigid body nanodumbbells in levitated optomechanics," Phys. Rev. A **99**, 013821 (2019).

[24] J. Vovrosh, M. Rashid, D. Hempston, J. Bateman, M. Paternostro, and H. Ulbricht, "Parametric feedback cooling of levitated optomechanics in a parabolic mirror trap," J. Opt. Soc. Am. B, JOSAB **34**, 1421–1428 (2017).

[25] J. Gao, F. van der Laan, J. A. Zielińska, A. Militaru, L. Novotny, and M. Frimmer, "Feedback cooling a levitated nanoparticle's libration to below 100 phonons," Phys. Rev. Res. **6**, 033009 (2024).

[26] M. Iwasaki, T. Yotsuya, T. Naruki, Y. Matsuda, M. Yoneda, and K. Aikawa, "Electric feedback cooling of single charged nanoparticles in an optical trap," Phys. Rev. A **99**, 051401 (2019).

[27] F. Tebbenjohanns, M. Frimmer, A. Militaru, V. Jain, and L. Novotny, "Cold Damping of an Optically Levitated Nanoparticle to Microkelvin Temperatures," Phys. Rev. Lett. **122**, 223601 (2019).

[28] G. P. Conangla, F. Ricci, M. T. Cuairan, A. W. Schell, N. Meyer, and R. Quidant, "Optimal Feedback Cooling of a Charged Levitated Nanoparticle with Adaptive Control," Phys. Rev. Lett. **122**, 223602 (2019).

[29] L. Magrini, P. Rosenzweig, C. Bach, A. Deutschmann-Olek, S. G. Hofer, S. Hong, N. Kiesel, A. Kugi, and M. Aspelmeyer, "Real-time optimal quantum control of mechanical motion at room temperature," Nature **595**, 373–377 (2021).

[30] M. Kamba, R. Shimizu, and K. Aikawa, "Optical cold damping of neutral nanoparticles near the ground state in an optical lattice," Opt. Express, OE **30**, 26716–26727 (2022).

[31] F. Tebbenjohanns, M. L. Mattana, M. Rossi, M. Frimmer, and L. Novotny, "Quantum control of a nanoparticle optically levitated in cryogenic free space," Nature **595**, 378–382 (2021).

[32] D. Windey, C. Gonzalez-Ballestero, P. Maurer, L. Novotny, O. Romero-Isart, and R. Reimann, "Cavity-Based 3D Cooling of a Levitated Nanoparticle via Coherent Scattering," Phys. Rev. Lett. **122**, 123601 (2019).

[33] V. Vuletić and S. Chu, "Laser Cooling of Atoms, Ions, or Molecules by Coherent Scattering," Phys. Rev. Lett. **84**, 3787–3790 (2000).

[34] V. Vuletić, H. W. Chan, and A. T. Black, "Three-dimensional cavity Doppler cooling and cavity sideband cooling by coherent scattering," Phys. Rev. A **64**, 033405 (2001).

[35] U. Delić, M. Reisenbauer, D. Grass, N. Kiesel, V. Vuletić, and M. Aspelmeyer, "Cavity Cooling of a Levitated Nanosphere by Coherent Scattering," Phys. Rev. Lett. **122**, 123602 (2019).

[36] U. Delić, M. Reisenbauer, K. Dare, D. Grass, V. Vuletić, N. Kiesel, and M. Aspelmeyer, "Cooling of a levitated nanoparticle to the motional quantum ground state," Science (2020).

[37] J. Piotrowski, D. Windey, J. Vijayan, C. Gonzalez-Ballestero, A. de los Ríos Sommer, N. Meyer, R. Quidant, O. Romero-Isart, R. Reimann, and L. Novotny, "Simultaneous ground-state cooling of two mechanical modes of a levitated nanoparticle," Nat. Phys. pp. 1–5 (2023).

[38] A. Ranfagni, K. Børkje, F. Marino, and F. Marin, "Two-dimensional quantum motion of a levitated nanosphere," Phys. Rev. Research **4**, 033051 (2022).

[39] J. Schäfer, H. Rudolph, K. Hornberger, and B. A. Stickler, "Cooling Nanorotors by Elliptic Coherent Scattering," Phys. Rev. Lett. **126**, 163603 (2021).

[40] A. Pontin, H. Fu, M. Toroš, T. S. Monteiro, and P. F. Barker, "Simultaneous cavity cooling of all six degrees of freedom of a levitated nanoparticle," Nat. Phys. pp. 1–6 (2023).

[41] Y. Y. Fein, P. Geyer, P. Zwick, F. Kiałka, S. Pedalino, M. Mayor, S. Gerlich, and M. Arndt, "Quantum superposition of molecules beyond 25 kDa," Nat. Phys. **15**, 1242–1245 (2019).

[42] M. Rossi, A. Militaru, N. C. Zambon, A. Riera-Campeny, O. Romero-Isart, M. Frimmer, and L. Novotny, "Quantum Delocalization of a Levitated Nanoparticle," (2024).

[43] O. Romero-Isart, A. C. Pflanzer, F. Blaser, R. Kaltenbaek, N. Kiesel, M. Aspelmeyer, and J. I. Cirac, "Large Quantum Superpositions and Interference of Massive Nanometer-Sized Objects," Phys. Rev. Lett. **107**, 020405 (2011).

[44] B. A. Stickler, K. Hornberger, and M. S. Kim, "Quantum rotations of nanoparticles," arXiv:2102.00992 [quant-ph] (2021).

[45] B. A. Stickler, B. Papendell, S. Kuhn, B. Schrinski, J. Millen, M. Arndt, and K. Hornberger, "Probing macroscopic quantum superpositions with nanorotors," New J. Phys. **20**, 122001 (2018).

[46] Y. Ma, K. E. Khosla, B. A. Stickler, and M. S. Kim1, "Quantum persistent tennis racket dynamics of nanorotors," Phys. Rev. Lett. **125**, 053604 (2020).

[47] H. C. v. d. Hulst, *Light Scattering by Small Particles* (Courier Corporation, 1981).

[48] L. Novotny and B. Hecht, *Principles of Nano-Optics* (Cambridge University Press, Cambridge, 2012), 2nd ed.

[49] G. Pesce, P. H. Jones, O. M. Maragò, and G. Volpe, "Optical tweezers: theory and practice," Eur. Phys. J. Plus **135**, 949 (2020).

[50] J. Gieseler, R. Quidant, C. Dellago, and L. Novotny, "Dynamic relaxation of a levitated nanoparticle from a non-equilibrium steady state," Nature Nanotech **9**, 358–364 (2014).

[51] R. Kubo, "The fluctuation-dissipation theorem," Rep. Prog. Phys. **29**, 255 (1966).

[52] W. P. Bowen and G. J. Milburn, *Quantum optomechanics* (CRC press, 2015).

[53] F. van der Laan, "Rotational Levitodynamics," Ph.D. thesis, ETH Zurich (2022).

[54] F. Tebbenjohanns, A. Militaru, A. Norrman, F. Van Der Laan, L. Novotny, and M. Frimmer, "Optimal orientation detection of an anisotropic dipolar scatterer," Phys. Rev. A **105**, 053504 (2022).

[55] J. Bang, T. Seberson, P. Ju, J. Ahn, Z. Xu, X. Gao, F. Robicheaux, and T. Li, "Five-dimensional cooling and nonlinear dynamics of an optically levitated nanodumbbell," Phys. Rev. Research **2**, 043054 (2020).

[56] U. Sezer, L. Wörner, J. Horak, L. Felix, J. Tüxen, C. Götz, A. Vaziri, M. Mayor, and M. Arndt, "Laser-Induced Acoustic Desorption of Natural and Functionalized Biochromophores," Anal. Chem. **87**, 5614–5619 (2015).

[57] P. Asenbaum, S. Kuhn, S. Nimmrichter, U. Sezer, and M. Arndt, "Cavity cooling of free silicon nanoparticles in high vacuum," Nature Communications **4**, 1–7 (2013).

[58] M. Nikkhou, Y. Hu, J. A. Sabin, and J. Millen, "Direct and clean loading of nanoparticles into optical traps at millibar pressures," arXiv:2109.10316 [physics, physics:quant-ph] (2021).

[59] J. Gieseler, "Dynamics of optically levitated nanoparticles in high vacuum," Doctoral thesis, Universitat Politècnica de Catalunya (2014).

[60] R. M. Pettit, "Optomechanics with Optically Levitated Nanoparticles," Ph.D. thesis, University of Rochester (2019).

[61] J. Gieseler, L. Novotny, and R. Quidant, "Thermal nonlinearities in a nanomechanical oscillator," Nature Phys **9**, 806–810 (2013).

[62] U. Delić, "Cavity cooling by coherent scattering of a levitated nanosphere in vacuum," Doctoral Thesis, University Vienna (2019).

[63] L. Martinetz, K. Hornberger, and B. A. Stickler, "Gas-induced friction and diffusion of rigid rotors," Phys. Rev. E **97**, 052112 (2018).

[64] G. Placzek, *The rayleigh and raman scattering*, vol. 526 (Lawrence Radiation Laboratory, 1959).

[65] Anonymous, "Proceedings of the american physical society," Phys. Rev. **69**, 674–674 (1946).

[66] M. Toroš, U. Delić, F. Hales, and T. S. Monteiro, "Coherent-scattering two-dimensional cooling in levitated cavity optomechanics," Phys. Rev. Research **3**, 023071 (2021).

[67] C. Gonzalez-Ballestero, P. Maurer, D. Windey, L. Novotny, R. Reimann, and O. Romero-Isart, "Theory for cavity cooling of levitated nanoparticles via coherent scattering: Master equation approach," Phys. Rev. A **100**, 013805 (2019).

[68] R. Loudon, *The Quantum Theory of Light* (Oxford University Press, 2000), 3rd ed.

[69] S. Nimmrichter, K. Hammerer, P. Asenbaum, H. Ritsch, and M. Arndt, "Master equation for the motion of a polarizable particle in a multimode cavity," New J. Phys. **12**, 083003 (2010).

[70] Z. Li and G. E. Stedman, "Asymmetric response profile of a scanning Fabry-P&-ot interferometer," Opt. Commun. **100** (1993).

[71] A. E. Dangor, "The response of the Fabry-Perot interferometer to rapid changes in optical length," J. Phys. D Appl. Phys. **3** (1970).

[72] J. Poirson, F. Bretenaker, M. Vallet, and A. Le Floch, "Analytical and experimental study of ringing effects in a Fabry–Perot cavity Application to the measurement of high finesses," J. Opt. Soc. Am. B **14**, 2811 (1997).

[73] F. Zhou, Y. Bao, J. J. Gorman, and J. R. Lawall, "Cavity Optomechanical Bistability with an Ultrahigh Reflectivity Photonic Crystal Membrane," Laser & Photonics Reviews **17**, 2300008 (2023).

[74] E. D. Black, "An introduction to Pound–Drever–Hall laser frequency stabilization," Am. J. Phys. **69**, 10 (2001).

[75] J. A. Armstrong, "Theory of interferometric analysis of laser phase noise∗," J. Opt. Soc. Am. **56**, 1024–1031 (1966).

[76] F. Quinlan, S. Gee, S. Ozharar, and P. Delfyett, "The effects of filtering rf source phase noise by a low noise, high quality factor actively modelocked laser on the laser's absolute and relative phase noise," Opt. Express **14**, 5346–5355 (2006).

[77] M. Parniak, I. Galinskiy, T. Zwettler, and E. S. Polzik, "High-frequency broadband laser phase noise cancellation using a delay line," Opt. Express **29**, 6935 (2021).

[78] N. Meyer, A. d. l. R. Sommer, P. Mestres, J. Gieseler, V. Jain, L. Novotny, and R. Quidant, "Resolved Sideband Cooling of a Levitated Nanoparticle in the Presence of Laser Phase Noise," arXiv:1907.02741 [physics, physics:quant-ph] (2019).

[79] S. M. Meenehan, "Cavity Optomechanics at Millikelvin Temperatures," Ph.D. thesis, California Institute of Technology, Pasedena, California (2015).

[80] A. H. Safavi-Naeini, J. Chan, J. T. Hill, S. Gröblacher, H. Miao, Y. Chen, M. Aspelmeyer, and O. Painter, "Laser noise in cavity-optomechanical cooling and thermometry," New J. Phys. **15**, 035007 (2013).

[81] C. Wang, L. Banniard, L. M. de Lépinay, and M. A. Sillanpää, "Fast feedback control of mechanical motion using circuit optomechanics," Phys. Rev. Applied **19**, 054091 (2023).

[82] V. Jain, J. Gieseler, C. Moritz, C. Dellago, R. Quidant, and L. Novotny, "Direct Measurement of Photon Recoil from a Levitated Nanoparticle," Phys. Rev. Lett. **116**, 243601 (2016).

[83] V. Jain, "Levitated optomechanics at the photon recoil limit," Ph.D. thesis, ETH Zurich (2017).

[84] M. Aspelmeyer, T. J. Kippenberg, and F. Marquardt, "Cavity optomechanics," Rev. Mod. Phys. **86**, 1391–1452 (2014).

[85] L. Van Damme, P. Mardešić, and D. Sugny, "The tennis racket effect in a three-dimensional rigid body," Physica D: Nonlinear Phenomena **338**, 17–25 (2017).

List of Figures

List of Tables